Shielded CSI-EPT

Tissue parameter reconstruction based on an analytical model for a shielded birdcage coil in quantized CSI-EPT

T.I. van Velden

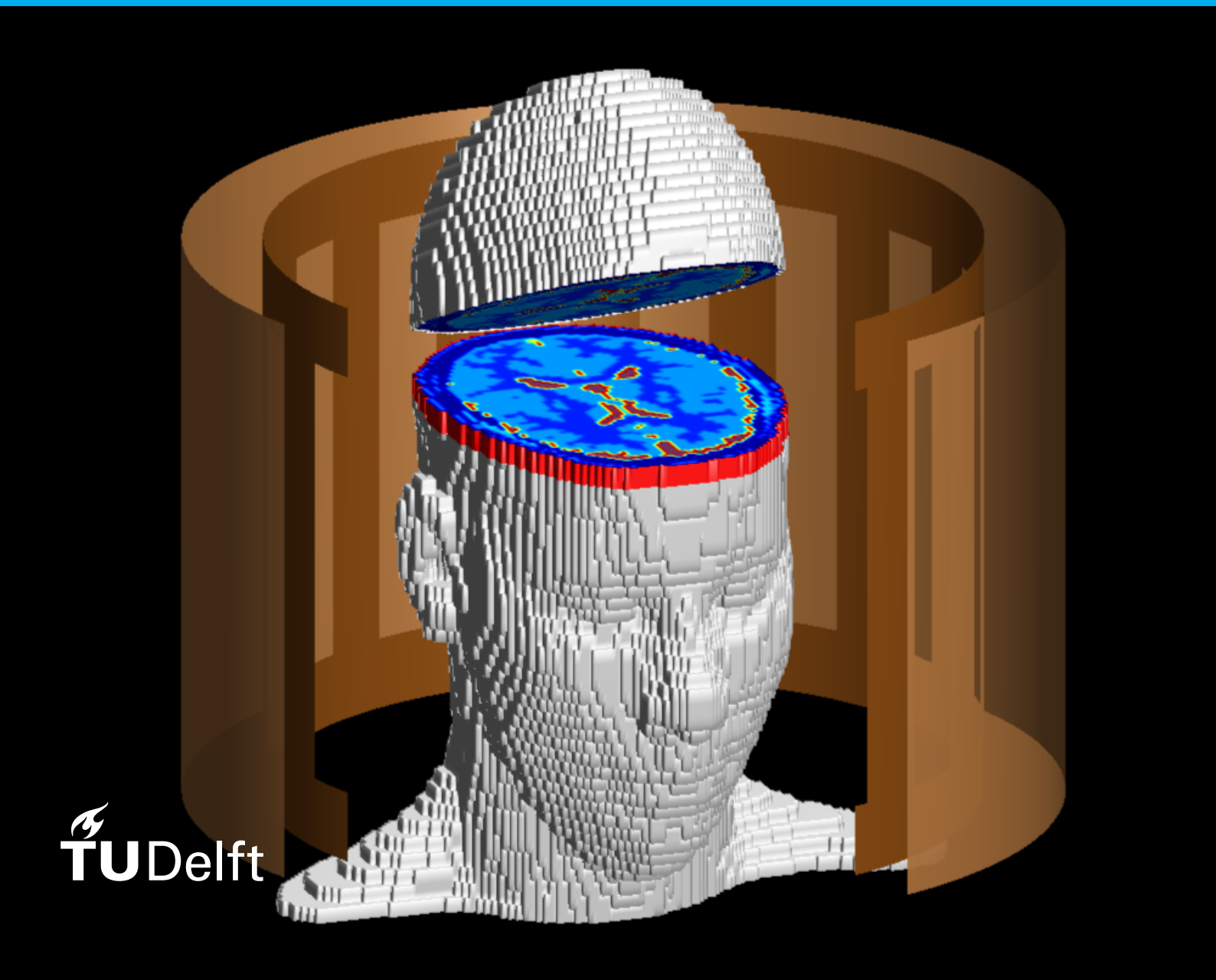

TU Delft

Shielded CSI-EPT

Tissue parameter reconstruction based on an analytical model for a shielded birdcage coil in quantized CSI-EPT

by

T.I. van Velden

to obtain the degree of Master of Science
at the Delft University of Technology.

Student number:	4922166	
Project duration:	April 2024 – February 2025	
Thesis committee:	Dr. ir. R.F. Remis	TU Delft, supervisor
	Dr. ir. B. J. Kooij,	TU Delft

An electronic version of this thesis is available at `http://repository.tudelft.nl/`.

TU Delft

Abstract

Accurate knowledge of the conductivity and permittivity of tissue is vital in the diagnosis of many diseases. Magnetic resonance electrical property tomography (MR-EPT) reconstructs these using measurements of the electromagnetic fields inside the MR-scanner. These properties are reconstructed using two-dimensional contrast source inversion, due to a significant complexity reduction in comparison to its three-dimensional counterpart, allowing for reconstructions in a reasonable amount of time. Data acquisition is usually performed using a shielded birdcage coil. Current methods, however, disregard the presence of this shielding, only accounting for it using a rough first-order approximation, as properly accounting for it would lead to an intractable computational load. This thesis shows a method of analytically describing this shielding in the Greens functions and its efficient implementation in the corresponding Greens operators for CSI-EPT, exploiting the Greens functions being degenerate. This results in a significant increase in the reconstruction performance both qualitatively and quantitatively, at the cost of a slight increase of the computational load. The inversion problem being ill-posed leads to poor reconstruction performance on noisy data. This thesis presents a method for quantization of the tissue parameters, by enforcing a multi-modal distribution for these parameters. Through simulation, the quantization method shows a significant increase in performance for noisy data, at the cost of losing smaller details in the image. This improved model was tested on synthetic E-polarized data, and realistic three-dimensional data, showing a more robust, and accurate reconstruction of the electrical properties for both.

Contents

1 Introduction

Electrical Properties (EPs) can be an aid in characterizing biophysical properties of different tissues. These properties include water content, ion concentration, molecular composition, intracellular space, permeability of the cell membrane (not to be confused with the electrical property of magnetic permeability), and cellular structure [1]. These properties can help in the diagnosis of several types of cancer[2], (malignant) cysts, ischemic tissues[3], among many others. Knowledge of these electrical properties could therefore be vital in the early detection and consequently the faster treatment for these diseases. Besides diagnosis, knowledge on the electric properties are also important in personalized MR safety, where these can be used for local specific absorption rate (SAR) mapping[4], which tells us how much electromagnetic power introduced by the MR-scanner is converted into heat.

These EPs can be mapped using several techniques, each with their own advantages and disadvantages. Electrical Impedance Tomography (EIT) maps these properties by attaching electrodes to the the tissue of interest, applying a current through them. This is limited by in the amount-, and the placement of the electrodes, resulting is significant lower resolutions[5][6]. Ultrasound methods are also limited by their probes, but are also limited by the ability to penetrate different (harder) tissues[7]. The Computed Tomography (CT) methods can acquire higher resolution, but make use of dangerous ionizing X-Ray radiation[8]. To omit the issues of low spatial resolution and/or the usage of dangerous radiation the non-invasive method of Magnetic Resonance Electrical Properties Tomography (MR-EPT) was proposed[9], which uses the non-invasive data acquisition of Magnetic Resonance Imaging (MRI).

There are several methods for MR-EPT which can be categorized in local or global methods and direct or inverse methods. Local methods will find the properties of interest for a particular point using only the data of that point and closely neighboring points, while global methods will find these properties using all data points simultaneously. Local methods often fail for non-smooth surfaces, introducing large errors near boundaries, for which the global methods often perform better. Global methods often also give more information about the system; instead of only reconstructing the electrical properties, also the corresponding electric and magnetic fields are reconstructed, at the cost of a higher computational complexity and more complex implementations. When considering MR-EPT, Maxwell's equations must be solved often. The direct methods will often use the differential form of Maxwell's equation, such that the computationally much more complex integrals do not have to be solved, and one can reside to the estimation of the spatial derivative of the magnetic fields by their numerical gradients. These methods are usually very noise-sensitive. The inverse methods find these properties of interest by formulating an optimization scheme, iteratively solving the inverse MR-EPT problem. This is computationally more complex, but will be more robust in noisy environments.

Using the benefits of both the global and inverse methods, this thesis will use the Contrast Source Inversion method[10][11] for the reconstruction. This method is based on a physics based model, and iteratively optimizing this model such that the simulated fields generated by this model will best approach the measured fields.

While the data-acquisition, or the gathering of the measurements for MR-EPT, which is called $\mathbf{B}_1^+$-mapping, is a whole field of research on itself, some basic understanding of how the MRI-machine acquires the data is required. The MRI-machine (in high-field MRI) consists of a strong super-conducting magnet, creating a strong magnetic background field $\mathbf{B}_0$, which puts all magnetic particles inside the body in the same orienta-

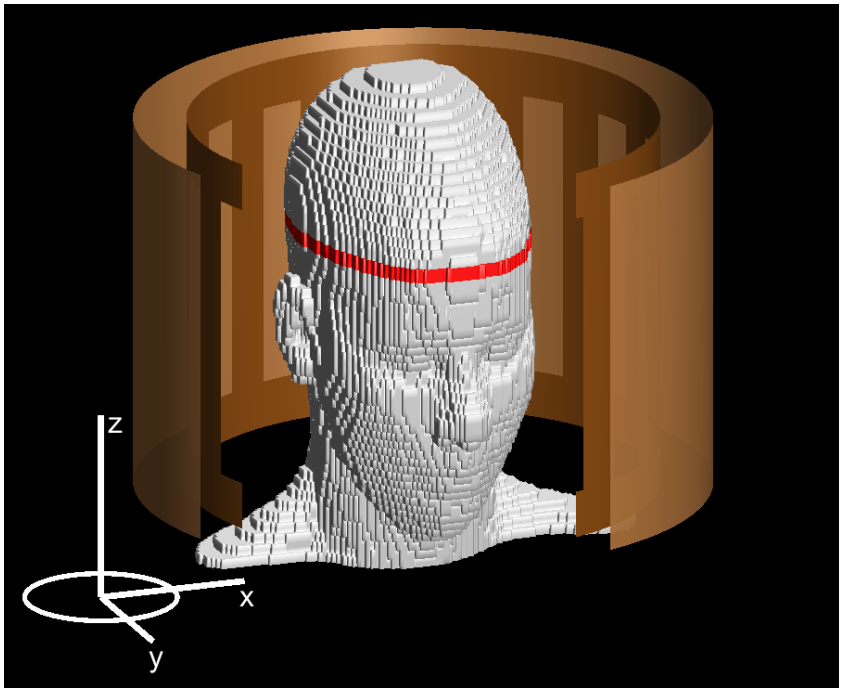

Figure 1.1: Measurement setup showing the rungs of the birdcage coil, as well as the surrounding RF-shielding. A single slice is highlighted in red, since this thesis uses two-dimensional CSI-EPT which only uses information of a single slice. This figure also shows the convention for the Cartesian coordinate system used throughout this thesis

tion, which in this thesis is in the negative $\hat{z}$-direction. This state is the equilibrium state. These particles are struck out of this equilibrium by a radio frequency (RF-)pulse, after which the particles will return to this equilibrium. This relaxation back to equilibrium happens in a rotating manner, and the rates in which they relax back to this equilibrium are described by the T_1 and T_2 relaxation time, for the longitudinal and transversal components of the magnetization, respectively. These magnetically rotating regions can be measured by the receive coils, and thus be measured.

Nowadays, the most commonly used antennas for transmitting the RF-pulse are antennas placed in a birdcage coil configuration. Birdcage coils consist of two conducting rings on the top and bottom of the coil, which are connected by an even number of rungs or legs. A schematic overview of such a coil is shown in Fig. 1.1. These coils are used for the transmission of the RF-pulse, but could also be used in reception, given that the object to be imaged is sufficiently close, which is a valid assumption for smaller birdcage coils such as head coils, or knee coils. These birdcage coils are often shielded by an RF-shield to prevent any external sources injecting interfering signals into the measurement distorting them, and vice versa to prevent electromagnetic (EM) radiation generated by these coils to cause interference in nearby (medical) devices. The shielding present around these birdcage coils is sufficiently close to the object to image that it has a significant impact on the electromagnetic fields caused by the antennas of the birdcage coils, and the effects caused by object inside this shield. While some of the reconstruction methods approximate the effects of this shield by means of mirror-sources[12], this is only applied on the current-sources in the incident field, and there not accurately describe the effects this shielding has on the electromagnetic fields. According to [12], analytically modeling the effect of the shielding would severely increase the computational complexity. Yet, this thesis will provide a better (analytical model) for the effect this RF-shielding has on the electric and magnetic fields on both the incident and scattered field, and subsequently the reconstruction, and implementing this shielding efficiently.

The optimization problem required for the reconstruction is ill-posed, and nonlinear. This means that when the optimization algorithm converges to a (local) optimum, this optimum might not be truly feasible physically; e.g. negative conductivities. These constraints have been implemented before by either applying the Rectified Linear Unit (ReLU) function on, or taking the absolute of these strictly nonnegative optimization parameters, to make sure they will satisfy the physical representation better. This thesis will provide a different approach by using the knowledge that tissues have distinct electrical properties which can be assumed constant in a patient.

1.1. Research question

To achieve the goals mentioned in the section above the following research question is to be answered.

How can the effects of the RF-shield be implemented analytically for tissue parameter reconstruction in two-dimensional CSI-EPT, while maintaining a tractable computational complexity?

This problem is decomposed into several subproblems, each with their own research question. These are:

- SQ1a: How can the effects of the shield be accounted for analytically in two-dimensional CSI-EPT?
- SQ1b: What improvements can be made to reduce the computational complexity without losing of information?
- SQ2: How can the multi-modal distribution of tissue parameters be exploited to increase reconstruction accuracy?

1.2. Contributions

This thesis provides several contributions corresponding to the subquestions mentioned above. These contributions are indexed according to the subquestion they are answering:

- C1a: The effects of the RF-shielding can be modeled analytically in the Greens functions, and subsequently the corresponding discretized Greens operators. This allows for a fully analytical description of the fields within the PEC enclosed setup for E-polarized fields;
- C1b: While the shift-invariance for the new Greens operators is lost, the Greens operators can still be calculated efficiently by exploiting the Greens function being degenerate;
- C2: While only implemented for two-dimensional CSI-EPT, the quantization method shows a significant increase in performance for simulations on synthetic noisy measurements.

1.3. Thesis outline

The outline of this thesis is as follows. Chapter 2 provides the description of the standard two-dimensional CSI-EPT method, and its current implementations. Chapter 3 then describes how this standard CSI-EPT must be altered to analytically account for the effects of the RF-shielding. Chapter 4 will provide an analysis of different segmentation methods such that these can be used to enforce the quantization for the tissue parameters interim the optimization algorithm. Chapter 5 presents the numerical results of several simulations based on these methods, after which Chapter 6 concludes this work.

2

Theory

The technique used for reconstruction the electric properties of tissue is the Contrast Source Inversion (CSI) method. CSI is global inversion method using the integral representation of the electromagnetic fields. The externally applied currents, located in the birdcage coils' rungs, are only z-oriented, which for the midplane of the birdcage coil leads to the assumption that all fields in this plane are E-polarized. For body coils, the observation has been made that the longitudinal component of the electric field is an order of magnitude larger than its transverse component[13]. This E-polarization allows for the use of the two-dimensional CSI-EPT method, severely reducing the computational complexity w.r.t. the much harder three-dimensional CSI-EPT, as described in [14]. This reduction from the three-dimensional formulation allows for convergence within a couple hundred iterations to a few thousand, in comparison to tens of thousands for the three-dimensional formulation. This reduced the computation time from several days to only a few hours (when modeling a three-dimensional subject using a pseudo 3D approach).

The CSI-EPT algorithm iteratively solves the inverse electromagnetic scattering problem, optimizing for the contrast source and contrast function (both containing information of the tissue parameters) alternatingly. This optimization is performed by minimizing the mismatch between the fields generated by a physical model to the fields acquired by measurement, while adhering to Maxwell's equations. The values of the tissue parameters can then be retrieved from these optimization parameters.

This chapter will describe the theory behind the contrast source inversion method used for electrical property tomography, as well as the challenges for the implementation. It starts with building the physical model. The space in which this physical model operates will then be discretized, such that it matches the discretization of the measured data from the MRI-machine. Using this physical model in discretized space, the optimization algorithm will be discussed which will reconstruct the electrical properties of tissue.

This chapter describes the two-dimensional CSI-EPT method as given by [15], which assumes all sources to be radiating in a limitless homogeneous medium. In actuality this space is not homogeneous due to the presence of the RF-shield enclosing the measurement setup, which in this case will be corrected for by mirror-sources[12]. Chapter 3 describes how the standard two-dimensional CSI-EPT must be altered to properly include the presence of the RF-shielding.

2.1. Physical model

In CSI-EPT the goal is to reconstruct the electrical properties σ and ϵ_r (μ is considered constant and equal to μ_0 inside the human body) from the measured data, by matching the electromagnetic fields generated by the model to the fields measured by the MR-scanner. Most EPT methods reconstruct the electrical properties based on measurements of the left-hand rotating magnetic field $\hat{B}_1^+$. The MR-scanner can only measure the amplitude of the $\hat{B}_1^+$-field, and measure its transceive phase, which is the superposition of the (left-hand rotating) transmit field and the (right-hand rotating) receive field: $\phi^{\pm} = \angle\hat{B}_1^+ + \angle\hat{B}_1^-$. This is corrected for during the iterative process by performing the Transceive Phase Correction[12]. The goal now becomes to formulate the physics such that the measured $\hat{B}_1^+$ field can be described according to the electrical properties σ and ϵ_r, allowing for the optimization over these properties.

The electric and magnetic fields are described by Maxwell's equations, where the equations of interest are Faraday's Law of Induction and the Ampere-Maxwell's Law, as these describe the interaction between these.

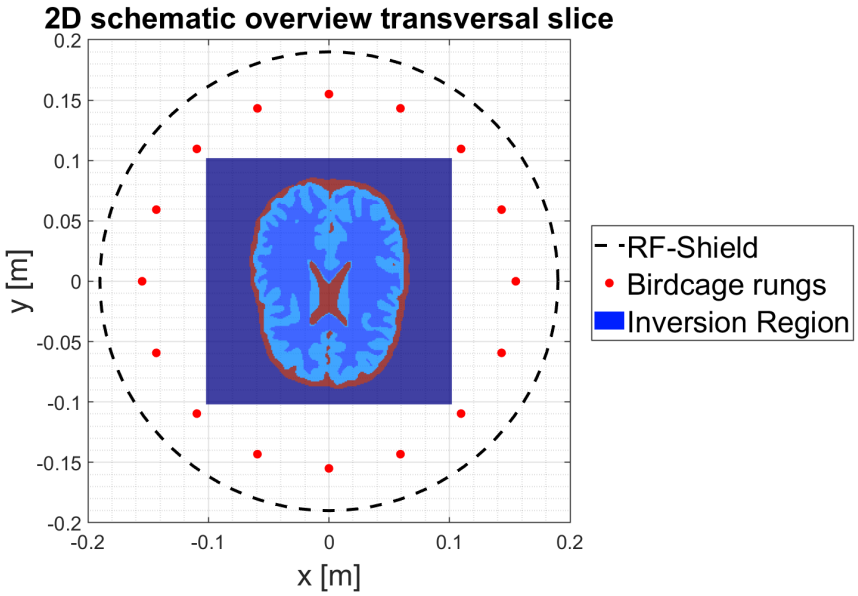

Figure 2.1: Schematic overview of a transversal slice for 2D CSI-EPT, using a standard birdcage coil for heads ($R_{\text{birdcage}} = 0.155$m, $R_{\text{RF}} = 0.190$m). The inversion region is now filled in with the conductivity of M32, slice 80 of the ADEPT dataset.

The phasor representation (denoted by a hat) of these fields, using a time factor $e^{j\omega t}$, are given by:

$$-\nabla \times \hat{\mathbf{H}} + \hat{\eta}\hat{\mathbf{E}} = -\hat{\mathbf{J}}^{\text{ext}} \tag{2.1a}$$

$$\nabla \times \hat{\mathbf{E}} + j\omega\mu\hat{\mathbf{H}} = -\hat{\mathbf{K}}^{\text{ext}}, \tag{2.1b}$$

where $\hat{\eta} = \sigma + j\omega\epsilon$ denotes the per-unit-length admittance of the tissue.

Near the midplane of the birdcage coil the externally applied currents of the birdcage coil can be approximated by z-oriented line currents. This leads to the assumption that all present wavesare E-polarized. This perpendicular polarization means that the electric field is oriented only along z, while the magnetic field is located only in the transversal (or in medical terms *axial*) (x, y)-plane. This assumption for E-polarization implies an invariance along z; this assumption is therefore most valid when considering structures which do not vary much along this direction (e.g. an arm or leg). Using this independence of z, the perpendicular polarization of the waves, and using the notion that magnetic currents $\mathbf{K}^{\text{ext}}$ do not exist physically, the 3-dimensional Ampere-Maxwell's law (Eq. 2.1b) can be decomposed in its Cartesian components and simplified to:

$$\hat{H}_x = -\frac{1}{j\omega\mu}\partial_y \hat{E}_z \tag{2.2a}$$

$$\hat{H}_y = \frac{1}{j\omega\mu}\partial_x \hat{E}_z. \tag{2.2b}$$

Substituting these into Faraday's Law of Induction as given by Eq. 2.1a, results in the 2-dimensional Helmholtz equation:

$$\partial_x\partial_x\hat{E}_z + \partial_y\partial_y\hat{E}_z - j\omega\mu\left(\sigma + j\omega\epsilon\right)\hat{E}_z = j\omega\mu\hat{f}^{\text{ext}}, \tag{2.3}$$

which for sources radiating in free-space, characterized by $\epsilon = \epsilon_0$, $\mu = \mu_0$ and $\sigma = 0$, can be reduced to the inhomogeneous Helmholtz equation:

$$\left(\partial_x^2 + \partial_y^2\right)\hat{E}_z + k_0^2\hat{E}_z = -\hat{f}, \tag{2.4}$$

where the source $\hat{f} = -j\omega\mu_0\hat{J}^{\text{ext}}$ and $k_0 = \sqrt{\epsilon_0\mu_0}$ denotes the wave-number of the wave propagating in free-space. Using an outward radiation condition (the boundary condition imposed by Sommerfeld radiation condition), a unique solution exists to this differential equation, and is given by the well-known integral formulation:

$$\hat{E}_z(\mathbf{r}) = \int_{\mathbf{r}'\in\mathbb{R}^2} \hat{g}^{EJ}(\mathbf{r},\mathbf{r}')\hat{f}(\mathbf{r}')\mathrm{d}\mathbf{r}', \tag{2.5}$$

where $\hat{g}^{EJ}(\mathbf{r},\mathbf{r}')$ denotes the Greens function describing the electric field generated by an electric current radiating in a homogeneous medium (air in this case). This Greens function for the electric field for the two-dimensional Helmholtz equation is given by:

$$\hat{g}^{EJ}(\mathbf{r},\mathbf{r}') = \frac{1}{4j} H_0^{(2)}(k|\mathbf{r}-\mathbf{r}'|), \tag{2.6}$$

where $H_0^{(2)}(\cdot)$ denotes the order zero Hankel function of the second kind.

In inverse scattering problems, a clear distinction between the incident field and the scattered field must be made. The incident field describes the fields without the presence of the object of interest, while the scattered field describes the effect this object has on the fields. Both of these fields have their own sources and should therefore be solved differently for, but the superposition of the two fields describes the total field:

$$\hat{\mathbf{E}} = \hat{\mathbf{E}}^{\text{inc}} + \hat{\mathbf{E}}^{\text{sca}} \qquad \text{and} \qquad \hat{\mathbf{H}} = \hat{\mathbf{H}}^{\text{inc}} + \hat{\mathbf{H}}^{\text{sca}}. \tag{2.7}$$

2.1.1. Incident fields

As stated before, the incident fields denote the fields without the presence of the object of interest. This is the field induced by the antennas of the birdcage coil, with the presence of the RF-shielding (which for now will be approximated). In clinical MRI applications birdcage coils are commonly used as these perform well for data acquisition by allowing for quadrature drive, and providing a more homogeneous transmit field [16], subsequently allowing for higher signal-to-noise ratios (SNRs).

The birdcage coil, or more specifically the collection of rungs can be approximated by a collection of z-oriented line sources, each excited with its own phase and amplitude to reach a desired polarization. The current induced by the birdcage coil can therefore be described as a super-position of Delta of Dirac sources as:

$$\hat{\mathbf{J}}_{\text{bc}}^{\text{ext}}(\mathbf{r}) = \sum_{n=1}^{N_A} \alpha^{[n]} \delta(\mathbf{r}-\mathbf{r}_A^{[n]}) e^{j\phi^{[n]}} \hat{z}, \tag{2.8}$$

where $\alpha^{[n]}$ denotes the amplitude of the current used in the excitation of rung n, and $\phi^{[n]}$ its phase. The most commonly used excitation method for birdcage coils is quadrature, in which multiples of four antennas are excited in such a way to achieve a circularly polarized incident field. This means for a setup with 4 antennas that the phase shift between two neighboring antennas is 90 degrees, for 8 rungs this becomes 45 degrees, etc. The amplitude $\alpha^{[n]}$ in quadrature excitation is constant across all antennas.

For birdcage coils to reach a good signal-to-noise ratio (SNR) shielding is required, as without proper shielding the RF coils might interfere with other coils present in the MRI machine, such as the gradient coils, or receive signals from other medical equipment present nearby; both leading to a reduced image quality [16]. In clinical MRI such a shield is usually made of a highly conductive material, such as copper. This highly conductive shield can therefore be approximated by a shield made of Perfectly Electric Conducting (PEC) material. Transverse components of the electric field must vanish at the PEC's surface, which can be achieved by applying the image theorem and placing a mirror-source at equal distance from the shield on the other side of the shield with opposite polarization[17]. For a flat surface, this would result in the construction of one mirror source while for the circular PEC surface, an infinite number of mirror sources would have to be constructed. This in general is not tractable, thus an improved placement of this single mirror source is proposed to provide a better first-order approximation for circular shields[12]. According to [12] this approximation of the RF-shields avoids severe increases in computational complexity and computation time, at the cost of a less accurate reconstruction. The improved placement of this mirror-source for a rung located at the cylindrical coordinates (r_s,θ) then becomes:

$$\mathbf{r}_{\text{ms}} = (r_{\text{ms}},\theta) = (\frac{R_{\text{RF}}^2}{r_s},\theta), \tag{2.9}$$

where R_{RF} denotes the radius of the RF-shield. The current source as given by these mirror-sources is then described as:

$$\hat{\mathbf{J}}_{\text{ms}}^{\text{ext}}(\mathbf{r}) = -\sum_{n=1}^{N_A} \alpha^{[n]} \delta(\mathbf{r}-\mathbf{r}_{ms}^{[n]}) e^{j\phi^{[n]}} \hat{z}, \tag{2.10}$$

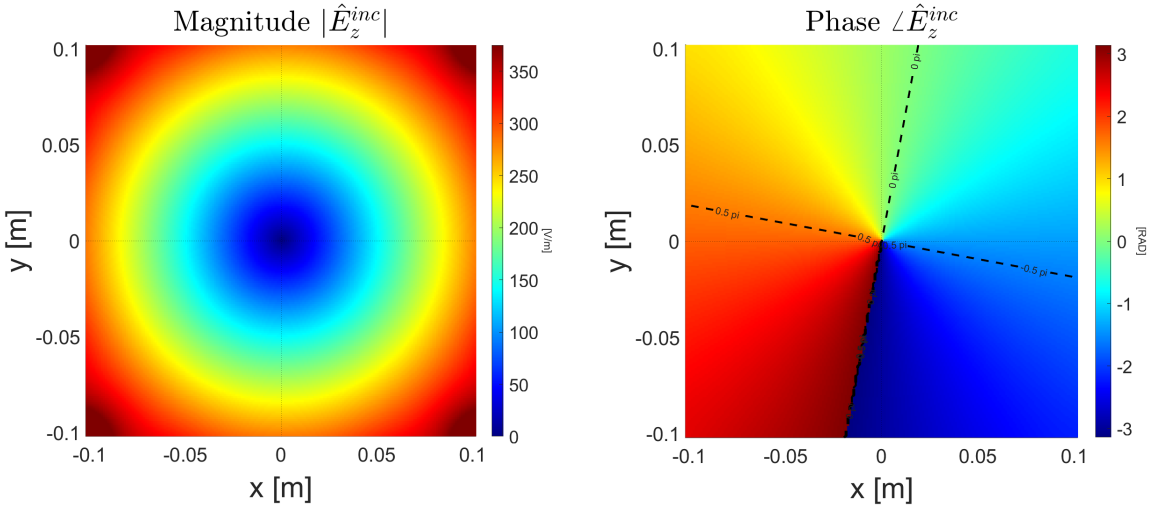

(a) Magnitude of the incident electric field

(b) Phase of the incident electric field

Figure 2.2: Incident electric field generated using mirror-sources in a head sized birdcage coil. This image is generated using an inversion region of 256 × 256 pixels where each pixel is 1mm × 1mm. This figure shows the circular polarization transmitted by the birdcage coil, with a zero in the center of the birdcage coil.

and consequently the total externally applied current source for the incident field can now be described as:

$$\hat{\mathbf{J}}^{\text{ext}}(\mathbf{r}) = \hat{\mathbf{J}}^{\text{ext}}_{\text{bc}}(\mathbf{r}) + \hat{\mathbf{J}}^{\text{ext}}_{\text{ms}}(\mathbf{r}). \tag{2.11}$$

Substituting this expression for the total externally applied current source in the integral expression of Eq. 2.5, the incident electric field can be calculated as:

$$\hat{E}_z^{\text{inc}}(\mathbf{r}) = -\alpha \frac{\omega\mu}{4} \sum_{n=1}^{N_A} \left[H_0^{(2)}\left(k\left|\mathbf{r}-\mathbf{r}_A^{[n]}\right|\right) e^{j\phi^{[n]}} - H_0^{(2)}\left(k\left|\mathbf{r}-\mathbf{r}_{\text{ms}}^{[n]}\right|\right) e^{j\phi^{[n]}} \right]. \tag{2.12}$$

The incident electric field for a 16-rung head-size birdcage coil using a unitary current ($\alpha^{[n]} = 1$) is shown in Fig. 2.2, where the circular polarization is clearly visible. It also becomes rather apparent that in the center of this inversion region, the magnitude of the incident field vanishes, due to the combination of oppositely polarized antennas at each side of the birdcage coil.

The magnetic field can be expressed in a similar manner as the electric field, in the sense that it satisfies a similar Helmholtz equation as defined for the electric field:

$$\hat{\mathbf{H}}(\mathbf{r}) = \int_{\mathbf{r}'\in\mathbb{R}^2} \hat{\mathbf{g}}^{HJ}(\mathbf{r},\mathbf{r}')\hat{f}(\mathbf{r}')\mathrm{d}\mathbf{r}'. \tag{2.13}$$

Using the linearity of the used operators, and the relation between the electric and magnetic field of Eq. 2.2, the Greens function for the magnetic field from an electric current can be described as:

$$\hat{\mathbf{g}}^{HJ}(\mathbf{r},\mathbf{r}') = \begin{bmatrix} \hat{g}_x^{HJ}(\mathbf{r},\mathbf{r}') \\ \hat{g}_y^{HJ}(\mathbf{r},\mathbf{r}') \end{bmatrix} = \begin{bmatrix} -(y-y') \\ (x-x') \end{bmatrix} \frac{1}{|\mathbf{r}-\mathbf{r}'|} \frac{k}{4j(j\omega\mu)} H_1^{(2)}(k|\mathbf{r}-\mathbf{r}'|). \tag{2.14}$$

This Greens function can, subsequently, be used to calculate the incident magnetic fields induced by the current source (which is still defined as the sum of the currents on the rungs and their corresponding mirror-sources). This results in an incident magnetic field of:

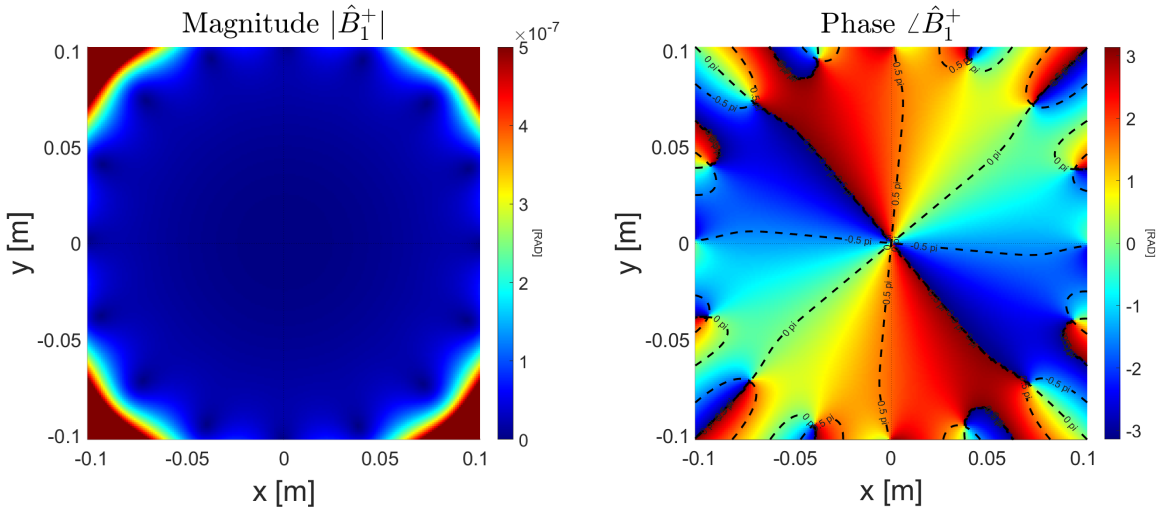

(a) Magnitude of the incident magnetic B_1^+ field

(b) Phase of the incident magnetic B_1^+ field

Figure 2.3: Incident magnetic field generated using mirror-sources in a head sized birdcage coil. This image is generated using an inversion region of 256 × 256 pixels where each pixel is 1mm × 1mm. This figure shows the circular polarization transmitted by the birdcage coil, with a zero in the center of the birdcage coil.

$$\hat{\mathbf{H}}(\mathbf{r}) = \begin{bmatrix} \hat{H}_x \\ \hat{H}_y \end{bmatrix} = -\alpha \sum_{n=1}^{N_A} \begin{bmatrix} -(y - y_A^{[n]}) \\ (x - x_A^{[n]}) \end{bmatrix} \frac{1}{\left|\mathbf{r} - \mathbf{r}_A^{[n]}\right|} \frac{k}{4j} H_1^{(2)}\left(k\left|\mathbf{r} - \mathbf{r}_A^{[n]}\right|\right) e^{j\phi^{[n]}} + \begin{bmatrix} (y - y_{\text{ms}}^{[n]}) \\ -(x - x_{\text{ms}}^{[n]}) \end{bmatrix} \frac{1}{\left|\mathbf{r} - \mathbf{r}_{\text{ms}}^{[n]}\right|} \frac{k}{4j} H_1^{(2)}\left(k\left|\mathbf{r} - \mathbf{r}_{\text{ms}}^{[n]}\right|\right) e^{j\phi^{[n]}}. \tag{2.15}$$

The incident magnetic field of the same 16-rung head-size birdcage coil as for the incident electric field is shown in Fig. 2.3.

The incident electric and magnetic fields are independent of the object later placed in the MR-scanner. This means that these only have to be determined once, during the full CSI-EPT algorithm. When using data from other sources, the excitation strength of the birdcage coil is often unknown, thus the α, and subsequently the strength of the incident electric and magnetic must be estimated.

2.1.2. Scattered fields

With this knowledge on the fields without the presence of the object of interest, the effects this object has on the electromagnetic can be described. This object will often be denoted as the scatterer, also justifying the name 'scattered' fields. The scattered fields contain the information of the electrical properties of the object of interest.

In an analogous manner, the Helmholtz equation for the scattered field can be formulated, reaching the same integral form as shown for the incident field in Eq. 2.5. Using the scattering formalism given in Appendix A, one can define the equivalent current sources which introduce this contrast to the image as:

$$\hat{\mathbf{J}}^{\text{sca}}(\mathbf{r}) = \left(\hat{\eta}(\mathbf{r}) - \hat{\eta}_0\right) \hat{\mathbf{E}}(\mathbf{r}), \tag{2.16}$$

which can be used in the integral formulation of Eq. 2.5w reaching the following definition for the scattered electric field:

$$\hat{\mathbf{E}}^{\text{sca}}(\mathbf{r}) = \int_{\mathbf{r}' \in \mathbb{R}^2} \hat{g}^{EJ}(\mathbf{r}, \mathbf{r}') \hat{f}^{\text{sca}}(\mathbf{r}') \mathrm{d}\mathbf{r}' = -j\omega\mu_0 \int_{\mathbf{r}' \in \mathbb{R}^2} \hat{g}^{EJ}(\mathbf{r}, \mathbf{r}') \hat{\mathbf{J}}^{\text{sca}}(\mathbf{r}') \mathrm{d}\mathbf{r}'. \tag{2.17}$$

This integral formulation for the scattered field can be simplified by introducing the contrast source $\hat{\mathbf{w}}$,

which is defined as:

$$\hat{\mathbf{w}}(\mathbf{r}) = \hat{\chi}(\mathbf{r})\hat{\mathbf{E}}(\mathbf{r}), \tag{2.18}$$

where $\hat{\mathbf{E}}(\mathbf{r})$, denotes the *total* electric field in point $\mathbf{r}$, and the contrast function $\hat{\chi}$ is defined as:

$$\hat{\chi}(\mathbf{r}) = \frac{\hat{\eta}(\mathbf{r}) - \hat{\eta}_0}{\hat{\eta}_0} = \epsilon_r(\mathbf{r}) - 1 - j\frac{\sigma(\mathbf{r})}{\omega\epsilon_0}. \tag{2.19}$$

Notice that the (relative) permittivity and conductivity are independently present in the real and imaginary part of this contrast function, respectively, which allow for the reconstruction of these properties from this contrast source. Given the product with the total electric field in Eq. 2.18, the real and imaginary part of this contrast function correspond with the displacement and conduction current, respectively.

With this contrast source, the scattered field can be calculated as:

$$\hat{\mathbf{E}}^{\text{sca}}(\mathbf{r}) = \mathscr{G}_E\{\hat{\mathbf{w}}\}(\mathbf{r}) = k_0^2 \int_{\mathbf{r}'\in\mathbb{R}^2} \hat{g}^{EJ}(\mathbf{r},\mathbf{r}')\hat{\mathbf{w}}(\mathbf{r}')\mathrm{d}\mathbf{r}', \tag{2.20}$$

where $\mathscr{G}_E\{\hat{\mathbf{w}}\}$ is the operator used to calculate the scattered field using the contrast source, which is often called the *object operator*. Note that this scattered field does not take into account the effect of the RF-shielding, as stated prior this was intentional to keep the computation time more tractable.

By following the same steps as for the scattered electric field, the operator for the scattered magnetic field can be determined. The scattered magnetic field can then be calculated by as:

$$\hat{\mathbf{H}}(\mathbf{r}) = \eta_0 \int_{\mathbf{r}'\in\mathbb{R}^2} \hat{\mathbf{g}}^{HJ}(\mathbf{r},\mathbf{r}')\hat{\mathbf{w}}(\mathbf{r}')\mathrm{d}\mathbf{r}'. \tag{2.21}$$

This magnetic field is given in Cartesian coordinates, and are not describing the fields measured by the MR-scanner, since the MR-scanner is measuring the transmit, left-hand rotating, $\hat{B}_1^+$ field. The total $\hat{\mathbf{B}}_1$ field, can be decomposed into the left-hand rotating, transmit, field $\hat{B_1^+}$, and the right-hand rotating, receive field, $\hat{B_1^-}$. The transmit field can be found using[18]:

$$\hat{B}_1^+(\mathbf{r}) = \frac{\hat{B}_{1,x}(\mathbf{r}) + j\hat{B}_{1,y}(\mathbf{r})}{2} = \mu_0\frac{\hat{H}_x(\mathbf{r}) + j\hat{H}_y(\mathbf{r})}{2}. \tag{2.22}$$

Note that the B_1^+-fields were not defined for the incident field, since strictly spoken the B_1^+ fields can only exist in the presence of an object in the MR-scanner. This incident B_1^+-field can be simulated mathematically, but these would in practise not exist. Following the convention of defining the operators for CSI-EPT, the *data operator*, which gets its name from the notion that it simulates the measured data, can be defined as:

$$\hat{B}_1^{+,\text{sca}}(\mathbf{r}) = \mathscr{G}_{B_1^+}\{\hat{\mathbf{w}}\}(\mathbf{r}) = \frac{\mu_0\eta_0}{2}\int_{\mathbf{r}'\in\mathbb{R}^2} (\hat{g}_x^{HJ}(\mathbf{r},\mathbf{r}') + j\hat{g}_y^{HJ}(\mathbf{r},\mathbf{r}'))\hat{\mathbf{w}}(\mathbf{r}')\mathrm{d}\mathbf{r}'. \tag{2.23}$$

This section has now fully described how the fields are influenced by the excitation caused by the approximated 'shielded' birdcage coil, and how the electrical properties affect the contrast, and consequently the (scattered) fields. This section shows that the physical description used in current methods only use the mirror-source approximation in the incident field, while assuming radiation in a limitless homogeneous medium for the scattered field.

2.2. Discretization

During the data acquisition of the MR-scanner called B_1^+-mapping the data is only acquired at discretized positions in space. This discretization is limited by the chosen amount of pixels for a particular Field Of View (FOV). The amount of pixels chosen affects the SNR of the image, since when the pixel is larger more power can be received in that pixel, and vice versa[19]. This discretization of the space in a single transverse slice by using the midpoint method is given by:

$$\mathbf{r}_{i,j} = \begin{bmatrix} x_i \\ y_j \end{bmatrix} = \begin{bmatrix} \frac{\delta_x}{2} + i\delta_x \\ \frac{\delta_y}{2} + j\delta_y \end{bmatrix}, \tag{2.24}$$

where δ_x and δ_y are the spatial resolution in mm/pixel in the x and y dimension, respectively. This discretization holds for all indexes $i = 0, ..., M-1$ and $j = 0, ..., N-1$, where M denotes the amount of pixels in the x direction, and N the amount in y.

Under the assumption that the pixels outside of the imaging domain do not contribute to the measured signal, meaning that the scatterer is completely inside the imaging domain, an approximation can be made for the integrals in the Greens operators derived in Sec. 2.1. These integrals can be approximated by performing a double Riemann sum, which for the scattered electric field results in:

$$\hat{E}_z^{\text{sca}}(\mathbf{r}_{i,j}) = k_0^2 \delta_x \delta_y \sum_{m=0}^{M-1} \sum_{n=0}^{N-1} g^{EJ}(\mathbf{r}_{i,j}, \mathbf{r}_{m,n}) \hat{\mathbf{w}}_{m,n}, \tag{2.25}$$

where the m, n subscript denotes the value of the quantity at $\mathbf{r}_{m,n}$ (equivalent Riemann sums can be formulated for the magnetic field operators). This double sum can be converted to a vector dot-product by vectorizing the discretized terms for the Greens function, contrast function and electric field. The vectorization itself is performed using the big-endian[20] convention. This results in Eq. 2.25 to be written as:

$$\begin{aligned}\hat{E}_z^{\text{sca}}(\mathbf{r}_{i,j}) &= k_0^2 \delta_x \delta_y \text{vec}\left(\begin{bmatrix} \hat{g}^{EJ}(\mathbf{r}_{i,j}, \mathbf{r}_{0,0}) & \hat{g}^{EJ}(\mathbf{r}_{i,j}, \mathbf{r}_{0,1}) & \dots & \hat{g}^{EJ}(\mathbf{r}_{i,j}, \mathbf{r}_{0,N-1}) \\ \hat{g}^{EJ}(\mathbf{r}_{i,j}, \mathbf{r}_{1,0}) & \hat{g}^{EJ}(\mathbf{r}_{i,j}, \mathbf{r}_{1,1}) & & \vdots \\ \vdots & & \ddots & \vdots \\ \hat{g}^{EJ}(\mathbf{r}_{i,j}, \mathbf{r}_{M-1,0}) & \dots & \dots & \hat{g}^{EJ}(\mathbf{r}_{i,j}, \mathbf{r}_{M-1,N-1}) \end{bmatrix}\right)^T \text{vec}(\hat{\mathbf{W}}) \\ &= k_0^2 \delta_x \delta_y \text{ vec}\left(\mathbf{G}^{EJ}(\mathbf{r}_{i,j})\right)^T \text{ vec}(\hat{\mathbf{W}}),\end{aligned} \tag{2.26}$$

where $\hat{\mathbf{W}}$ denotes the contrast source defined for all pixels in the slice. This Riemann sum is now performed to find the scattered electric field at one location in space, but can easily be extended to be performed for all locations in space simultaneously by stacking the electric fields of all locations in one vector. This results in:

$$\hat{\mathbf{e}}_z^{\text{sca}} = \begin{bmatrix} \hat{E}_z^{\text{sca}}(\mathbf{r}_{0,0}) \\ \hat{E}_z^{\text{sca}}(\mathbf{r}_{0,1}) \\ \vdots \\ \hat{E}_z^{\text{sca}}(\mathbf{r}_{M-1,N-1}) \end{bmatrix} = k_0^2 \delta_x \delta_y \begin{bmatrix} \text{vec}\left(\mathbf{G}(\mathbf{r}_{0,0})\right)^T \\ \text{vec}\left(\mathbf{G}(\mathbf{r}_{0,1})\right)^T \\ \vdots \\ \text{vec}\left(\mathbf{G}(\mathbf{r}_{M-1,N-1})\right)^T \end{bmatrix} \text{vec}(\hat{\mathbf{W}}) = \mathbb{G}^{EJ} \text{vec}(\hat{\mathbf{W}}), \tag{2.27}$$

where $\mathbb{G}^{EJ} \in \mathbb{C}^{MN \times MN}$. This method of calculating the fields using the full-matrix implementation of the double Riemann sum will be called the *naive* implementation of the Greens operators. The computational complexity of this naive implementation for calculating this scattered field using the contrast sources is defined by the matrix-vector multiplication of order $\mathcal{O}(M^2N^2)$. This method of solving the electric field numerically can be used analogously for the magnetic field, resulting in a numerical approximation of $\mathcal{G}_{B_1^+}\{\hat{\mathbf{w}}\}$: $\mathbb{G}^{(B_1^+ J)}$.

2.2.1. Complexity reduction by exploiting shift-invariance

The aforementioned method of applying the Greens operators, or solving for the scattered fields, requires the computationally intensive task of computing this large matrix multiplication, which scales quadratically with the amount of pixels in the imaging domain.

One might have noticed that the integral formulations in all Greens operators, resemble convolution integrals. The difference from the formulations present in these Greens operators, is that the Greens functions are functions of 2 variables ($\mathbf{r}$ and $\mathbf{r}'$), while the standard convolution integral must have this function as the difference between the two, making the Greens function spatially (or shift-) invariant. Due to the symmetry present in the definition of the electric and magnetic field Greens functions (Eq. 2.6, 2.14), it is possible to write them as functions of this difference. The integral form for the electric field Greens operator then becomes:

$$\hat{E}_z^{\text{sca}}(\mathbf{r}) = k_0^2 \int_{\mathbf{r}' \in \mathbb{R}^2} \hat{g}^{EJ}(\mathbf{r} - \mathbf{r}') \hat{\mathbf{w}}(\mathbf{r}') \mathrm{d}\mathbf{r}', \tag{2.28}$$

which in discretized space can be solved more easily and efficiently through the convolution theorem for the Discrete Time Fourier Transform (DTFT). This DTFT (and its inverse) can be calculated efficiently by using

the Fast Fourier Transform (FFT). The magnetic field Greens operators can be transformed using the same method. This means this convolution can be calculated using:

$$\hat{E}_z^{\text{sca}}(\mathbf{r}) = k_0^2 \text{ifft}\left(\text{fft}\left(\hat{g}^{EJ}\right) \odot \text{fft}\left(\hat{\mathbf{w}}(\mathbf{r}')\right)\right), \tag{2.29}$$

where $\odot$ denotes the Hadamard product. This method of finding $\hat{E}_z^{\text{sca}}$, reduces the computational complexity from $\mathcal{O}(M^2N^2)$ for calculating the scattered field for all observation points by using the double Riemann sum, to $\mathcal{O}\left(MN\log(MN)\right)$, when using the Fast Fourier approach.

This optimization is only possible when the Greens function is of the spatially invariant form, where it can be written as the difference of the source and observation point. This transformation is only possible since the contrast-source is assumed to radiate in free-space, leading to the spatially invariant Greens function. The introduction of the RF-shielding into the Greens function will invalidate the assumption, resulting into reverting to the naive implementation of the Greens operators.

2.2.2. Accounting for the singularity

The Hankel function present in the Greens function for the electric field, has a singularity at $\mathbf{0}$, which occurs when the source and observation point are overlapping ($\mathbf{r} = \mathbf{r}'$). Integrating over this singularity in continuous space does not pose any issue, but when considering the discrete implementation of these integrals, this singularity will be stretched over the entire domain of a single pixel, providing a bad representation of the electric field of that pixel. This means this Green's function must be weakened, to provide a better representation for the electric field in- and near $\mathbf{r} = \mathbf{r}'$. This is achieved by replacing the source, which previously was defined as a delta of Dirac source, by a current source spanning a small circle with radius a[21](in 3 dimensions this would be a sphere with radius a). The amplitude of this current distribution is chosen such that its total contribution equals the contribution of the delta of Dirac source. This results in the expression of the weakened Greens function:

$$\hat{g}^{EJ,W}(\mathbf{r},\mathbf{r}') = -\frac{j}{2k_b a} J_1(k_b a) H_0^{(2)}(k_n|\mathbf{r}-\mathbf{r}'|), \tag{2.30}$$

with a self-patch element for the singularity at $\mathbf{r}' = \mathbf{r}$:

$$\hat{g}^{EJ,W}(\mathbf{r},\mathbf{r}'=\mathbf{r}) = -\frac{j}{2k_b a}\left(H_1^{(2)}(k_b a) - \frac{2j}{\pi k_b a}\right). \tag{2.31}$$

The Greens function for the magnetic field, also has this singularity. This singularity however is not only caused by the singularity in the Hankel function at $\mathbf{r} = \mathbf{r}'$, but also due to the division by 0 at $\mathbf{r} = \mathbf{r}'$. Applying the same weakening as for the electric field Greens function to the magnetic field Greens function results in:

$$\begin{aligned}\hat{\mathbf{g}}^{HJ,W}(\mathbf{r},\mathbf{r}') = &\frac{J_1(k_b a)}{2a}\frac{(y-y')}{||\mathbf{r}-\mathbf{r}'||}\frac{1}{(j\omega\mu)} H_1^{(2)}(k|\mathbf{r}-\mathbf{r}'|)\hat{x} + \\ &\frac{-J_1(k_b a)}{2a}\frac{(x-x')}{||\mathbf{r}-\mathbf{r}'||}\frac{1}{(j\omega\mu)} H_1^{(2)}(k|\mathbf{r}-\mathbf{r}'|)\hat{y},\end{aligned} \tag{2.32}$$

which still has a singularity at $\mathbf{r} = \mathbf{r}'$. Taking the limit towards the singularity, results in the self-patch element for the weakened magnetic field Greens function:

$$\hat{\mathbf{g}}^{HJ,W}(\mathbf{r},\mathbf{r}'=\mathbf{r}) = \mathbf{0}. \tag{2.33}$$

The methods proposed in this section will be applied to all Greens operators, but throughout the remainder of this report the superscript W will often be omitted for the sake of readability.

2.3. Optimization

With this discretized physical model of free-space sources, the optimization technique for finding the electrical properties can be discussed. The goal of the optimization algorithm now becomes to best fit the physical model to the measured data, while adhering to the physical equations, such that the parameters given by the optimization best describe the physical parameters.

It achieves this by optimizing over the contrast source and the contrast function alternatingly. The optimization algorithm achieves this by minimizing a cost function, which penalizes the mismatch between the measured data and the modeled data, and which introduces a penalty when the modeled data does no longer adhere the physical equations.

2.3.1. Cost functions

The first part of the cost function introduces a penalty when there is a mismatch between the measured and modeled fields. This modeled field B_1^+ is calculated by applying the data-operator on the contrast source (Eq. 2.23), such that it can be used to minimize the difference between the measured and simulated field given by the data-residual:

$$\rho = \hat{B}_1^{+;\text{sca}} - \mathscr{G}_{B_1^+}\{\hat{\mathbf{w}}\}. \tag{2.34}$$

The cost function corresponding to this data mismatch is then given by:

$$F_D(\mathbf{w}) = \frac{\left|\left|\rho\right|\right|_{\mathbb{D}}^2}{\left|\left|\hat{B}_1^{+;\text{sca}}\right|\right|_{\mathbb{D}}^2} = \frac{\left|\left|\hat{B}_1^{+;\text{sca}} - \mathscr{G}_B\{\hat{\mathbf{w}}\}\right|\right|_{\mathbb{D}}^2}{\left|\left|\hat{B}_1^{+;\text{sca}}\right|\right|_{\mathbb{D}}^2}. \tag{2.35}$$

The second criterion was making sure that the reconstruction would still adhere to Maxwell's equation. This is achieved by minimizing the discrepancy between the modeled scattered field calculated by the object operator, the total field stored in the contrast source, and the (assumed to be known) incident electric field. The this discrepancy is given by the object-residual:

$$r = \hat{\chi}\left(\hat{\mathbf{E}}^{\text{inc}} + \mathscr{G}_E\{\hat{\mathbf{w}}\}\right) - \hat{\mathbf{w}} \tag{2.36}$$

This object-residual can now be used to define the object cost function:

$$F_O(\hat{\mathbf{w}}, \hat{\chi}) = \frac{||r||_{\mathbb{D}}^2}{\left|\left|\hat{\chi}\hat{\mathbf{E}}^{\text{inc}}\right|\right|_{\mathbb{D}}^2} = \frac{\left|\left|\hat{\chi}\left(\hat{\mathbf{E}}^{\text{inc}} + \mathscr{G}_E\{\hat{\mathbf{w}}\}\right) - \hat{\mathbf{w}}\right|\right|_{\mathbb{D}}^2}{\left|\left|\hat{\chi}\hat{\mathbf{E}}^{\text{inc}}\right|\right|_{\mathbb{D}}^2}. \tag{2.37}$$

Note that the normalization of the object cost function is dependent on the contrast function, leading to a different cost function at every iteration.

There are different methods of using these cost-functionals to optimize for the electrical properties. Strategies like naive CSI-EPT first optimize for the data cost-functional, followed by optimizing for the object-functional[22]. There is traditional CSI-EPT, which optimizes for the sum of the two cost-functionals, and there are regularized CSI-EPT strategies which scale this sum with another regularization cost-functional, such as total-variation. For now, the super-position of the object and the data function will be used as the total cost function leading to:

$$F(\hat{\mathbf{w}}, \hat{\chi}) = F_D(\hat{\mathbf{w}}) + F_O(\hat{\mathbf{w}}, \hat{\chi}) \tag{2.38}$$

Now the goal of the CSI-EPT algorithm becomes to minimize this cost-function to find the model parameters $\hat{\mathbf{w}}$ and $\hat{\chi}$ such that the resulting fields best match the measured fields, while still being able to adhere to Maxwell's equations.

2.3.2. Nonlinear conjugate gradient descent

In CSI-EPT, the aforementioned cost functions will be optimized for the contrast source and contrast function alternatingly. The contrast source will be optimized for using a nonlinear conjugate gradient (NCG) descent method, after which the contrast function will be determined using a least squares method. The contrast source in nonlinear conjugate gradient descent is updated according to:

$$\hat{\mathbf{w}}^{[n]} = \hat{\mathbf{w}}^{[n-1]} + \alpha^{[n]} v^{[n]}, \tag{2.39}$$

where $v^{[n]}$ denotes the update direction of iteration n, and $\alpha^{[n]}$ the step length. The bracketed superscripts denotes the data of the iteration indexed by the number between the brackets.

In the nonlinear conjugate gradient method, the update direction can be calculated using different methods; this thesis chose the Polak-Ribiere conjugate gradient update direction:

$$v^{[n]} = \nabla F^{[n]} + \frac{\text{Re}\left\{\langle \nabla F^{[n]}, \nabla F^{[n]} - \nabla F^{[n-1]} \rangle_{\mathbb{D}}\right\}}{\left|\left|\nabla F^{[n-1]}\right|\right|_{\mathbb{D}}^2} v^{[n-1]}, \tag{2.40}$$

where $\nabla F^{[n]}$ is the gradient with respect to the contrast source, and $\langle\cdot,\cdot\rangle_{\mathbb{D}}$ denotes the inner product over domain $\mathbb{D}$. The update direction at iteration 0 is $v^{[0]} = \mathbf{0}$. This gradient with respect to the contrast source, according to[23], can be written as:

$$\nabla F^{[n]} = -\frac{\mathscr{G}^{\dagger}_{B_1^+}\left\{\rho^{[n-1]}\right\}}{\left|\left|\hat{B}_1^+\right|\right|^2} - \frac{r^{[n-1]} - \mathscr{G}^{\dagger}_{E}\left\{\overline{\hat{\chi}^{[n-1]}} r^{[n-1]}\right\}}{\left|\left|\hat{\chi}^{[n]}\hat{E}^{\text{inc}}\right|\right|^2}, \tag{2.41}$$

where $\mathscr{G}^{\dagger}_{E,B_1^+}\{\cdot\}$, denote the adjoint operators of the electric and magnetic Greens operators. When using the matrix implementation for the Greens operators ($\mathbb{G}^{EJ}$, $\mathbb{G}^{(B_1^+J)}$), the adjoints are defined as the Hermitian of the matrices (conjugate-transpose); for the adjoint for the efficient implementation of the Greens operators (as given in Sec. 2.2.1) is shown in Algorithm 1.

With this update direction, the step-length to update the contrast source can be calculated by performing the line-search over α to find the minimum of the cost function using the previous contrast. This minimum can be calculated explicitly[23], resulting in:

$$\alpha^{[n]} = \arg\min_{\alpha}\left[F\left(\hat{\mathbf{w}}^{[n-1]} + \alpha v^{[n]}, \hat{\chi}^{[n-1]}\right)\right] = \frac{\text{Re}\left[\langle \nabla F^{[n]}, v^{[n]}\rangle\right]}{\frac{\left|\left|\mathscr{G}_B\{v^{[n]}\}\right|\right|^2}{\left|\left|\hat{B}_1^{+,\text{inc}}\right|\right|^2} + \frac{\left|\left|v^{[n]} - \hat{\chi}^{[n-1]}\mathscr{G}_E\{v^{[n]}\}\right|\right|^2}{\left|\left|\hat{\chi}^{[n-1]}\hat{E}^{\text{inc}}\right|\right|^2}} \tag{2.42}$$

With the update direction $v^{[n]}$, and step length $\alpha^{[n]}$, the contrast source can be update using Eq. 2.39. This, however, still needs an initialization of the contrast source $w^{[0]}$. This initialization step is crucial in CSI-EPT, as this can cause or prevent the algorithm the converge to a local minimum[24]. This initialization can be improved by including *a priori* knowledge. This thesis assumes no prior knowledge is available, thus will use an initialization based on back propagation:

$$\hat{\mathbf{w}}^{[0]} = \frac{\left|\left|\mathbb{G}^{(B_1^+J)\dagger}\hat{B}_1^+\right|\right|^2_{\mathbb{D}}}{\left|\left|\mathbb{G}^{(B_1^+J)}\mathbb{G}^{(B_1^+J)\dagger}\hat{B}_1^+\right|\right|^2_{\mathbb{D}}}\mathbb{G}^{(B_1^+J)\dagger}\hat{B}_1^+. \tag{2.43}$$

2.3.3. Reconstruction

This updated contrast source can be used to calculated the electric and magnetic scattered fields using their respective Greens operators. Since the incident fields are assumed to be known, by either simulation or imaging an empty MRI-machine, the total fields can be calculated easily.

Recall that the contrast source was the product of the contrast function (containing all electric properties) and the total electric field. This means the contrast function can be approximated by solving the minimum square error of the difference between the contrast source, and this product. This results in:

$$\hat{\chi}^{[n]} = \arg\min_{\hat{\chi}}\left|\left|\hat{\mathbf{w}}^{[n]} - \hat{\chi}\hat{\mathbf{E}}^{[n]}\right|\right|^2_D = \frac{\hat{\mathbf{w}}^{[n]}\left(\hat{\mathbf{E}}^{[n]}\right)^H}{\left|\left|\hat{\mathbf{E}}^{[n]}\right|\right|^2_{\mathbb{D}}} \tag{2.44}$$

Finally, the electrical properties of interest can be recovered from this contrast function, due to the independence of these electrical properties in the real and imaginary part, as shown in Eq. 2.19

$$\sigma = -\omega\epsilon_0\text{Im}(\hat{\chi}^{[n]}) \qquad \text{and} \qquad \epsilon_r = \text{Re}(\hat{\chi}^{[n]}) + 1. \tag{2.45}$$

The standard two-dimensional CSI-EPT algorithm as described in this chapter is summarized in Algorithm 2.

Algorithm 1 Adjoint convolution theorem based Greens operator $\hat{G}$, as done in Matlab's implementation[25]

Require:
Spectral matrix $\hat{G}$

$G \leftarrow \text{ifft2}(\hat{G})$
$G \leftarrow \text{rot90}(G, 2)$
$G \leftarrow \text{conj}(G)$
$G \leftarrow \text{circshift}(G, [1, 1])$
$\hat{G}^{\dagger} \leftarrow \text{fft2}(G)$

Algorithm 2 General algorithm of 2D CSI-EPT

Calculate the incident fields $\hat{\mathbf{E}}^{\text{inc}}$, $\hat{\mathbf{B}}_1^{+,\text{inc}}$, $\hat{\mathbf{B}}_1^{-,\text{inc}}$
Initial guess $\hat{\mathbf{w}}^{[0]}$ using backpropagation

for $n = 1, 2, \ldots$ **do**
Update contrast-source using NCG
$g^{[n]} = \nabla F\left(\hat{\mathbf{w}}^{[n-1]}, \hat{\chi}^{[n-1]}\right)$
$\mathbf{v}^{[n]} \leftarrow g^{[n]} + \frac{\text{Re}\left[\langle (g^{[n]} - g^{[n-1]}), g^{[n]} \rangle\right]}{\|g^{[n]}\|^2} g^{[n-1]}$
$\alpha^{[n]} \leftarrow \frac{-\text{Re}\left[\langle g^{[n]}, \mathbf{v}^{[n]} \rangle\right]}{\eta_S \|\mathscr{G}_{\text{dat}}\{\mathbf{v}^{[n-1]}\}\|^2 + \eta_D^{[n]} \|\mathbf{v}^{[n]} - \hat{\chi}^{[n-1]} \mathscr{G}_{\text{obj}}\{\mathbf{v}^{[n]}\}\|^2}$
$\hat{\mathbf{w}}^{[n]} \leftarrow \hat{\mathbf{w}}^{[n-1]} + \alpha^{[n]} \mathbf{v}^{[n]}$

Update fields using contrast-source
$\hat{E}_z^{[n]} \leftarrow \hat{E}_z^{\text{inc}} + \mathscr{G}_E\{\hat{\mathbf{w}}^{[n]}\}$
$\hat{B}_1^{+,[n]} \leftarrow \hat{B}_1^{+,\text{inc},[n]} + \mathscr{G}_{B_1^+}\{\hat{\mathbf{w}}^{[n]}\}$
$\hat{B}_1^{-,[n]} \leftarrow \hat{B}_1^{-,\text{inc},[n]} + \mathscr{G}_{B_1^-}\{\hat{\mathbf{w}}^{[n]}\}$

Update contrast-function using MLS
$\hat{\chi}^{[n]} \leftarrow \frac{\hat{\mathbf{w}}^{[n]} (\hat{\mathbf{E}}^{[n]})^H}{\|\hat{\mathbf{E}}^{[n]}\|^2}$

Calculate cost function
$F^{[n]}\left(\hat{\mathbf{w}}^{[n]}, \hat{\chi}^{[n]}\right) = \frac{\left|\left|\hat{B}_1^{+;\text{sca}} - \mathscr{G}_B\{\hat{\mathbf{w}}^{[n]}\}\right|\right|_{\mathbb{D}}^2}{\left|\left|\hat{B}_1^{+;\text{sca}}\right|\right|_{\mathbb{D}}^2} + \frac{\left|\left|\hat{\chi}^{[n]}\left(\hat{\mathbf{E}}^{\text{inc}} + \mathscr{G}_E\{\hat{\mathbf{w}}^{[n]}\}\right) - \hat{\mathbf{w}}^{[n]}\right|\right|_{\mathbb{D}}^2}{\left|\left|\hat{\chi}^{[n]} \hat{\mathbf{E}}^{\text{inc}}\right|\right|_{\mathbb{D}}^2}$

end for

3

RF-Shielding

The physical model, and the techniques for reconstruction the electrical properties in Chapter 2, only use the (rough) mirror-source approximation of the RF-shield present around the birdcage coil. In this method the shielding is only accounted for in the incident field, by a (modified) first order approximation, and disregarding the effects of the shielding in the scattered field. This approximation inherently leads to an error, especially when considering that all relevant information about the patient's tissue is given by these scattered fields. For large coils, when both the shielding and rungs are located far from the patient, this assumption becomes more valid. However, when considering birdcage coils for smaller objects, such as a head or limb, this shielding is most definitely non-negligible.

This chapter will therefore introduce the changes that must be made to the CSI-EPT algorithm described in Chapter 2, to account for this shielding analytically for E-polarized fields. This results in fully analytic expressions for the electromagnetic fields in the shielded MR-scanner, where the only assumption is that the fields are truly E-polarized.

This starts with first introducing how the shielding affects the physical model, and consequently the Greens functions. Thereafter, the consequences to the implementation of the discretization and optimization are discussed. The altered version, which accounts for this shielding, will be referred to as the *shielded CSI-EPT* method.

3.1. Physics model

The presence of the RF-shielding alters how the sources (both the current-sources for the incident field and the contrast sources for the scattered field) radiate in the space within the shielding. The highly conductive RF-shield can still be assumed to be made of Perfect Electric Conductor (PEC), meaning the tangential component of the electric field must still vanish PEC's surface. Instead of constructing the (first-order modified) mirror-sources, the Greens functions can be modified to fully analytically account for the RF shielding.

While this presence of the PEC enclosure changes the setup, the electromagnetic fields must still adhere to Maxwell's equations. Using the methods described in Sec. 2.1, the Helmholtz equation for this system can be described, with the addition of the Dirichlet boundary condition of 0 at the PEC's surface, and is given by:

$$\begin{aligned} \left(\partial_x^2 + \partial_y^2\right)\hat{E}_z(\mathbf{r}) + k_0\hat{E}_z(\mathbf{r}) &= -\hat{f} && \mathbf{r}\in\Omega \\ \hat{E}_z(\mathbf{r}) &= 0 && \mathbf{r}\in\partial\Omega, \end{aligned} \tag{3.1}$$

where Ω describes the region within the PEC enclosure, and $\partial\Omega$ its boundary. This Helmholtz equation has a similar solution as the unshielded one, with the exception of a different Greens function in the integral. The solution for the electric field is given by:

$$\hat{E}_z(\mathbf{r}) = \int_{\mathbf{r}'\in\Omega} \hat{g}_{sh}^{EJ}(\mathbf{r},\mathbf{r}')\,\hat{f}(\mathbf{r}')\,\mathrm{d}\mathbf{r}'. \tag{3.2}$$

This equation now uses the modified Greens function $\hat{g}_{sh}^{EJ}$ which describes the steady-state electric field inside this PEC enclosure. This Greens function is constructed such that it is the superposition of the unshielded

(radiating in free-space) Greens function $\hat{g}^{EJ}$, as given in Chapter 2, and the correction term $\hat{p}^{EJ}$ which corrects for all effects this shield has on the electric field. This shielded Greens function for the electric field is given by:

$$\hat{g}^{EJ}_{sh}\left(\mathbf{r},\mathbf{r}'\right) = \hat{g}^{EJ}\left(\mathbf{r},\mathbf{r}'\right) + \hat{p}^{EJ}\left(\mathbf{r},\mathbf{r}'\right). \tag{3.3}$$

Using the linearity in the Helmholtz equation, one can define a Helmholtz equation for just this correction term $\hat{p}^{EJ}$. This Helmholtz equation is a result from subtracting the homogeneous Helmholtz equation from Eq. 2.4, from the shielded Helmholtz equation of Eq. 3.1. For the homogeneous setting, the sources radiate an (tangential) electric field across the PEC shields' surface, which must be counteracted exactly by the correction terms, since the tangential field at the PEC's surface has to be 0. This new boundary value problem then becomes:

$$\begin{aligned} \nabla^2 \hat{p}^{EJ}(\mathbf{r},\mathbf{r}') + k^2 \hat{p}^{EJ}(\mathbf{r},\mathbf{r}') = 0 \qquad & \mathbf{r} \in \Omega \\ \hat{p}^{EJ}(\mathbf{r},\mathbf{r}') = -\hat{g}^{EJ}_{fs}(\mathbf{r},\mathbf{r}') \qquad & \mathbf{r} \in \partial\Omega. \end{aligned} \tag{3.4}$$

This boundary value problem can be solved analytically[26][27], which is achieved by an eigenfunction expansion using separation of variables in the cylindrical coordinate system, and is given by:

$$\hat{p}^{EJ}\left(\mathbf{r},\mathbf{r}'\right) = \frac{A_0}{2} J_0\left(kr\right) + \sum_{n=1}^{\infty} \left(A_n(\mathbf{r}') J_n\left(kr\right)\cos\left(n\theta\right) + B_n\left(\mathbf{r}'\right) J_n\left(kr\right)\sin\left(n\theta\right)\right), \tag{3.5}$$

where r and θ denote the polar coordinate representation of $\mathbf{r}$, and the Fourier expansion coefficients A_n and B_n for all n (including 0) are given by:

$$A_n\left(\mathbf{r}'\right) = \frac{-1}{4jJ_n\left(kR_{sh}\right)} \left[J_n\left(kr'\right) e^{-jn\theta'} H^{(2)}_n\left(kR_{sh}\right) + J_{-n}\left(kr'\right) e^{jn\theta'} H^{(2)}_{-n}\left(kR_{sh}\right)\right] \tag{3.6a}$$

$$B_n\left(\mathbf{r}'\right) = \frac{-1}{4J_n\left(kR_{sh}\right)} \left[J_n\left(kr'\right) e^{-jn\theta'} H^{(2)}_n\left(kR_{sh}\right) - J_{-n}\left(kr'\right) e^{jn\theta'} H^{(2)}_{-n}\left(kR_{sh}\right)\right], \tag{3.6b}$$

where R_{sh} denotes the radius of the RF-shield. Note that there is a discrepancy between the definition of B_n between [26] and [27]; Appendix B shows the derivation for the correct B_n term, as it is shown in Eq. 3.6b. Most literature provides an exception for the zero-th ('DC') Fourier expansion coefficient, while this thesis does not require this exception.

Substituting the definitions of A_n and B_n in Eq. 3.5 allows for a simplification of the definition of $\hat{p}^{EJ}(\mathbf{r},\mathbf{r}')$ (as shown in Appendix D) to:

$$\hat{p}^{EJ}(\mathbf{r},\mathbf{r}') = \sum_{n=-\infty}^{\infty} \frac{-H^{(2)}_n(kR_{sh}) J_n(kr) J_n(kr') \cos(n(\theta-\theta'))}{4jJ_n(kR_{sh})}. \tag{3.7}$$

This expression consists only of integer-order Bessel functions; the Hankel function of the second kind is a linear combination of Bessel functions of the first and second kind, and will therefore often be denoted as a Bessel function of the third kind. By applying [28, Eq. 9.1.5], this two-sided infinite sum can now be reduced to a one-side infinite sum as:

$$\hat{p}^{EJ}(\mathbf{r},\mathbf{r}') = \frac{-H^{(2)}_0(kR_{sh}) J_0(kr) J_0(kr')}{4jJ_0(kR_{sh})} + \sum_{n=1}^{\infty} \frac{-H^{(2)}_n(kR_{sh}) J_n(kr) J_n(kr') \cos(n(\theta-\theta'))}{2jJ_n(kR_{sh})}, \tag{3.8}$$

Upon further inspection, the imaginary parts of $\hat{g}^{EJ}$ and $\hat{p}^{EJ}$ are equal in size but opposite in sign, as shown in Appendix D. This suggests that any (contrast)source located within the enclosed space produces a standing wave in this space, and the only phase which can be introduced is the phase at which the source is excited. Given that this Greens function does not have an imaginary part, it can be written as the sum of only the real parts of the free-space Greens function and the real part of the correction term $\hat{p}(\mathbf{r},\mathbf{r}')$, resulting in:

$$\hat{g}^{EJ}_{sh}(\mathbf{r},\mathbf{r}') = \mathrm{Re}\left\{g^{EJ}_{fs}(\mathbf{r},\mathbf{r}')\right\} + \mathrm{Re}\left\{\hat{p}^{EJ}(\mathbf{r},\mathbf{r}')\right\} = \frac{-1}{4} Y_0(k|\mathbf{r}-\mathbf{r}'|) + \sum_{n=-\infty}^{\infty} \frac{Y_n(kR_{sh})}{4J_n(kR_{sh})} J_n(kr) J_n(kr') \cos(n(\theta-\theta')), \tag{3.9}$$

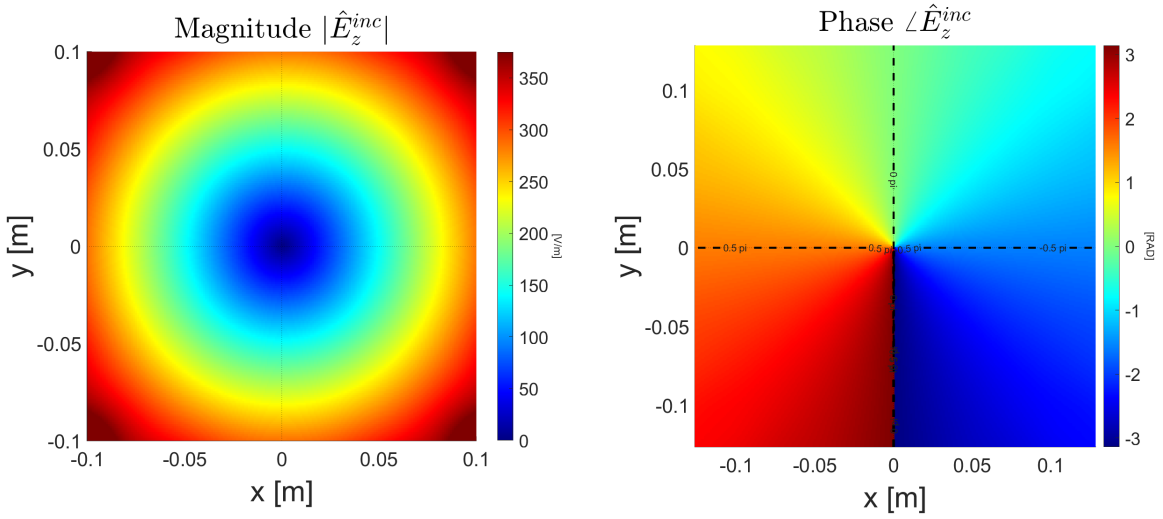

(a) Magnitude of the incident electric field

(b) Phase of the incident electric field

Figure 3.1: Incident electric field generated using g_{sh}^{EJ} in a head sized birdcage coil. This image is generated using an inversion region of 256 × 256 pixels where each pixel is 1mm × 1mm. This figure shows the circular polarization transmitted by the birdcage coil, with a zero in the center of the birdcage coil.

where $Y_n(\cdot)$ denotes the n^{th}-order Bessel function of the second kind. This absence of phase in the expression of the electric field Greens function becomes directly apparent when comparing the incident electric field generated using this shielded Greens function to the incident field generated by the free-space Greens function using 'mirror-sources'. The incident electric field can be calculated using Eq. 3.2 using just the currents flowing through the line-currents of the birdcage coil (Eq. 2.8), and is given by:

$$\hat{E}_z^{\text{inc}}(\mathbf{r}) = -\alpha\, j\omega\mu_0 \sum_{n=1}^{N_A} \hat{g}_{sh}^{EJ}(\mathbf{r}, \mathbf{r}_A^{[n]}). \tag{3.10}$$

Fig. 3.1 shows the incident electric field calculated using the shielded Greens function, which shows the $-\pi, \pi$ crossover on the negative y-axis. This crossover for the implementation with mirror-source occurs at a slight phase shift, as shown in Fig. 2.2, showing a clear difference between the two representations.

Now that this electric field inside the PEC enclosed birdcage coil is described completely analytically, the description of the magnetic field can be derived. Using the two-dimensional form of Ampere-Maxwell's law (Eq. 2.2), the magnetic field is given by the scaled curl of the electric field, which also be applied to the Greens functions as:

$$\hat{\mathbf{g}}_{sh}^{HJ}(\mathbf{r}, \mathbf{r}') = \tfrac{1}{j\omega\mu_0}\partial_y \hat{g}_{sh}^{EJ}(\mathbf{r}, \mathbf{r}')\hat{x} + \tfrac{-1}{j\omega\mu_0}\partial_x \hat{g}_{sh}^{EJ}(\mathbf{r}, \mathbf{r}')\hat{y} \tag{3.11}$$

By using the distributive properties of the derivatives, this can be split in the curl of the unshielded Greens function (which is derived in Chapter 2), and the curl of the correction term $\hat{p}^{EJ}$. Solving these derivatives analytically results in the expression for the correction terms for the magnetic field of:

$$\hat{\mathbf{p}}^{HJ}(\mathbf{r}, \mathbf{r}') = \sum_{n=-\infty}^{\infty} \frac{H_n^{(2)}(kR_{sh})}{4jJ_n(kR_{sh})} \frac{J_n(kr')}{j\omega\mu_0} \times \tag{3.12}$$
$$\left[\begin{array}{l} \Big(-\sin(\theta)\, k\,(J_{n-1}(kr) - J_{n+1}(kr))\cos\big(n(\theta-\theta')\big) + \frac{\cos(\theta)}{r} J_n(kr)\, n \sin\big(n(\theta-\theta')\big)\Big)\hat{x} + \\ \Big(\cos(\theta)\, k\,(J_{n-1}(kr) - J_{n+1}(kr))\cos\big(n(\theta-\theta')\big) + \frac{\sin(\theta)}{r} J_n(kr)\, n \sin\big(n(\theta-\theta')\big)\Big)\hat{y} \end{array} \right].$$

Combining Eq. 2.14 and Eq. 3.12, the Greens function for the magnetic field in presence of the RF-shield can be found easily. The corresponding incident magnetic field (derived analogously to Eq. 3.10) is shown in Fig. 3.2.

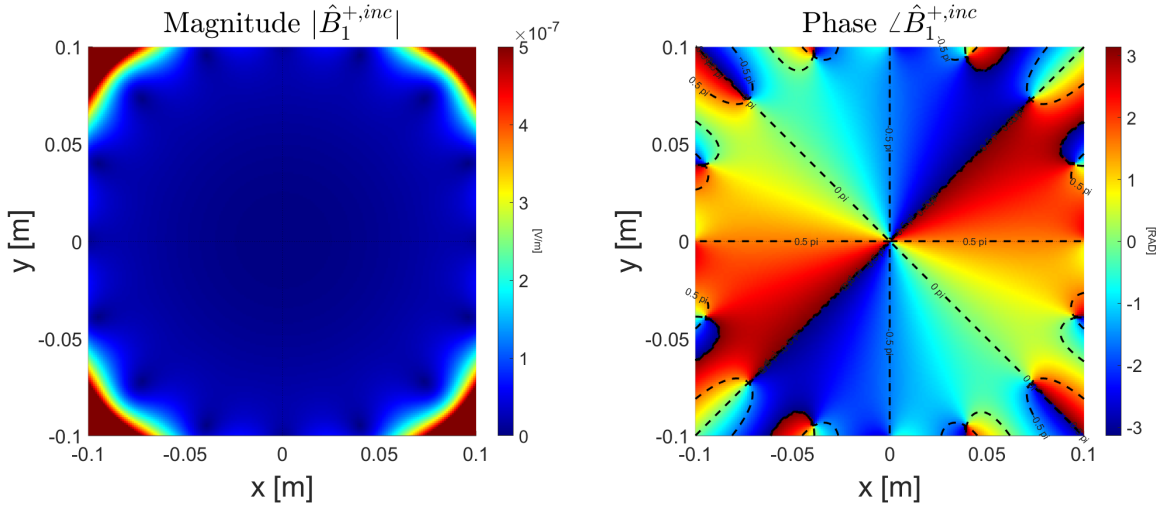

(a) Magnitude of the incident magnetic $\hat{B}_1^+$ field

(b) Phase of the incident magnetic $\hat{B}_1^+$ field

Figure 3.2: Incident magnetic field generated using g_{sh}^{EJ} in a head sized birdcage coil. This image is generated using an inversion region of 256 × 256 pixels where each pixel is 1mm × 1mm. This figure shows the circular polarization transmitted by the birdcage coil, with a zero in the center of the birdcage coil.

3.1.1. Truncating the correction terms

These analytic descriptions of the shielded electric and magnetic field Greens functions include an infinite sum of correction terms, which inherently make the problem intractable. A truncation of this sum is therefore required, given that this truncated sum would converge to the same result as the full sum within a predefined tolerance. The eigenfunction expansion used for solving the boundary value expansion of Eq. 3.4, results in the converging[29] series of eigenfunctions of Eq. 3.5. This convergence rate of this sum is dependent on location of the observation point $\mathbf{r}$ and the source $\mathbf{r}'$. Figure 3.3 shows the maximum contribution of the next term n of $\hat{p}^{EJ}$, when both the observation and source point are located on a circle of radius r. This figure can now be used to choose a truncation for this sum T, given a chosen error tolerance.

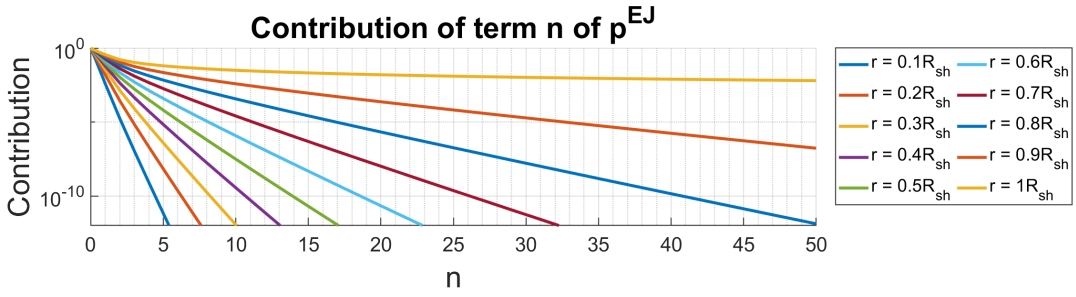

Figure 3.3: Contribution of the next term n in the sum of correction terms in $\hat{p}^{EJ}$. This figure shows that for observation- and source locations close to the origin the sum converges very fast, but this sum converges very slowly to points close to the shield's surface.

A tolerance often used is allowing for an error in the order of 10^{-10}[26]. When considering a birdcage coil for which the rungs are located at approximately 80% of the radius of the RF-shielding, means this sum can be truncated at $T = 40$. For a more probable convergence of this sum some extra terms will be taken into account, leading to a truncation (which for the remainder of this report) is $T = 50$. While this method only shows the truncation based on the contribution of the correction terms of $\hat{p}^{EJ}$, a similar approach can be taken for the contributions of $\hat{\mathbf{p}}^{HJ}$, resulting in the same conclusion and the same truncation bound of $T = 50$.

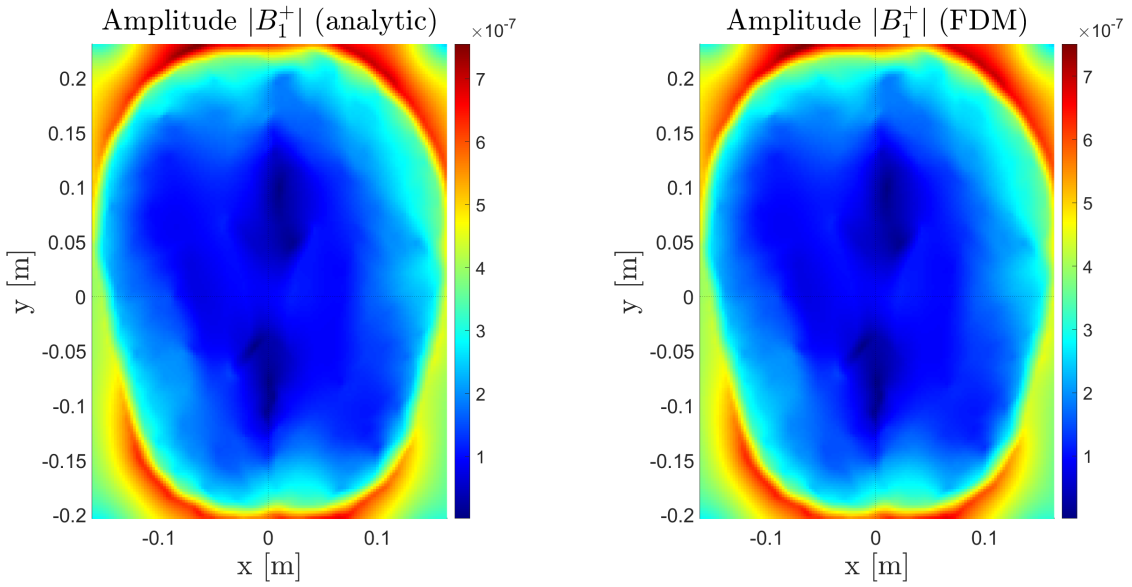

(a) Total magnetic field B_1^+ derived using the analytical Greens operators of Eq. 3.12

(b) Total magnetic field B_1^+ approximated using FDM as shown in Eq. 3.13

Figure 3.4: Comparison between the B_1^+-fields derived using the analytical expressions, and approximated by using an FDM. On the naked eye the difference is hardly noticeable, but near tissue boundaries this difference becomes more apparent. These magnetic fields are evaluated for patient M1, slice 80.

3.1.2. Verification of the analytical shielded magnetic field expression

Prior to this analytical description of the electric and magnetic field, the magnetic field was determined by approximating the magnetic field from the electric field. Instead of calculating the exact gradients of Eq. 3.11, they were approximated using a first order finite difference method. This first order finite difference method for the gradient is defined as[30]:

$$\begin{aligned} \partial_x g_{sh}^{EJ} &\approx \frac{g_{sh}^{EJ}(\mathbf{r}_{i+1,j},\mathbf{r}') - g_{sh}^{EJ}(\mathbf{r}_{i-1,j},\mathbf{r}')}{2\delta_x} \\ \partial_y g_{sh}^{EJ} &\approx \frac{g_{sh}^{EJ}(\mathbf{r}_{i,j+1},\mathbf{r}') - g_{sh}^{EJ}(\mathbf{r}_{i,j-1},\mathbf{r}')}{2\delta_y}. \end{aligned} \tag{3.13}$$

The expected error this first order approximation introduces is in the order of sampling size $\delta_{x,y}^2$, can now be reduced to the tolerance chosen in the truncation of the sum of correction terms.

This comparison serves two purposes; the first of which is to verify the derived analytical Greens function is certainly correct, which is valid when the differences between the two implementations becomes small for slow-varying regions. This second one is to show the error which is introduced by approximating this field instead of applying the analytical expression.

Figure 3.4 shows the magnetic fields derived using these two methods. At first glance, these figures appear to be equal. As stated before for slow-varying regions, this difference should be negligible, but when considering tissue boundaries, which introduce a significant difference in electrical properties, and therefore the electric field will also rapidly change. These high derivatives are more difficult to capture with the finite difference method. Figure 3.5 shows the error introduced in this image for all the field strengths in this image. For the slow-varying fields electric fields, resulting in low magnetic fields, the error introduced by the FDM is very low. The average error, while slightly trending down as the field strength increases, is still very close to 0, having a standard deviation smaller than 10^{-8}. When approaching the boundary between tissue, this electric field will vary much faster. In Fig. 3.5, this is shown in the region where the true B_1^+ field becomes larger than 1.5. From here on, the average error introduced will follow the same trend as in for the slow-varying regions, but the variance of these errors increases significantly. The errors, as expected, are mostly negative showing an underestimation of the B_1^+ field at these tissue boundaries. The largest errors introduced here are of the order of 10% of the original signal, which shows that analytical expressions can provide a much better representation of these fields for tissue boundaries.

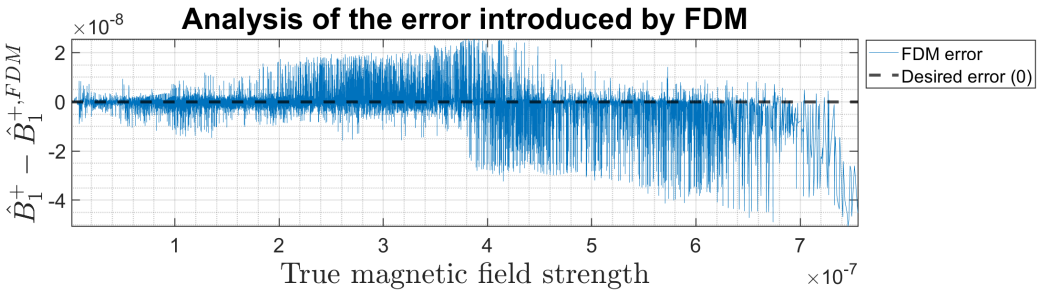

Figure 3.5: Error introduced by the FDM for different field strengths present in the Magnetic field of patient M1, slice 80

The finite difference method used here is of the first order, which means it is the most simple form of approximating this gradient. This method is most commonly used due to its ease of implementation and low computational complexity, at the cost of these large 'FDM' errors. While higher order finite difference methods exist, those often become instable when the solution is non-smooth. These higher order methods also require more complex sampling schemes than just using the direct neighbors, which lead to very complicated implementations near boundaries.

The first order finite difference method is the basis of many local methods like Helmholtz-EPT, which solve the Maxwells equations in the differential form using these FDM methods. These differential based methods usually perform poorly at tissue boundaries, or noisy environments where rapidly changing fields become more prevalent. The analytical method proposed here should omit these issues at tissue boundaries, since the analytical expression of the fields at these boundaries is now known.

3.2. Discretization

The discretization of the space, whether using the 'unshielded', or shielded description of the MR-scanner remains the same, using the midpoint-sampling convention for all pixels, as described in Sec. 2.2. While this new description does not affect the discretization, it does affect the implementation of the discretized Greens operators.

In the unshielded description of the scanner, the Greens function could be described using linear spatially invariant Greens functions (in the field of signal processing these would often be described as linear time invariant (LTI) filters), and therefore could be implemented much more efficiently using the convolution theorem. The descriptions given for the fully shielded Green's functions, however, do not have this property, and therefore the inefficient, naive method of solving for the Greens operators by means of the double Riemann sum must be used (Eq. 2.27), having the computational complexity of $\mathcal{O}(M^2N^2)$. For smaller inversion regions, it is possible to calculate for these Greens operators, but for larger inversion regions this often becomes impossible due to the increased computational load. This section will therefore propose a method of reducing the complexity of solving for these Greens operators by exploiting the fact that the kernel is degenerate or separable.

3.2.1. Complexity reduction using separable kernel

Given the linear combination of the unshielded Greens function and the correction terms, the full Greens function can also be solved for in those two parts. For the unshielded Greens function a very efficient method of solving has been described in Sec. 2.2.1, using the Fast Fourier Transforms (FFTs) reducing that computational complexity to $\mathcal{O}(MN\log(MN))$. This method will from now on be used again to solve for the unshielded term in the shielded Greens function, whereas for the correction terms a more efficient method is required. This also implies that the shielded Greens function no longer follow Eq. 3.9 (where only the real parts are considered), but will be calculated as the sum of the two complex function $\hat{g}^{EJ}$ and $\hat{p}^{EJ}$.

The terms in $\hat{p}^{EJ}$ describe the parts which do not posses the spatial invariance property, which led to the convolution theorem no longer being applicable, thus another (efficient) method for it must be proposed. This means the electric field Greens operator can be defined as the sum of the efficient operator for the un-

shielded part of the shielded Greens function and the naive implementation for the correction terms:

$$\begin{aligned}\mathcal{G}_E\{\hat{\mathbf{w}}\}(\mathbf{r}) &= k_0^2 \text{ifft}\left(\text{fft}\left(\hat{g}^{EJ}\right) \odot \text{fft}\left(\hat{\mathbf{W}}\right)\right) + \mathbb{P}^{EJ}\,\text{vec}(\hat{\mathbf{W}}) \\ &= k_0^2 \text{ifft}\left(\text{fft}\left(\hat{g}^{EJ}\right) \odot \text{fft}\left(\hat{\mathbf{W}}\right)\right) \\ &\quad + \begin{bmatrix} \hat{p}^{EJ}(\mathbf{r}_{0,0},\mathbf{r}'_{0,0}) & \hat{p}^{EJ}(\mathbf{r}_{0,0},\mathbf{r}'_{0,1}) & \dots & \hat{p}^{EJ}(\mathbf{r}_{0,0},\mathbf{r}'_{M-1,N-1}) \\ \hat{p}^{EJ}(\mathbf{r}_{0,1},\mathbf{r}'_{0,0}) & \hat{p}^{EJ}(\mathbf{r}_{0,1},\mathbf{r}'_{0,1}) & \dots & \hat{p}^{EJ}(\mathbf{r}_{0,1},\mathbf{r}'_{M-1,N-1}) \\ \vdots & \vdots & \ddots & \vdots \\ \hat{p}^{EJ}(\mathbf{r}_{M-1,N-1},\mathbf{r}'_{0,0}) & \hat{p}^{EJ}(\mathbf{r}_{M-1,N-1},\mathbf{r}'_{0,1}) & \dots & \hat{p}^{EJ}(\mathbf{r}_{M-1,N-1},\mathbf{r}'_{M-1,N-1}) \end{bmatrix} \begin{bmatrix} \hat{\mathbf{w}}_{0,0} \\ \hat{\mathbf{w}}_{0,1} \\ \vdots \\ \hat{\mathbf{w}}_{M-1,N-1} \end{bmatrix}.\end{aligned} \tag{3.14}$$

This method now includes both the convolution theorem method for the free-space component, as well as the naive implementation for the double Riemann sum using the large matrix multiplication for the correction terms. This implies a computational complexity of $\mathcal{O}(M^2N^2)$, is still required to calculate these operators. The complexity of this matrix multiplication, however, can be reduced significant by inspecting the solution for $\hat{p}^{EJ}$, in which one can show that the terms inside the sum can be decomposed to the multiplication of two functions; one only dependent on the observation point $\mathbf{r} = [r,\theta]^T$, and to other only dependent on the source location $\mathbf{r}' = [r',\theta']^T$. This results in:

$$\hat{p}^{EJ}(\mathbf{r},\mathbf{r}') = \frac{-H_0^{(2)}(kR_{sh})J_0(kr)J_0(kr')}{4jJ_0(kR_{sh})} + \sum_{n=1}^{T} \frac{-H_n^{(2)}(kR_{sh})}{8jJ_n(kR_{sh})}\left(J_n(kr)e^{jn\theta}J_n(kr')e^{-jn\theta'} + J_n(kr)e^{-jn\theta}J_n(kr')e^{jn\theta'}\right). \tag{3.15}$$

This separated form allows for the formation of $\mathbb{P}^{EJ}$ as the sum of $1+2T$ rank-1 matrices (where T is given by the truncation of the sum of p^{EJ}), without the loss of any information. The definition of $\mathbb{P}^{EJ}$ then becomes:

$$\begin{aligned}\mathbb{P}^{EJ} &= \frac{-H_0^{(2)}(kR_{sh})}{4jJ_0(kR_{sh})} \begin{bmatrix} J_0(kr_{0,0}) \\ J_0(kr_{0,1}) \\ \vdots \\ J_0(kr_{M-1,N-1}) \end{bmatrix} \begin{bmatrix} J_0(kr'_{0,0}) \\ J_0(kr'_{0,1}) \\ \dots \\ J_0(kr'_{M-1,N-1}) \end{bmatrix}^T \\ &\quad - \sum_{n=1}^{T} \frac{H_n^{(2)}(kR_{sh})}{8jJ_n(kR_{sh})} \begin{bmatrix} J_n(kr_{0,0})e^{jn\theta_{0,0}} \\ J_n(kr_{0,1})e^{jn\theta_{0,1}} \\ \vdots \\ J_n(kr_{M-1,N-1})e^{jn\theta_{M-1,N-1}} \end{bmatrix} \begin{bmatrix} J_n(kr'_{0,0})e^{-jn\theta'_{0,0}} \\ J_n(kr'_{0,1})e^{-jn\theta'_{0,1}} \\ \vdots \\ J_n(kr'_{M-1,N-1})e^{-jn\theta'_{M-1,N-1}} \end{bmatrix}^T \\ &\quad + \frac{H_n^{(2)}(kR_{sh})}{8jJ_n(kR_{sh})} \begin{bmatrix} J_n(kr_{0,0})e^{-jn\theta_{0,0}} \\ J_n(kr_{0,1})e^{-jn\theta_{0,1}} \\ \vdots \\ J_n(kr_{M-1,N-1})e^{-jn\theta_{M-1,N-1}} \end{bmatrix} \begin{bmatrix} J_n(kr'_{0,0})e^{jn\theta'_{0,0}} \\ J_n(kr'_{0,1})e^{jn\theta'_{0,1}} \\ \vdots \\ J_n(kr'_{M-1,N-1})e^{jn\theta'_{M-1,N-1}} \end{bmatrix}^T\end{aligned} \tag{3.16}$$

This can be written much more compact by introducing a few quantities; these are the column vectors in $\mathbb{P}^{EJ}$ (which are here denoted as transposed row vectors):

$$\begin{aligned}L_{1,n}^{EJ}(\mathbf{r}) &= \begin{bmatrix} J_n(kr_{0,0})e^{jn\theta_{0,0}} & J_n(kr_{0,1})e^{jn\theta_{0,1}} & \dots & J_n(kr_{M-1,N-1})e^{jn\theta_{M-1,N-1}} \end{bmatrix}^T \\ L_{2,n}^{EJ}(\mathbf{r}) &= \begin{bmatrix} J_n(kr_{0,0})e^{-jn\theta_{0,0}} & J_n(kr_{0,1})e^{-jn\theta_{0,1}} & \dots & J_n(kr_{M-1,N-1})e^{-jn\theta_{M-1,N-1}} \end{bmatrix}^T,\end{aligned} \tag{3.17}$$

where $L_{1,n}, L_{2,n} \in \mathbb{C}^{MN\times 1}$. The row vectors in $\mathbb{P}^{EJ}$ can be denotes as:

$$\begin{aligned}R_{1,n}(\mathbf{r}') &= \begin{bmatrix} J_n(kr'_{0,0})e^{-jn\theta'_{0,0}} & J_n(kr'_{0,1})e^{-jn\theta'_{0,1}} & \dots & J_n(kr'_{M-1,N-1})e^{-jn\theta'_{M-1,N-1}} \end{bmatrix} \\ R_{2,n}(\mathbf{r}') &= \begin{bmatrix} J_n(kr'_{0,0})e^{jn\theta'_{0,0}} & J_n(kr'_{0,1})e^{jn\theta'_{0,1}} & \dots & J_n(kr'_{M-1,N-1})e^{jn\theta'_{M-1,N-1}} \end{bmatrix},\end{aligned} \tag{3.18}$$

where $R_{1,n}, R_{2,n} \in \mathbb{C}^{1\times MN}$ and the scalars in front of the rank-1 matrices:

$$m_n = \frac{-H_n^{(2)}(kR_{sh})}{4jJ_0(kR_{sh})}. \tag{3.19}$$

These definition allow for the construction of $\mathbb{P}^{EJ}$ (without loss of accuracy) as a matrix multiplication of:

$$\mathbb{P}^{EJ} = \begin{bmatrix} L^{EJ}_{1,0} & L^{EJ}_{1,1} & L^{EJ}_{2,1} & L^{EJ}_{1,2} & L^{EJ}_{2,2} & \dots & L^{EJ}_{1,T} & L^{EJ}_{2,T} \end{bmatrix} \begin{bmatrix} 2m_0 & & & & & & & \\ & m_1 & & & & & & \\ & & m_1 & & & & & \\ & & & m_2 & & & & \\ & & & & m_2 & & & \\ & & & & & \ddots & & \\ & & & & & & m_T & \\ & & & & & & & m_T \end{bmatrix} \begin{bmatrix} R_{1,0} \\ R_{1,1} \\ R_{2,1} \\ R_{1,2} \\ R_{2,2} \\ \vdots \\ R_{1,T} \\ R_{2,T} \end{bmatrix} \tag{3.20}$$

$$= \mathbb{L}^{EJ}\mathbb{M}\mathbb{R},$$

where $\mathbb{L}^{EJ} \in \mathbb{C}^{MN\times(2T+1)}$, $\mathbb{M} \in \mathbb{C}^{(2T+1)\times(2T+1)}$, and $\mathbb{R} \in \mathbb{C}^{(2T+1)\times MN}$. Note that the first entry in these matrices describes the rank-1 matrix prior to the sum. This decomposition shows that the rank of $\mathbb{P}^{EJ}$ is equal the truncation bound for the sum in $\hat{p}^{EJ}$.

Using this decomposition of the matrix $\mathbb{P}^{EJ}$, of which all the matrices can be calculated prior to the iterative algorithm, solving for the electric field Greens operator as shown in Eq. 3.14 can now be done using:

$$\mathscr{G}_E\{\mathbf{w}\}(\mathbf{r}) = k_0^2 \text{ifft}\left(\text{fft}\left(\hat{g}^{EJ}\right) \odot \text{fft}\left(\mathbf{w}\right)\right) + \mathbb{L}^{EJ}\left(\mathbb{M}\mathbb{R}\,\text{vec}(\hat{\mathbf{W}})\right), \tag{3.21}$$

which means the large matrix multiplication with the computational complexity of $\mathscr{O}(M^2N^2)$ can be reduced to a complexity of $\mathscr{O}\left(MN\log(MN) + MN(2T+1) + (2T+1)MN\right) = \mathscr{O}\left(MN\log(MN) + MNT\right)$. Given that the truncation T is independent on, and much smaller than the size of the inversion region denoted by MN, a significant reduction in complexity can be reached. These operators can be defined in a similar for the magnetic field components. Since only the $\mathbb{L}^{EJ}$ matrix has a dependence on the observation point $\mathbf{r}$, the operator for the correction term for the magnetic fields can be found much simpler since only the (scaled) curl with respect to this $\mathbb{L}^{EJ}$-matrix is required. The independence of the observation point allows for the reusing of the $\mathbb{M}\mathbb{R}$ matrices. Taking this scaled curl, or applying the gradients as shown in Eq. 2.2, the magnetic field operators become:

$$\mathscr{G}_H\{\hat{\mathbf{w}}\} = \eta_0 \text{ifft}\left(\text{fft}\left(\hat{g}^{HJ}\right) \odot \text{fft}\left(\mathbf{w}\right)\right) + \mathbb{L}^{HJ}\left(\mathbb{M}\mathbb{R}\,\text{vec}(\hat{\mathbf{W}})\right), \tag{3.22}$$

where all entries in the $L_{1,n}$ matrix operator for the magnetic field $\mathbb{L}^{HJ}$ are defined as:

$$\frac{1}{j\omega\mu_0}\left(\nabla \times J_n(kr)e^{jn\theta}\right) = \frac{1}{j\omega\mu_0}\frac{1}{r}\partial_\theta J_n(kr)e^{jn\theta}\hat{r} - \partial_r J_n(kr)e^{jn\theta}\hat{\theta} \tag{3.23}$$

$$= \frac{1}{j\omega\mu_0}\frac{jn}{r}J_n(kr)e^{jn\theta}\hat{r} - \frac{k}{2}\left(J_{n-1}(kr) - J_{n+1}(kr)\right)e^{jn\theta}\hat{\theta}, \tag{3.24}$$

and likewise the entries for the $L_{2,n}$ can be found as:

$$\frac{1}{j\omega\mu_0}\left(\nabla \times J_n(kr)e^{-jn\theta}\right) = \frac{1}{j\omega\mu_0}\frac{-jn}{r}J_n(kr)e^{-jn\theta}\hat{r} - \frac{k}{2}\left(J_{n-1}(kr) - J_{n+1}(kr)\right)e^{-jn\theta}\hat{\theta}. \tag{3.25}$$

These operators are still defined in the cylindrical coordinate system, but the eventual operators for the B_1^+ and B_1^- fields require the Cartesians coordinates. Therefore the simple conversion $\hat{r} = \cos(\theta)\hat{x} + \sin(\theta)\hat{y}$ and $\hat{\theta} = -\sin(\theta)\hat{x} + \cos(\theta)\hat{y}$ has to be applied. This allows for the magnetic field operators to have the same computational complexity as the electric field Greens operators.

This reduction of computational complexity also allows for much larger inversion regions. Both the naive method, and the decomposed methods are limited by the available storage space for the matrices. The storage space required for this problem scales with the same order as the complexity, which means that for a fixed truncation the inversion region for the decomposed matrix can be much larger. Considering a computer with 16 GB of RAM which 75% can be used (12 GB) for the operators, a square inversion region of 1118×1118 would be possible when using this low-rank method, while this region is only limited to 105×105 when using the naive implementation.

3.3. Optimization

These new operators do not have much of an impact on the of the whole optimization algorithm. The same cost functions, which penalize a mismatch between the measured and simulated field and which penalize not adhering to Maxwell's equations, will be used. Also the same optimization scheme of conjugate gradient descent will be used. The main (or only) difference introduced by these correction terms falls in defining the gradient of the cost function, which is defined using the adjoints of the Greens operators.

3.3.1. Adjoint

For this section, the naive implementation of the shielded Greens operators will be considered first, after which the complexity reductions will be applied. In the naive implementation of the Greens operators, the operation is a large matrix multiplication. The adjoint operator for matrix multiplication is well-known and is given by the Hermitian-Adjoint, which is simply the left multiplication with the Hermitian of the original matrix. Using the knowledge that the naive implementation is the super-position of the 'free-space' Greens operator and the correction term, this Hermitian adjoint operator can be defined by applying the distributive property of the Hermitian as:

$$\mathscr{G}^{\dagger}\{\hat{\mathbf{w}}\} = \mathbb{G}^{H}\hat{\mathbf{w}} = \mathbb{G}^{H}\hat{\mathbf{w}} + \mathbb{P}^{H}\hat{\mathbf{w}}, \tag{3.26}$$

which holds for both the electric as magnetic field Greens operators. Like the equivalency between applying the double Riemann sum and the method based on the convolution theorem (Sec. 2.2.1), an equivalency can be derived for applying the adjoint operator of this free-space operator. This means these adjoint operators can be split in the adjoint for the free-space part, which could be solved using the adjoint of the convolution theorem as shown in Algorithm 1, and the Hermitian adjoint using the Hermitian of the decomposed Greens operators. This results in the adjoint of the operators to be defined as:

$$\mathscr{G}^{\dagger}\{\hat{\mathbf{w}}\} = \mathscr{G}^{\dagger}\{\hat{\mathbf{w}}\} + \left(\mathbb{R}^{H}\mathbb{M}^{H}\right)\left(\mathbb{L}^{H}\hat{\mathbf{w}}\right). \tag{3.27}$$

With this definition the effects of the RF-shield present around the birdcage coil is described for the physics, and the implementation of these physics in the optimization algorithm. This improved physical model should now results in better reconstructions of the electrical properties as this chapter provided a better representation of the physical truth.

4

Quantization

The previous chapter showed the methods for reconstructing the electrical properties of tissue in a two-dimensional shielded birdcage coil, under the assumption that the fields are truly E-polarized. Testing, as will be shown in Chapter 5 and Appendix F.1, showed (mostly) good results for noiseless measurements, but showed poor performance when realistic noise was applied to the measurements.

The inversion problem, which the shielded CSI-EPT algorithm solves for, is ill-posed. In general this means that there does not exist a unique solution to the problem, and that small changes on the input can have extreme results on the output. The effects of small noise can have impact on the reconstruction, as shown by the reconstruction on realistically noisy data in Appendix F.1. Effects caused by this 'ill-posedness' can be reduced or mitigated by imposing constraints on the optimization problem, leading to a higher likelihood of converging to the correct solution, and a more robust solution with respect to noise.

This chapter will first describe the constraints which have been applied to the CSI-EPT method, based on the physical domain of certain quantities used. After this, a new method will be proposed which uses the multi-modality of the tissue parameter, which will result in the introduction of the quantization steps of the shielded CSI-EPT algorithm.

4.1. Constraints on the physical domain of tissue parameters

Physics tells us that conductivity and relative permittivity are bounded in magnitude. The conductivity is a real quantity that is strictly positive, and the relative permittivity is a quantity that is larger than or equal to 1. This *a priori* knowledge can be applied to the intermediate results produced by the reconstruction method to guarantee the reconstruction algorithm only produces results which are feasible. Not applying these constraints could result in a reconstruction which converged to values which cannot occur in nature. These *positivity constraints* [31] were previously used by applying (one of two) activation functions on the reconstructed parameters. The activation functions used there were the absolute function and the Rectified Linear Unit (ReLU) function, mapping the quantities which are physically impossible to the closest or another representative one. Since the conductivity is lower-bounded by 0, no modification to the activation function has to be applied, but this does not hold for the relative permittivity, which was lower-bounded by 1. The activation functions for the absolute and the ReLU function can be modified to $\max(|\epsilon_r|), 1)$ and $\text{ReLU}(\epsilon_r - 1) + 1$, respectively. Applying these constraints showed significant improvements in the accuracy of the reconstruction.

4.2. Constraints on the multi-modality of tissue parameters

Many researches, as summarized in [32], showed that different tissues have distinct electrical properties. The electrical properties of these tissues can even be assumed constant per tissue type within one subject, but may be varying from patient to patient. The IT'IS foundation's database [32] provides the (electrical) properties of may different tissues as the average of these many researches. Figure 4.1 shows a few of these properties for the most commonly found tissues inside a human head . Since the dataset used for testing only consists of brain models, the different tissues in the brain (gray matter, white matter, and cerebrospinal fluid (CSF)) are highlighted in these figures.

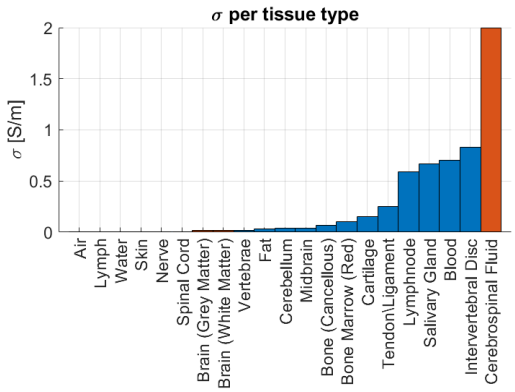

(a) Conductivity levels for different tissue types in the head

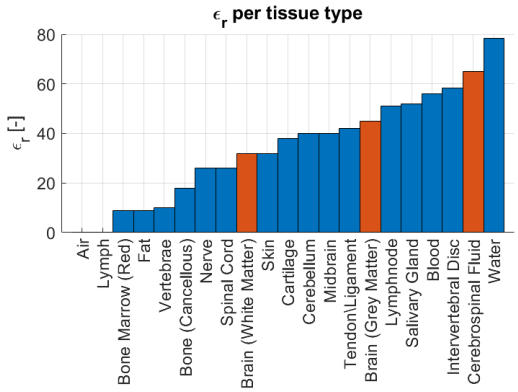

(b) Relative permittivity levels for different tissue types in the head

Figure 4.1: Tissue parameters for different tissue types in the head as given by the database of the IT'IS foundation [32]. This figure illustrates the quantized levels of the tissue parameters. The gray matter, white matter and cerebrospinal fluid are highlighted, as these are most commonly used in segmentation of brain images

The true values of the electrical properties cannot be known a priori as these are patient specific, but from this data one can assume that the tissue parameters can only take one of a few values. This means the distributions of the tissue parameters become multi-modal, with one mode corresponding to one tissue type. Of these modes however, the support (which pixels belong to this tissue type), and the exact value are unknown and must be found during the optimization process of the shielded CSI-EPT.

In the two-dimensional CSI algorithm only data from a single slice is used, which inherently means that there can only be a limited amount of tissue types present. When looking at the distribution of the tissue parameters in such a slice, this distribution becomes multi-modal, where each mode (assuming no variation for a single tissue type) is infinitesimally narrow. Since the reconstruction still allows for a continuous amount of levels for the tissue parameters, reconstructing such that these peaks are reached in the reconstruction is very unlikely, and what most probably will occur is that those peaks will become wider, and the distributions corresponding to the different tissue types will have more variance. Figure 4.2 shows the distribution of the tissue parameters after reconstruction for each of the different tissue types separately an a synthetically generated truly E-polarized data-set with realistic noise. These figures show that the distribution of the conductivity levels is still multi-modally distributed, while no structure is present in the distribution of the relative permittivity.

The goal of the quantization method now becomes to enforce this multi-modality on the intermediate results, reducing the variance for each of these modes, allowing for a more robust and more accurate reconstruction. This method might also lead to a better separation for the different modes.

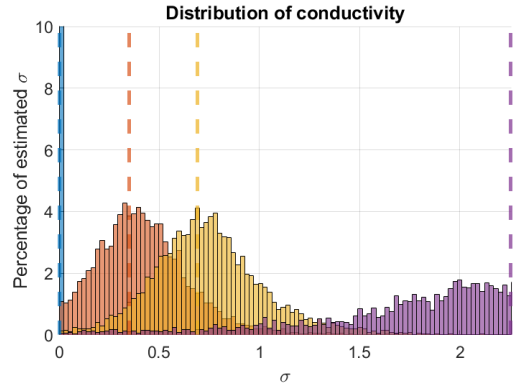

(a) Histogram of the conductivity for the different tissues

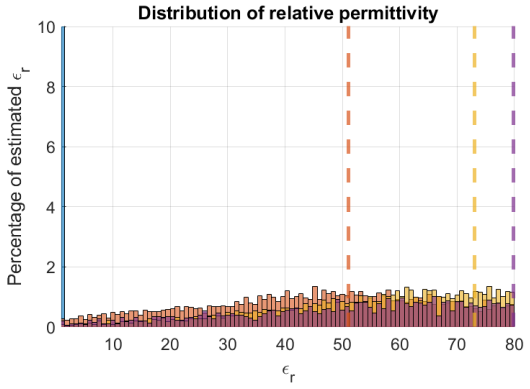

(b) Histogram of the relative permittivity for the different tissues

Figure 4.2: Histogram of the electrical properties after reconstruction on noisy E-polarized measurement data for slice 80 of subject M1. The dashed lines represent the ground truth of the value which should be reconstructed. This figure shows an increased variance for the modes of the conductivity, while the modes of the permittivity do not show any structure.

Splitting an image into several regions based on certain properties is called image segmentation. In the

medical field this is often applied to brain images, resulting in 'brain image segmentation'. Image segmentation techniques, often also called clustering techniques, can be subdivided into several categories, each with their own advantages and disadvantages. One must keep in mind that most of the techniques used in image segmentation would usually be applied only once, while in our application the clustering must be performed many times during an already computationally expensive optimization scheme. This section will describe a few of these categories and provide motivation on the usability for this application. This motivation will mainly be based on the computational complexity, noise-robustness, and the applicability to large-scale data of the different methods.

A summary of these different methods, with a few commonly used examples from literature, is shown in Tab. 4.1.

4.2.1. Hierarchical clustering

In hierarchical clustering, data clustering is achieved by finding a hierarchy of clusters. This hierarchy is based on the similarity between the certain clusters and is found in one of two methods: agglomeratively or divisely. In agglomerative clustering, each data point is considered a cluster, which will be merged together based on a minimum inter-cluster distance, in a greedy approach. This inter-cluster distance, or cluster-linkage, can be defined using many different methods[33], each with their own computational complexities. The clusters will be merged until the desired number of clusters is reached. The second method, divisive clustering, starts with all data belonging to one cluster, after which it will split the cluster based on the maximum inter-cluster linkage, until it reaches the desired amount of clusters (or another clustering condition has been satisfied).

The computational complexity of most hierarchical clustering algorithms is $\mathcal{O}(n^3)$, where n is the number of data points which in our case is the number of pixels, where the most efficient methods have a complexity of $\mathcal{O}(n^2)$. Since data points are added to the clusters in a greedy manner, these points will not be reconsidered after they have been added to a cluster, resulting in poor performance on noisy data[34]. Additionally, the methods require knowledge of the number of clusters to be found, which in the application for this work is unknown.

4.2.2. Partitional clustering

In partitional clustering all data points will be clustered such that each belongs to one (disjoint) cluster, with the exception of fuzzy clustering where each data point can have a membership grade for multiple clusters. This is most often achieved by minimizing a cost function iteratively, which is stopped either when a convergence bound is reached, or a maximum number of iteration is reached. The most famous partitional clustering method is the K-means clustering method. K-means partitions the data into K disjoint subsets, such that the total distance from the data points to their clusters' center is minimal. K-means clustering, as most clustering problems, is an NP-hard problem. The iterative optimization process for a fixed K, given by Lloyd's algorithm[35], has a computational complexity of $\mathcal{O}(nKT)$, where T is the maximum number of iterations allowed. This iterative process will converge to a local minimum, which does not necessarily coincide with the global optimum. This method, similar to the hierarchical methods, requires knowledge of the amount of clusters K. The low computational complexity of this algorithm allows for the implementation of this algorithm on more large scale data. The K-means algorithm does perform significantly worse on noisy data[34], or data infected with outlier, as these outlier may lead to the shifting of the clusters to incorrect location, significantly impacting the clustering accuracy.

4.2.3. Spectral clustering

Spectral clustering does not cluster on the data itself, but on a lower-dimensional representation of the data[36]. This is achieved by assuming all data points being nodes of a graph, and creating an adjacency or similarity matrix for this graph. This matrix will be converted to the (normalized) graph Laplacian, of which the first K eigenvectors are taken. These eigenvectors will be combined in a new matrix on which the clustering will be performed, which is done most often using the partitional clustering method of K-means.

Spectral clustering methods were shown to outperform standard partitional clustering methods, such as K-means, for noisy data and more complex cluster shapes. Where K-means works for round-, or for higher-dimensional data (hyper)spherical-shaped clusters, spectral clustering is not limited to these shapes of clusters and can be used for more arbitrarily shaped clusters. However, spectral clustering methods are computationally much more complex than standard clustering methods, due to eigenvalue decomposition, which has to be performed with a complexity of $\mathcal{O}(n^3)$, making it less viable for larger-scale data sets.

Table 4.1: Overview of several clustering methods. This overview includes few examples and shows the computational complexity, robustness w.r.t. noise, and whether or not the method is applicable for large scale datasets.

Clustering Category	Example	Performance			Remarks
		Computational complexity	Noise robustness	Applicability large scale data	
Hierarchical	HAC	$\mathcal{O}(n^3)$	Medium	No	[33] showed an improvement for better results on noisy implementations
	SLINK	$\mathcal{O}(n^2 \log n)$	Medium	Yes	
Partitional	K-means	$\mathcal{O}(nKT)$	Low	Yes	
	Improved K-Means [37]	$\mathcal{O}(nKT)$	Medium	Yes	Filtering data before applying K-means
Spectral	[36]	$\mathcal{O}(n^3)$	High	No	Limited by EVD of similarity matrix

4.3. Quantization step using K-means

The hierarchical and spectral clustering methods are not feasible in this application due to their higher computational complexities. This implicitly means that the interim clustering must be built upon a partitional clustering algorithm, which in general have a lower computational complexity. This work will consider the K-means clustering method. This algorithm is one of the most widely used clustering algorithms, even though it has a poor robustness w.r.t. noise. To improve the performance w.r.t. noise, the improved K-means clustering[37] will be considered, which performs low pass filtering prior to the clustering.

K-means clustering separates a set $[x_1, x_2, ..., x_N]$ of N samples into K subsets $\mathbf{C} = [C_1, C_2, ..., C_K]$ (or clusters) such that the distance of the points belonging to the subsets is minimized. This is achieved by minimizing a cost function such that the sum of Euclidian distances for each point to the center of its cluster is minimal. This cost function is defined as:

$$J = \sum_{k=1}^{K} \sum_{x \in C_k} ||x - M_k||^2 , \tag{4.1}$$

where M_k denotes the center of cluster C_k. The centers of these clusters can now be found iteratively by minimizing this cost function until either a minimum is reached or a maximum amount of iteration is reached. The full K-means algorithm, given by Lloyd's algorithm[35], is described in Algorithm 3.

Algorithm 3 K-means

1: Random initialization of the cluster centers M_k
2: **for** $i = 1, 2, \ldots$ **do**
3: Assign all sample points x_n to the nearest cluster
4: Recalculate the center of each cluster: $M_k = \frac{1}{N_k} \sum_{x \in C_k} x$
5: Calculate cost function: $J^{[i]} = \sum_{k=1}^{K} \sum_{x \in C_k} ||x - M_k||^2$
6: **if** $J^{[i]} \geq J^{[i-1]}$ or $i \geq I_{\max}$ **then**
7: Stop
8: **end if**
9: **end for**

The clustering method will be applied on the contrast function, to keep both the information of the conductivity and the relative permittivity. The K-means clustering algorithm will find this Euclidian distance, by splitting the complex contrast function into a vector, separating the real and imaginary parts. This means $\chi \in \mathbb{C}$ will be represented as $\chi = [\Re(\chi), \Im(\chi)]^T \in \mathbb{R}^2$, which is equivalent to splitting one complex feature into two real features. Priory it was already stated that the real part of the contrast function is much more sensitive

to noise, and that much of the information about the relative permittivity is lost there. This therefore shows that one of these features for the K-means, would mainly introduce errors.

Instead of representing the complex number as its real and imaginary part, the contrast function could also be separated into its polar coordinates $\chi = [|\chi|, \angle\chi]^T \in \mathbb{R}^2$, again splitting the one complex feature into two real features. These features also occupy distinct levels for different tissue types. When the clustering is performed on this representation, the calculation of the Euclidian distance has a different interpretation than for using the Cartesian representation. Testing showed better performance for clustering on the polar representation of the contrast source. This is most probably caused due to the smaller magnitude of the real part of the contrast function (corresponding to the permittivity), which is affected more by noise as the noise has an equal magnitude for the real and imaginary part, thus a relatively larger effect on the permittivity.

4.3.1. Mapping using stacked sigmoid

When applying the clustering of K-means, all parameters will usually be mapped using a staircase-type function, where the height and width of the steps are determined by the location of the clusters and the spacing between clusters. This then becomes very similar to a multi-level thresholding problem[38]. Such a function will force all parameters to the cluster centers, resulting in chopping of the original signal. This effect of this chopping might becomes larger than any step the CSI algorithm can take in one iteration, leading to the CSI being stuck in the local minimum introduced by this clustering. Due to the computational load, and the (very likely) chance of being stuck in a local minimum the clustering is only performed once every N_C iteration, which is usually chosen such that the clustering is performed once every 20 or 50 iterations.

This stair-case style function is a piece-wise constant function mapping the continuous spanning input parameters to the quantized levels found by the k-means. This mapping function inherently has jumps in its gradient due to the jumps between the different levels. Values near the edges of the different levels will be mapped towards the center of these cluster, which means that wrong classifications near cluster boundaries will have extreme consequences.

To alleviate these issue introduced by the coarse mapping of the staircase-function, a smoother continuously differentiable function can be found which still promotes these quantized levels. This function is the stacked sigmoid, which is constructed by fitting a sigmoid function between each of the clusters centers. The stacked sigmoid can be constructed as:

$$\chi_{\text{out}} = M_1 + \sum_{k=2}^{K} (M_k - M_{k-1}) \text{sigmoid}\left(\alpha\left(\chi_{\text{in}} - \frac{M_k + M_{k-1}}{2}\right)\right), \tag{4.2}$$

where α denotes the steepness of the sigmoid function. Figure 4.3 shows such a sigmoid function for $\alpha = 0.5$, the staircase function it approximates, and their gradients.

This mapping function could now be added into the optimization problem of χ, where χ becomes a function over another parameter χ_{in}, such that the optimization can be performed for χ_{in}. Reconstructing the contrast function from the contrast source would require another iterative process, as the minimum least squares solution does not exist for this function. This thesis only use the mapping of this function, during the quantization step not incorporating it in the gradients for the sake of a lower computational complexity.

4.3.2. Low pass filtering

Another major drawbacks of K-means clustering, besides its sensitivity to the chosen amount of clusters K, is its susceptibility to noise. This means that clustering on the intermediate contrast function will be hard, since the noise can cause for a wrong clustering, further increasing the reconstruction error. Therefore, steps must be taken to reduce or remove this noise.

Most of the image of the resides in the lower frequency of the K-space representation of the image. Assuming that the noise is somewhat frequency independent, much of the noise can be removed by only retaining these lower frequencies, while limiting the contributions of the higher frequencies. Filtering for these higher frequencies has been performed by first applying a averaging filter to the image[37]. This averaging filter creates a new image by averaging the pixel values of a small neighborhood of 3×3, 5×5, or 7×7 around the pixel.

Instead of filtering in the imaging domain, the filtering could also be performed in K-space. Filtering for these lower frequencies can be now achieved by placing a two-dimensional Gaussian bell over the K-space representation of the image, gradually lowering the contributions of the higher frequencies. This filtering does not only affect high frequency components of the noise, but also the high frequency components of the

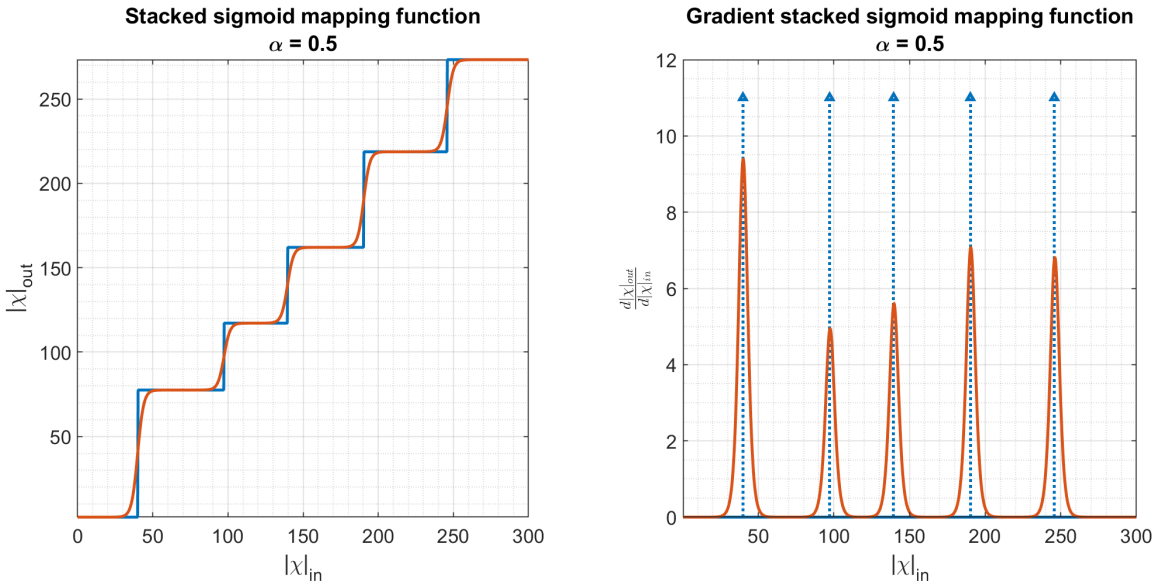

(a) Stacked sigmoid

(b) Gradient of stacked sigmoid

Figure 4.3: Example of a stacked sigmoid function where the cluster centers are defined as $\mathbf{M} = [0, 77, 117, 162, 218, 273]$, and the steepness parameter $\alpha = 0.5$. The blue lines represent the staircase function which is approximated by the stacked sigmoid, which for the gradient becomes a collection of delta spikes.-

original signal. These high frequency components represent the fast changes in parameters, which should only occur at tissue boundaries. This manipulation of the K-space inherently causes for a worse performance at the tissue boundaries and removes smaller details from the image, but allows for a much more robust performance of the clustering algorithm.

The whole quantization process which is performed once every N_c iteration is summarized in Algorithm 4.

Algorithm 4 Quantization step

Apply low pass filter on contrast function

$\chi' = \text{LPF}(\chi_{in})$

Perform K-Means clustering on χ'

$\mathbf{C}, \mathbf{M} \leftarrow \text{KMeans}(\chi')$

Create and apply stacked sigmoid function

$$\chi_{out} = M_1 + \sum_{k=2}^{K} (M_k - M_{k-1}) \cdot \text{sigmoid}\left(\alpha\left(\chi_{\text{in}} - \frac{M_k + M_{k-1}}{2}\right)\right)$$

5

Simulation

The previous chapters described the problem, and mainly the methods on how to solve the problem. This chapter will show and discuss the results for applying these methods in simulation. These simulations serve for assessing the performance on a truly E-polarized simulation setup, assess its performance on different levels of noise, and finally determine how well the shielded CSI-EPT reconstruction algorithm performs on realistic three-dimensional (where the waves are no longer fully E-polarized). This performance assessment shows the accuracy and robustness of the shielded CSI-EPT algorithm on truly E-polarized data, and can give a good insight for its performance on more realistic data, such that it can be used in pseudo 3D form as a good initialization for a three-dimensional EPT method.

The dataset used for these simulation is the ADEPT[39] dataset, consisting of 120 different brain models, of which 84 are healthy and 36 contain tumors. For each of these models the conductivity and relative permittivity levels are known, as well as the relevant three-dimensional electromagnetic fields for MR-EPT (the magnitude of B_1^+ and the corresponding transceive phase $\phi^{\pm}$). These fields are calculated using the full-wave solver Sim4Life [40]. The measurements for the E-polarized simulation setups will be generated using the physics described in Chapters 2 and 3.

This chapter will start with the description and comparison of performance metrics used in literature, and describing which performance metric will be used for the assessment. These metrics will subsequently be used to assess the performance on a full E-polarized simulation setup. For this also the performance with respect to noise levels will be determined. Finally, the performance on the full-wave solved three-dimensional fields will be assessed. The results shown in this chapter are based on the reconstruction of subject M1, from the ADEPT dataset, and for the metrics also the distribution of the results for all other subjects is shown. The conductivity and permittivity of transversal slice 80 of subject M1 are shown in Fig. 5.1. The conductivit and permittivity values of the different tissues in this (and all other slices for M1) are found in Tab. 5.1.

5.1. Metrics

As stated in the introduction of this thesis, the goal of the shielded CSI-EPT method can be split into two parts. The first is purely based on accuracy, since high reconstruction accuracy means that the absolute values of the electrical properties are found well. This performance can be tested well using several numerical metrics, of which a few will be described and used in this chapter. The second goal is to produce an image which can be interpreted well, meaning that the absolute values of the electrical properties might be incorrect, but the overall shape (or support) of the image is found correctly. This difference results in the analysis of the results both in a quantitative and qualitative manner.

This section will describe the different analyses that will be performed for all simulations, including a small discussion regarding the performance metrics used. For the performance based on the different noise

Table 5.1: Ground truth tissue parameters for the different tissues of subject M1

Tissue type	Air	White matter	Gray matter	Cerebro Spinal Fluid (CSF)
Conductivity [S/m]	0	0.35	0.69	2.26
Relative permittivity [-]	1	51	73	80

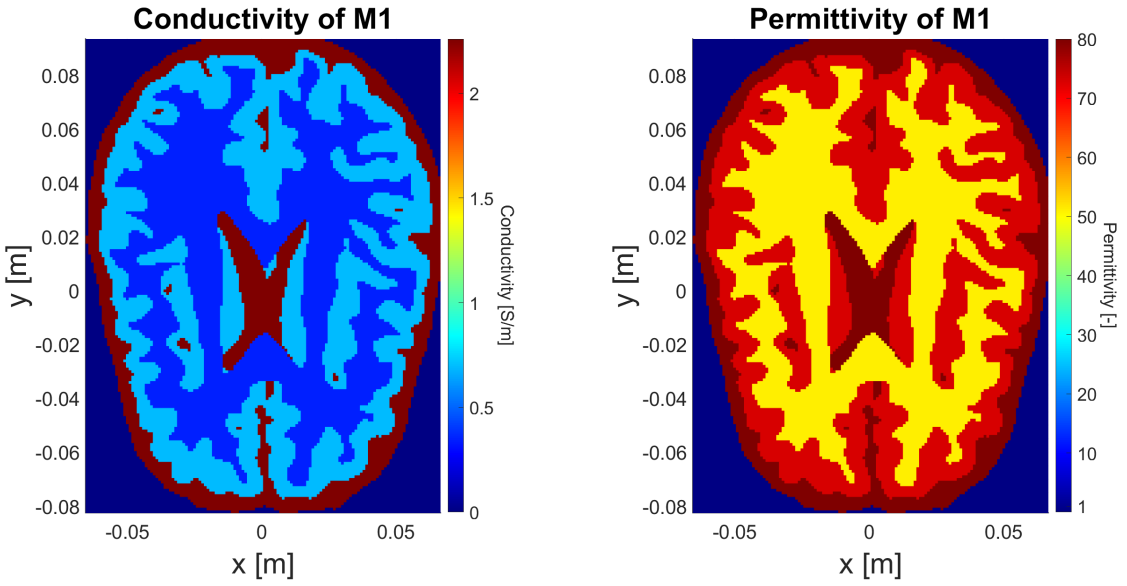

(a) Ground truth of the conductivity

(b) Ground truth of the relative permittivity

Figure 5.1: Ground truth of slice 80 for subject M1 of ADEPT. These parameters are to be reconstructed throughout all simulation in this chapter.

levels, these will not be used directly. During the discussion of the results, the results for the quantitative metrics will be shown for all subjects from the ADEPT dataset, while the qualitative metrics will only be discussed for subject M1.

5.1.1. Cost function

The first analysis which will be performed is on the progression of the cost function. During the calculation of the cost function, no knowledge of the ground truth is available, which is why it will not be called a performance metric directly. The cost function (by construction) gives insight in how well the reconstruction matches the data, and how well the reconstruction adheres to Maxwell's equation. While combined in one value, this could give insight into how well the algorithm itself thinks the solution is correct and accurate.

Given that the problem is ill-posed, there is no guarantee that the algorithm will converge. This analysis will also show whether or not the cost function will converge, or whether it will diverge from a minimum.

5.1.2. Masked MSE

The first true performance metric used is the masked Mean Square Error (MSE). The MSE is the average of the absolute squared error of the reconstructed parameter and the ground truth, for both the conductivity and relative permittivity separately. The standard formula for calculating the MSE is:

$$\mathrm{MSE}(\sigma) = \frac{1}{MN} \sum_{m=1}^{M} \sum_{n=1}^{N} |\hat{\sigma}_{mn} - \sigma_{mn}|^2 , \tag{5.1}$$

where $\hat{\sigma}_{mn}$ denotes the estimated value of the conductivity at pixel (m,n), and σ_{mn} is the ground truth at that same location. The same calculation would be done for the MSE of the relative permittivity.

This standard form of the MSE would average over all pixels in the inversion region, also the pixels for which no tissue is present. During data acquisition, the field can only be measured at the locations where tissue is present. This inherently provides a mask showing all the location where tissue can be, and showing the locations where only air is present. This information is available prior to the reconstruction, and is also used during the reconstruction. Averaging over all pixels, including the 'air-filled' pixels, will give a skewed result for the accuracy of the reconstruction. To correct for this the Masked MSE will be taken, in which only the pixels containing tissue will be used for calculating the MSE. The masked MSE is calculated as:

$$\mathrm{MSE}(\sigma) = \frac{1}{|\mathbb{D}^{\mathrm{obj}}|} \sum\sum_{(m,n)\in\mathbb{D}^{\mathrm{obj}}} |\hat{\sigma}_{mn} - \sigma_{mn}|^2 , \tag{5.2}$$

where the domain $\mathbb{D}^{obj}$ contains all pixels with tissue. Since the pixels containing air will automatically be estimated as such, the only difference between the masked and unmasked MSE is the fraction in front of the sums. The conversion from masked to unmasked is therefore rather straightforward; this conversion will be performed when comparing to results found in literature as there the unmasked variant is used most often.

The values which the conductivity can take (0 - 2.5 S/m) is generally much smaller than the values the relative permittivity can take (1 - 90). Comparing the results of the MSEs for the conductivity and the relative permittivity is therefore not fair, given that these have a completely different unit. Literature often only shows the MSE for these separately, and does not compare them to one other. This work will also show the MSE for the two quantities in the same 'unit'. Since the conductivity is often the one which is reconstructed the best, the unit of the permittivity will be corrected for by multiplying it with $\epsilon_0\omega$, which is the same multiplication used in retrieving the conductivity from the contrast.

5.1.3. Histogram inspection

The third metric used is to see how well the different tissues are being reconstructed qualitatively. This is done by looking at the distributions of the reconstructed pixels for each of the tissues. As stated in Chap. 4, the tissues should be distributed multi-modally, meaning that each of the tissues should contain only one mode. Instead of plotting the distribution of all pixels, the data is first divided into the different tissues using the ground truth, and of those separate subsets the histograms are plotted. This will give more insight on how the different tissues are reconstructed, whether lower- or higher-valued tissues perform better for reconstruction. This also allows for showing the overlap of these modes after reconstruction, giving a good indication whether the tissues can still be distinguished from one other.

5.1.4. Visual inspection

As a final assessment for the performance, the actual reconstructed image will be analyzed. This is also part of the qualitative analysis. This analysis can show more about the shape, or support, of the reconstruction. This assessment is also used to show whether or not the different regions can be recognized, whether small irregularities in the ground truths' electrical properties can be reconstructed accurately, and show potential errors which might be introduced by the reconstruction algorithm.

5.2. Reconstruction on noiseless 2D data

The first simulation assesses the performance of the shielded CSI-EPT algorithm, as described by Chapters 2 and 3, when performed on a noiseless truly E-polarized synthetic dataset. The purpose of this simulation is to show the rate at which the shielded CSI-EPT algorithm converges to-, and how accurately it can reconstruct the correct solution, when applied to idealistic measurements.

The synthetic data used for the E-polarized simulation setup are generated by solving the forward problem using the Greens operators of 3 knowing the ground truth of the contrast function in all locations. For the simulations the incident fields are calculated using a unitary amplitude for each rung ($a^n = 1$) in Eq.3.10 and its magnetic counterpart, which are subsequently used to find the total electric field using the known $\hat{\chi}$:

$$\hat{\mathbf{E}} = \arg\min_{\hat{\mathbf{E}}} \left|\left|\hat{\mathbf{E}} - \mathscr{G}_E\{\chi\hat{\mathbf{E}}\} - \hat{\mathbf{E}}^{\text{inc}}\right|\right|^2, \tag{5.3}$$

which is solved using a Generalized Minimal Residual (GMRes) method. The GMRes method in this work is allowed at most 100 iterations, and has a stopping condition when the supplied cost function reaches a value below 10^{-9}. This total field can now be used in the magnetic field Greens operators to calculate the synthetic measurements of the B_1^+ field (with the transceive phase).

For this ideal measurement the performance of the shielded CSI-EPT will be discussed. The shielded CSI-EPT method has a maximum number of iterations of 2000, and has a stopping criterion when the cost function becomes smaller than 10^{-6}.

Cost function

Figure 5.2 shows the progression of the cost function w.r.t. the iteration number; Fig. 5.2a shows this for subject M1, and Fig. 5.2b shows this as the distribution for all other subjects.

The first thing shown in Fig.5.2a is that the cost function reaches a low value of approximately 10^{-5}. This means that the reconstruction algorithm has found a solution for which the generated fields correspond extremely well with the measured data, while adhering to Maxwell's equation (as is the definition of the cost function). This is expected as the incident fields of the measured data and the ones supplied to the algorithm are equal, and the same operators are used to calculate the scattered fields. When further analyzing the cost functions definition, one can show that the data part of the cost function is equivalent to the (normalized) MSE between the measured and reconstructed B_1^+-fields. A low value of this cost function thus inherently means that the reconstructed fields are represented well.

While not necessarily shown in this work, the cost function in CSI-EPT is not guaranteed to converge. In the standard CSI-EPT algorithm, as described by just Chapter 2, the cost function is not necessarily a always descending function w.r.t. the iteration number. This is shown in [31]. The progression shown in that work tend to 'explode' after a few hundred iteration. This exploding behavior caused by the ill-posed nature of the CSI-EPT problem is not present in the shielded method presented in this thesis. This 'proper convergence' is not only present for subject $M1$, but also when considering the progression for all other subjects as shown

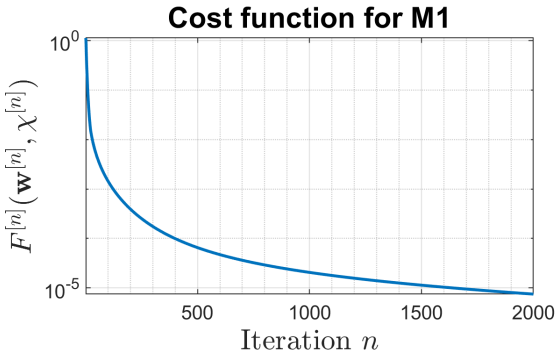

(a) Progression of the cost function for subject M1

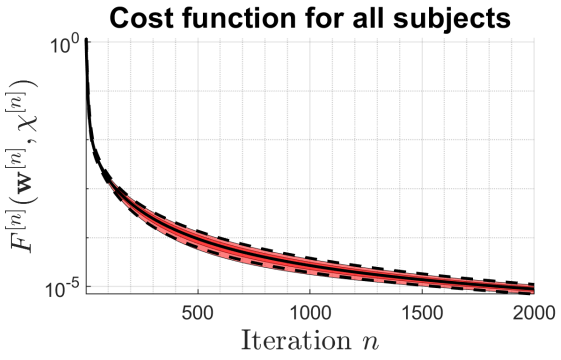

(b) Distribution of the cost function for all subjects. The black line shows the mean of all cost functions, the red regions show the area span by once or twice the standard deviation, while the dashed lines represent the maximum and the minimum of all cost functions

Figure 5.2: Progression of the cost function as a function of the iteration number for the noiseless 2D, truly E-polarized simulation setup

in Fig. 5.2b. This figure shows that all cost functions are always descending, and all reaching a minimum of approximately 10^{-5}, after 2000 iterations.

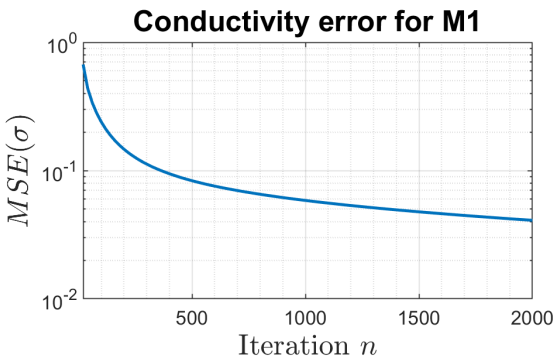

(a) Progression of the reconstruction error for the conductivity of subject M1

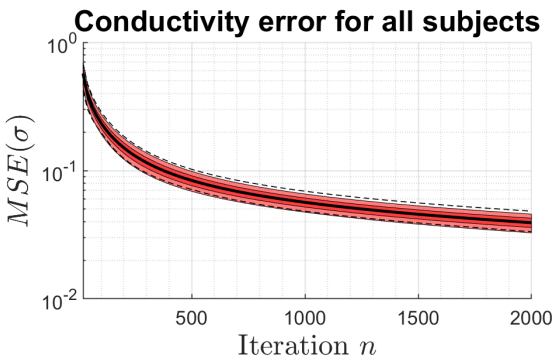

(b) Distribution of the reconstruction error for the conductivity for all subjects. The black line shows the mean, the red regions show the area span by once or twice the standard deviation, while the dashed lines represent the maximum and the minimum.

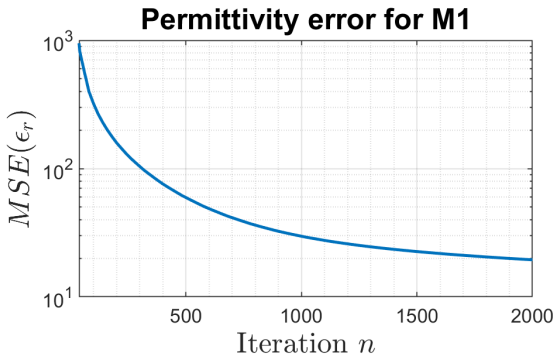

(c) Progression of the reconstruction error for the relative permittivity of subject M1

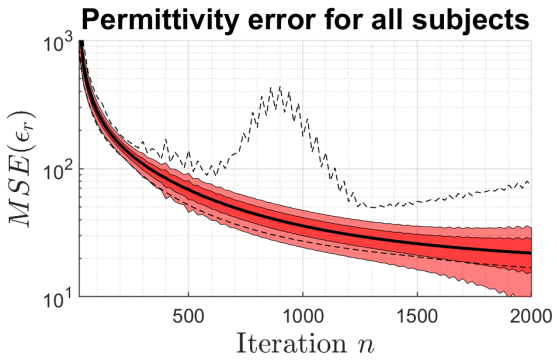

(d) Distribution of the reconstruction error for the relative permittivity for all subjects. The black line shows the mean, the red regions show the area span by once or twice the standard deviation, while the dashed lines represent the maximum and the minimum.

Figure 5.3: Reconstruction errors for the electrical properties for the noiseless 2D, truly E-polarized simulation setup. The dashed lines denote the ground truth values of the electrical properties

Reconstruction error

Figure 5.3 shows the reconstruction errors measured using the MSE for the conductivity and relative permittivity; Figs. 5.3a and 5.3c shows these for subject M1, while Figs. 5.3b and 5.3d show the distributions of these for all subjects.

The reconstruction error for the conductivity of subject M1, as shown in Fig. 5.3a, shows that the conductivity converges to a good solution, whereas the MSE reaches a value of approximately $4 \cdot 10^{-2}$ after 2000 iteration of the shielded CSI-EPT algorithm. This means that conductivity is estimated correctly with an average deviation of approximately 0.2 S/m. This accuracy is approximately consistent for all subjects, where the worst case, which reaches an MSE of $5 \cdot 10^{-2}$, deviates on average 0.22 S/m.

For the relative permittivity of subject M1, this convergence is also observed, where the MSE of the relative permittivity reaches a value of approximately 30 after 2000 iterations, which results in an average deviation of approximately 5.5. This error is significantly higher than the error for the conductivity due to the aforementioned mismatch in unit. This large difference in reconstruction accuracy is mainly caused by the 'conduction part' of the contrast function, or the conduction current in the contrast source, being dominant over the part corresponding to the relative permittivity in the contrast function, or the displacement current in the contrast source. If field strength of the background field $\hat{B}_0$ increases (e.g. in a 7 or 14 Tesla MR-scanner), the Larmor frequency ω will also increase, shifting the dominance from the conduction current more towards the displacement current, reaching a higher accuracy for the relative permittivity. The difference in unit between the conductivity and permittivity also plays a role in the difference in the MSE between the two; applying the correction however would result in the MSE for the relative permittivity to become approximately 10^{-3}.

This value is significantly smaller than the reconstruction error of the conductivity, while (as will be shown in the following subsections) the permittivity reconstruction is significantly worse. This is again caused by the mismatch in amplitude between the two quantities.

In the distribution of the reconstruction errors of the relative permittivity, one outlier is present for which the full progression is significantly higher than all other progressions. That subject (M69) is also omitted from the calculation of the mean, and standard deviation for the plot, as that would give a skewed representation of the distributions. This outlier shows that while the reconstruction algorithm converges to the right solution for most of the subjects, this is not guaranteed, considering this is still applied to an ideal noiseless dataset. This outlier is only visible in the reconstruction error of the relative permittivity; the reconstruction error for the conductivity and the cost function do not show this outlier.

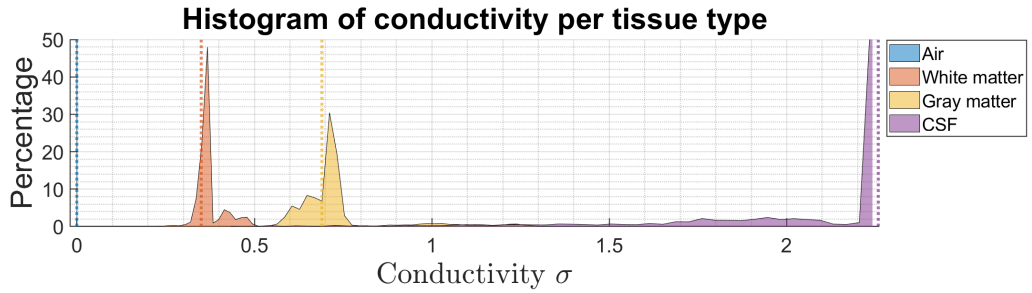

(a) Histograms for the reconstructed conductivity of subject M1

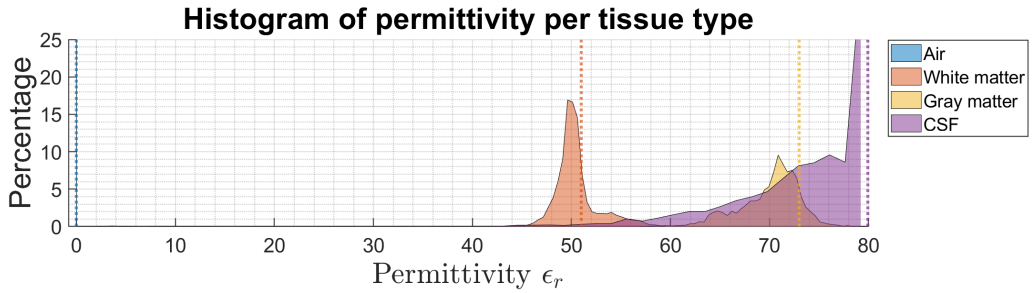

(b) Histograms for the reconstructed relative permittivity of subject M1

Figure 5.4: Histograms of the reconstructed electrical properties per tissue after 2000 iterations for the noiseless 2D, truly E-polarized simulation setup

Histogram inspection

Figure 5.4 shows the distributions of the tissue parameters for the different tissue by means of the histograms plots.

For the conductivity, as shown in Fig. 5.4a, the different modes can easily be recognized, as these are completely disjoint, meaning completely non-overlapping. This allows for an easy distinguishing of the different tissues. All three modes (for the white-, gray matter, and CSF) are located at the right value, having small variances. These variances are mostly a result from the averaging effect near tissue boundaries, shown by only a right tail for the white matter, mainly a left tail for the gray matter, and the long left tail for the CSF.

For the relative permittivity, the distributions of the tissue parameters, as shown in Fig. 5.4b, show a slightly worse result. While the modes for the different tissues are located approximately correctly, their variance is much larger than shown for the conductivity. This causes the different modes, in contrary to the conductivity, to no longer be disjoint. Especially the large left-sided tail of the CSF overlaps (fully) with the mode of the gray matter poses an issue, resulting in an indistinguishability between these two tissues. While not directly shown in these plots, this is mainly caused by an overestimation of the conductivity values near the 'air-CSF' boundary, resulting in an underestimate of the permittivity values.

These histograms primarily show that the (dominating) conductivity can be estimated much more accurately than the relative permittivity. While the relative permittivity reconstruction is less accurate, the values are still reconstructed in (mostly) the correct mode.

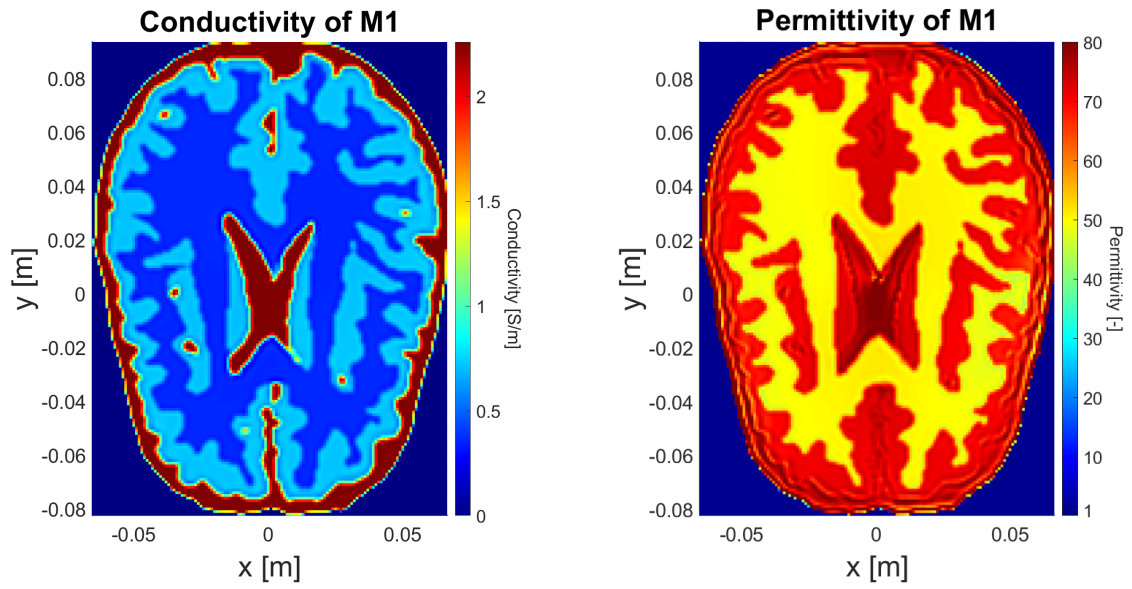

(a) Reconstructed conductivity of subject M1

(b) Reconstructed relative permittivity of subject M1

Figure 5.5: Reconstructed electrical properties after 2000 iterations for the noiseless 2D, truly E-polarized simulation setup

Visual inspection

Figure 5.5 shows the images of the reconstructed conductivity and relative permittivity of subject M1 in Fig. 5.5a and Fig. 5.5b, respectively.

The conductivity reconstruction shows a good reconstruction of the conductivity values. The support of the different tissues is reconstructed well, and even the smaller features of the CSF are found. These smaller features are enlarged due to the averaging around the tissue boundaries making them appear larger than they actually are. The most notable difference between the reconstruction and the ground truth is this effect of averaging happening at tissue boundaries due to the smoothness of the electromagnetic fields. While the amplitude of the electric field at the origin vanishes, the shielded CSI-EPT algorithm is still capable of accurately reconstructing the tissue parameters there.

As stated before, the permittivity reconstruction was less accurate than the conductivity reconstruction. This is also shown qualitatively in Fig. 5.5b. While the gray and white matter regions can be found well, and their values are reconstructed well, this is not true for the CSF. As discussed in the histogram analysis, the CSF is indistinguishable from gray matter in many places; this occurs mainly for the CSF surrounding the brain where permittivity values are severely underestimated. This reconstruction does show some effect of the electric field vanishing at the origin, due to a small gradient of the permittivity values occurring there.

Conclusion

This section showed the performance of the shielded CSI-EPT (without quantization) on ideal noiseless truly E-polarized synthetic data. This section showed that the shielded CSI-ET converged to approximately the right conductivity, while this is not guaranteed for the relative permittivity. The conductivity reconstruction is in general more accurate, shown by the lower variance in the different modes of the histograms. This is most probably caused by the dominance of the conductivity term (and consequently the conduction current) over the permittivity term in the contrast function at 3T. Finally, the smoothness of the fields causes averaging happening at tissue boundaries in both the conductivity and permittivity reconstruction, leading to a lower reconstruction accuracy at these boundaries.

The shielded CSI-EPT operators analytically described the electric and magnetic field for E-polarized waves in the PEC enclosed cylindrical shield. The methods described in Chapter 2 also solve for this situation using a few extra approximations. Appendix G will compare the standard CSI-EPT method to the shielded CSI-EPT method, showing the effects these assumptions have on the reconstruction, and showing the increase in reconstruction accuracy when correctly accounting for the shielding.

5.3. Analysis to different noise levels

The first simulation had a purpose of assessing the performance using ideal noiseless truly E-polarized measurements. The simulation described in this section will assess the performance based on different noise levels, determining how robust the shielded CSI-EPT algorithm is to noise. This section will also compare the standard shielded CSI-EPT method with the method that includes the quantization steps of Chapter 4. The performance metric in this chapter will be the final value of cost function after 2000 iteration for different levels of noise, as well as the reconstruction errors for these reconstructions at this final iteration (reconstruction images for these different noise levels can be found in Appendix F.1). During testing, it was observed that the cost function always converged to a minimum, thus prior stopping of the iterative process was not necessary.

In B1-mapping the amplitude and phase are mapped separately, and thus the noise is also added independently for the amplitude and the phase of the measured data. A realistic noise level for a 3T machine is a signal which has a SNR of 54 ($\approx$ 35dB) [12] (the performance of the algorithm at this noise level will be discussed in Sec. 5.4). The measured signal is constructed by measuring the signal power of the original $\hat{\mathbf{B}}_1^+$, and adding the respective noise to the amplitude and phase. The measured data which will be used as input data is then calculated as:

$$S = |\hat{B}_1^+ + \mathcal{N}_{B_1^+}| e^{j(\phi^\pm + \mathcal{N}_\phi)}, \tag{5.4}$$

where B_1^+ and $\phi^\pm$ are the magnitude and (transceive phase) of the measured signal calculated in section 5.2, and $\mathcal{N}_{B_1^+}$ and $\mathcal{N}_\phi$ are the noise sources, sampled from a scaled white Gaussian distribution to reach the desired SNR.

Cost function

Figure 5.6 shows the final values of the cost function for different noise levels; Fig. 5.6a shows this for subject M1, while Fig. 5.6b shows the distribution for all subjects.

For measurements with extremely high noise levels (low SNRs) the cost function of the standard shielded CSI-EPT (without quantization) is not able to converge to a low value. In this situation, the algorithm is unable to model a field which accurately corresponds to measured fields. The rapid changing magnetic fields cannot be constructed due to the inherent smoothness of the electric and magnetic fields, which means a low value for the data residual cannot be reached. When the noise decreases (and consequently the SNR increases), the reconstruction algorithm becomes much better at estimating these fields.

A similar trend can be observed for the method including the quantization steps, except that these methods converge to a cost function which is significantly higher. Especially when less noise is present, the quantized method has a significantly higher cost function to which it converges. This is caused by the 'chopping' of the quantization step, which is not included in the properly defined nonlinear conjugate gradient descent. Every 50$^{\text{th}}$ iteration, the quantization step maps the contrast function to the clusters, increasing the cost function significantly, as this was not accounted for by the gradient descent algorithm. Once the algorithm has almost converged, this jump in the cost function becomes larger than the iterative algorithm can descend in

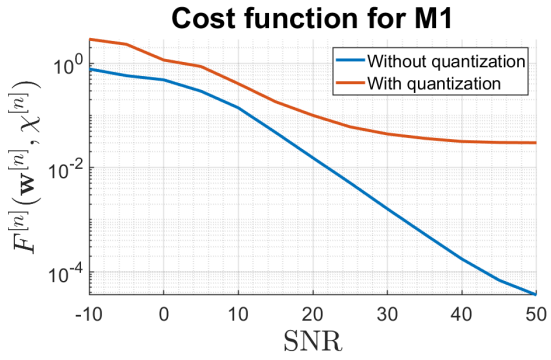

(a) Cost function values for subject M1

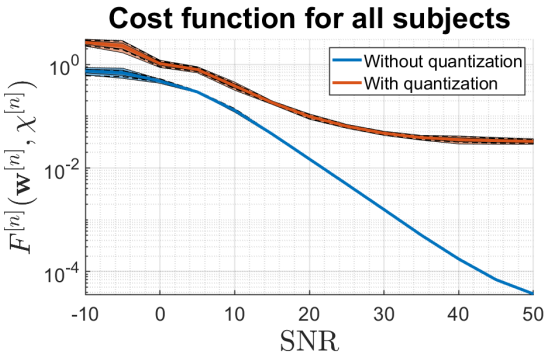

(b) Distribution of the cost function for all subjects. The black line shows the mean and the shaded regions show the area span by once or twice the standard deviation

Figure 5.6: Cost function values at the last iteration of the shielded CSI-EPT method for different noise levels

50 iterations, leading to this increased cost function. Given that the amount of iterations (2000) is a multiple of the quantization interval (50), the final cost function displayed in Fig. 5.6 is at the jumps, which is usually 10 times higher than the lowest value.

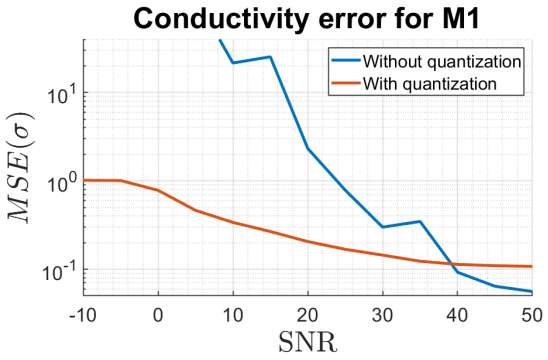

(a) Progression of the reconstruction error for the conductivity of subject M1

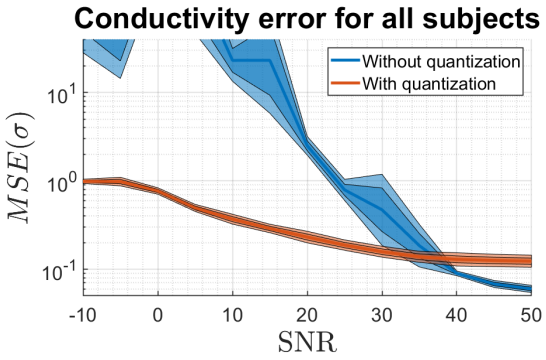

(b) Distribution of the reconstruction error for the conductivity for all subjects. The black line shows the mean and the shaded regions show the area span by once or twice the standard deviation

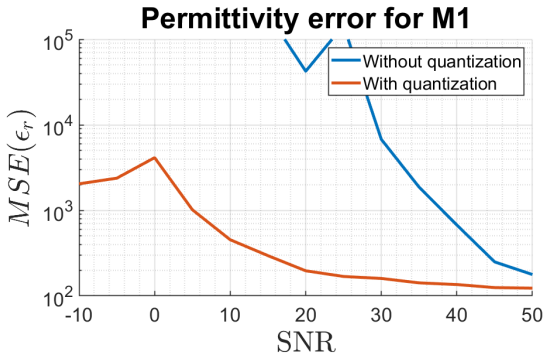

(c) Progression of the reconstruction error for the relative permittivity of subject M1

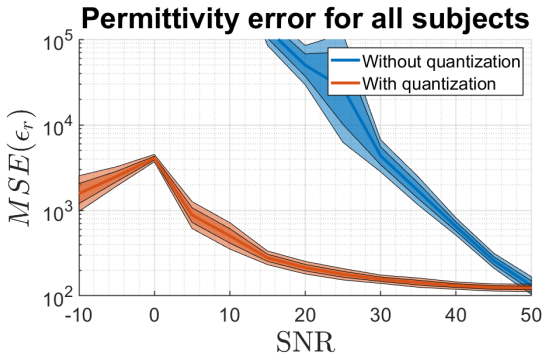

(d) Distribution of the reconstruction error for the relative permittivity for all subjects. The black line shows the mean and the shaded regions show the area span by once or twice the standard deviation

Figure 5.7: Reconstruction errors for the electrical properties for the noiseless 2D, truly E-polarized simulation setup. The dashed lines denote the ground truth values of the electrical properties

Reconstruction error

Figure 5.7 shows the reconstruction errors measured using the MSE for different noise levels after 2000 iteration of the (quantized) shielded CSI-EPT; Figs. 5.7a and 5.7b show the errors for the conductivity for subject M1 and the distribution for all errors, while Figs. 5.7c and 5.7d show these for the permittivity.

When considering the performance on the conductivity reconstruction, the method with quantization performs better for lower SNRs than the method without the quantization step. This is predominantly caused by the ceiling introduced by the clustering method, limiting values which the conductivity can take. This is shown by the plateau at the lower SNRs in Figs. 5.7a and 5.7b. For higher SNRs, the method without quantization will eventually surpass the method with quantization. This crossover point is located at an SNR of roughly 40dB. The low-pass filtering required for the clustering algorithm to work, does not only remove high frequency noise, but also removes details from the image. This loss of detail will cause some pixels to be misclassified, and thus will be given an incorrect value, which subsequently increases the reconstruction error. This means that when the noise becomes sufficiently small, the quantization step is not required for conductivity reconstruction.

For the permittivity reconstruction, however, the performance is in general higher with the quantization step. As stated before, due to the dominance of the conduction current over the displacement current in 3T MR-scanners, the conductivity can be estimated much more accurately than the permittivity. The quantization method couples the conductivity and permittivity, since the clustering is performed on the contrast function. Small variation in the real part of the contrast function, can have large effects on the reconstructed permittivity due to its relative small size, in comparison to the imaginary part. The magnitude component

of the features used for clustering is mostly dominated by the imaginary part of the contrast source (corresponding with the conductivity), which causes the clustering to be focused mostly on these conductivities. Due to the better reconstruction performance for the conductivity, the clustering becomes rather accurate, which means that the support for the permittivity is known, allowing for a better estimation. For higher field strengths, the more dominant part of the cost function, and consequently the quantity which can be estimated more accurately, will shift to the permittivity.

Conclusion

This simulation showed the robustness with respect to noise of the shielded CSI-EPT algorithm with and without the quantization steps. Without quantization, the performance of the shielded CSI-EPT algorithm quickly degrades once the noise increases slightly. While the quantization removes details from the reconstruction, the algorithm becomes much more robust with respect to noise. Due to the coupling of the conductivity and permittivity in the clustering method, the reconstruction accuracy of the permittivity is significantly increased even for the almost noiseless situations.

5.4. Reconstruction on noisy 2D data

The data acquisition performed by the MR-scanner is not perfect, which results in noise added to the measured signal. During data acquisition the amplitude and phase are measured independently, leading to two independent noise sources: one for the amplitude, and one for the phase. A realistic noise level for a 3T MR-scanner reaches a signal with an SNR of 35dB (factor 54) [12]. This section will show the reconstruction results having a SNR of 35dB using the noise generation described in Sec. 5.3. The results shown in this section are of a reconstruction after 2000 iterations of the shielded CSI-EPT reconstruction algorithm with the quantization step of Chapter 4.

Appendix F.1 shows the results of the shielded CSI-EPT method without quantization for a signal with this noise level. The ill-posed nature of the problem caused for a poor performance of this, showing the poor noise robustness of the shielded CSI-EPT algorithm. This was the motivation for introducing the quantization steps in the iterative reconstruction process. This chapter will show the results of the shielded CSI-EPT algorithm with the inclusion of the quantization steps described in Chapter 4.

Cost function

Figure 5.8 shows the progressions of the cost functions of the shielded CSI-EPT reconstruction algorithm with quantization step applied to noisy data with a SNR of 35dB for the amplitude and phase separately. For the distributions of the cost function for all subjects, the largest peeks are removed from the progression, since those would make the image less interpretable.

The quantization steps are clearly shown in the progression of the cost function by the spikes which are an order of magnitude higher than the remainder of the cost function. The quantization is only performed on the contrast function, not affecting the other quantities. The cost function and its respective analytic gradients do not account for this, resulting in the introduction of these large errors. The continuous differentiable stack sigmoid could be incorporated in the optimization for the contrast function, but this would lead to an extreme increase in computational complexity as. Right now the contrast function can be reconstructed from the contrast source by using the closed form minimum squares solution; including the stacked sigmoid in this would require an iterative process to reconstruct the contrast function from the contrast source.

The final value of the cost function after 2000 iteration of quantized shielded CSI-EPT is approximately 10^{-3}, which is two orders of magnitude larger than the results shown for the ideal noiseless setup. This shows that the algorithm is less capable of modeling the noise, resulting in a larger data-residual and thus a larger cost-function.

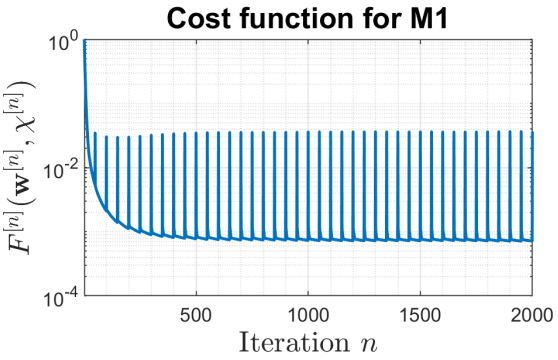

(a) Progression of the cost function for subject M1

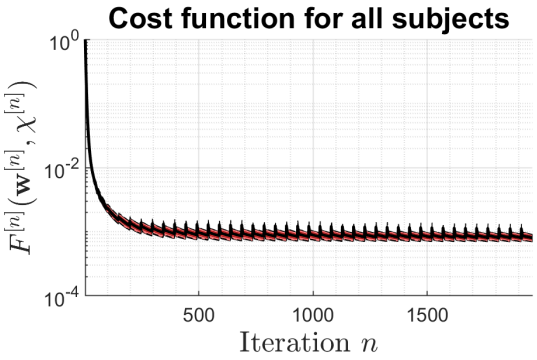

(b) Distribution of the cost function for all subjects. The black line shows the mean of all cost functions, the red regions show the area span by once or twice the standard deviation, while the dashed lines represent the maximum and the minimum of all cost functions

Figure 5.8: Progression of the cost function as a function of the iteration number for the noisy(SNR=35dB) 2D, truly E-polarized simulation setup

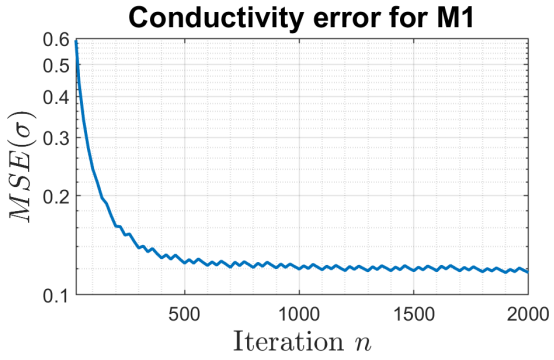

(a) Progression of the reconstruction error for the conductivity of subject M1

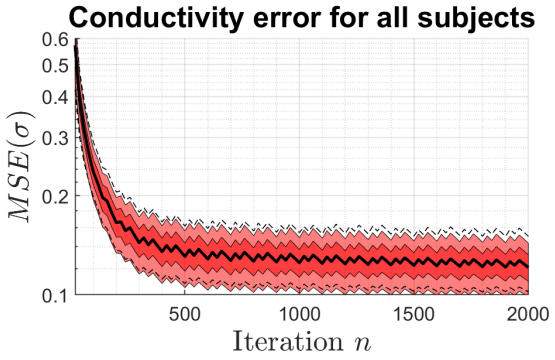

(b) Distribution of the reconstruction error for the conductivity for all subjects. The black line shows the mean, the red regions show the area span by once or twice the standard deviation, while the dashed lines represent the maximum and the minimum.

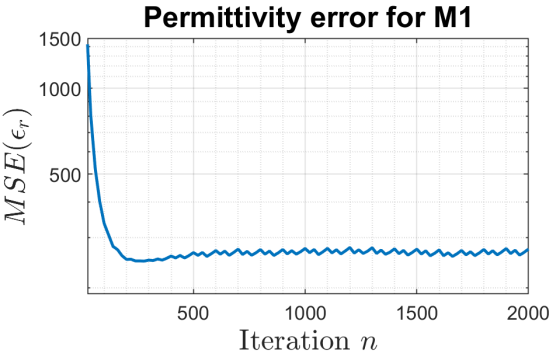

(c) Progression of the reconstruction error for the relative permittivity of subject M1

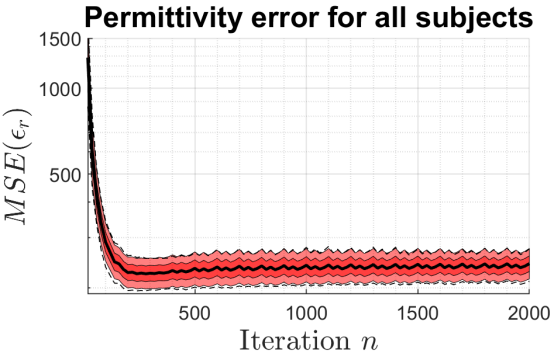

(d) Distribution of the reconstruction error for the relative permittivity for all subjects. The black line shows the mean, the red regions show the area span by once or twice the standard deviation, while the dashed lines represent the maximum and the minimum.

Figure 5.9: Reconstruction errors for the electrical properties for the noisy(SNR=35dB) 2D, truly E-polarized simulation setup

Reconstruction errors

Figure 5.9 shows the reconstruction errors measured using the MSE for the conductivity and relative permittivity; Figs. 5.9a and 5.9c shows these for subject M1, while Figs. 5.9b and 5.9d show the distributions of these for all subjects. The reconstruction errors are calculated once every 20 iteration, resulting in this sawtooth-like line for the reconstruction error. This sampling is performed as it results in a lower computational load, in comparison to calculating the MSE every iteration.

The progression of the MSE of the conductivity shows that the function always descending, reaching a minimum of 0.12 after 2000 iterations, which results in an average deviation from the ground truth of approximately 0.34 S/m. The worst case amongst all subjects has a minimum of 0.16 after 2000 iterations, corresponding with an average deviation of 0.4 S/m.

For the progression of the MSE of the permittivity, the minimum is occurs not at the end of the iterative process, but approximately around iteration 250. This shows that, while not visible in the progression of the cost function, a quantitatively better reconstruction of the permittivity values is found during the iterative process after which it converged to a worse solution. The final value of the MSE of the permittivity after 2000 iterations is approximately 250, resulting in an average deviation of 16. This shows that the reconstruction of the permittivity becomes significantly worse when noise is added to the measurements, in comparison to the performance decay of the conductivity.

In the noiseless simulation setup, subject M69 converged towards a wrong solution for the relative permittivity, shown by MSE which was significantly higher then for all other subjects. This outlier is no longer present in this simulation. The constraints imposed by the quantization steps leads to the algorithm not being stuck in a wrong local minimum, and converging to a better reconstruction.

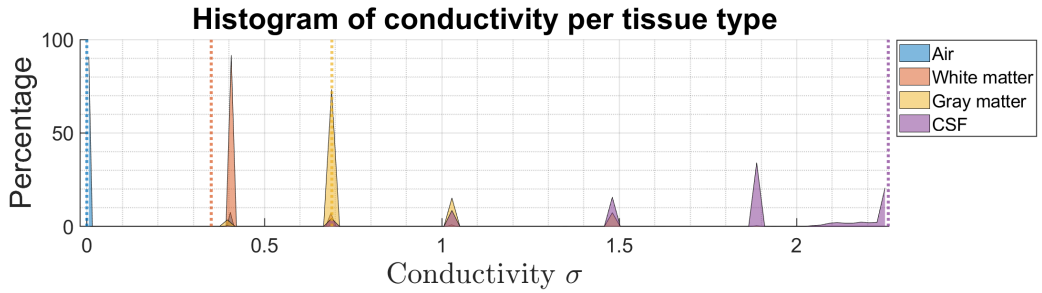

(a) Histograms for the reconstructed conductivity of subject M1

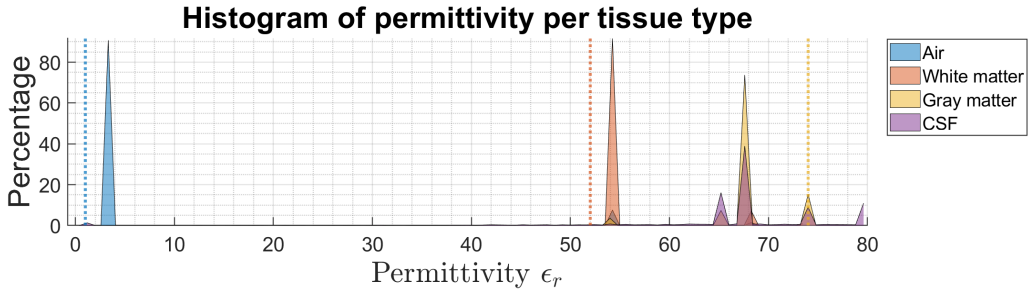

(b) Histograms for the reconstructed relative permittivity of subject M1

Figure 5.10: Histograms of the reconstructed electrical properties per tissue after 2000 iterations for the noisy(SNR=35dB) 2D, truly E-polarized simulation setup

Histogram

Figure 5.10 shows the distributions of the tissue parameters for the different tissues after 2000 iteration of quantized shielded CSI-EPT. Due to the quantization the tissues can only take very specific tissue parameters, leading to the histograms being collection of sharp peaks.

The histogram of the conductivity shows that most tissues are reconstructed well; the white matter is slightly over estimated, most of the gray matter is reconstructed well, and the CSF is mostly underestimate. In the histogram of the conductivity in the noiseless simulation, a low valued left-sided tail of the CSF was present, which now became more present in the due to the influence of noise. The segmentation in the quantization step now used several clusters to represent this large left-sided tail resulting in the smaller peaks in the histograms plot.

The histogram of the permittivity shows that quantization step was able to distinguish the white matter from the reconstruction well, while slightly being overestimated. The support of the gray matter and CSF however were less accurately found. Both these tissues are segmented to having a value of approximately 67.5, which is a severe underestimation for both tissues. The overlap of the two tissues is as expected as the noiseless simulation setup already showed that the CSF surrounding the brain is extremely hard to reconstruct well.

The segmentation in the quantization step was performed on the contrast function, meaning that the modes in the conductivity and permittivity are still linked. The segmentation method was able to accurately find the support of the white and gray matter, shown by the large peaks for these tissues, while the support of CSF was much harder to reconstruct as this is divided over many peaks. This is a result of a good magnitude reconstruction of the contrast source, while the phase is less accurately reconstructed. This poor phase reconstruction caused for the wrong placement of the modes for the conductivity, and especially the relative permittivity.

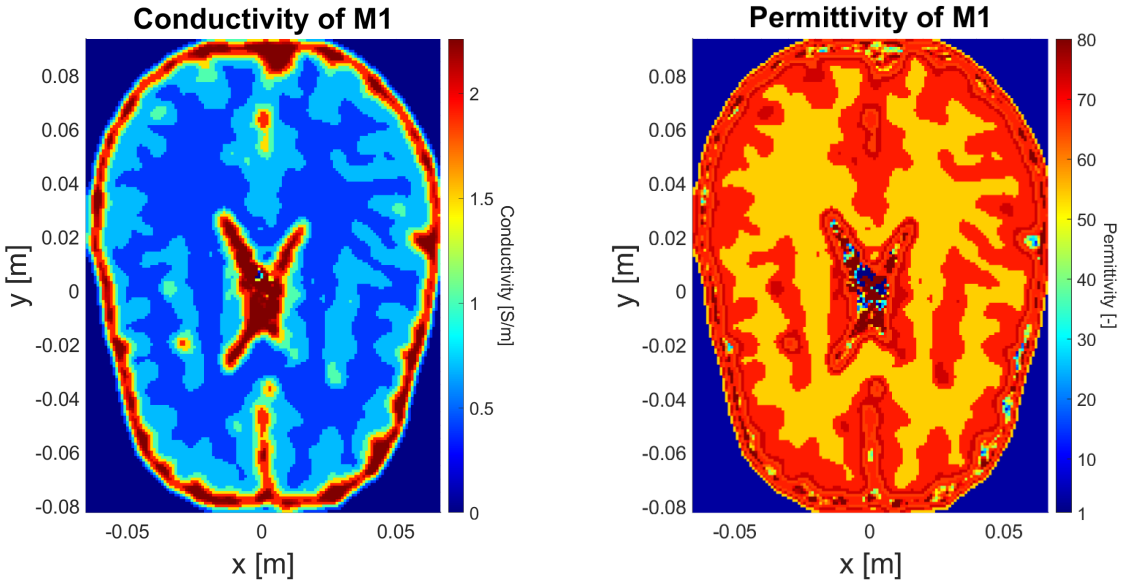

(a) Reconstructed conductivity of subject M1

(b) Reconstructed relative permittivity of subject M1

Figure 5.11: Reconstructed electrical properties after 2000 iterations for the noisy(SNR=35dB) 2D, truly E-polarized simulation setup

Reconstruction image

Figure 5.11 shows the reconstructed tissue parameters for subject M1 after 2000 iteration of quantized shielded CSI-EPT.

The large regions of the gray and white matter can easily be recognized, but many details are lost. This is primarily caused by the low pass filtering required for the segmentation. The expected effect of a poor reconstruction near the center, where the electric field vanishes is visible (in contrary to the noiseless simulation setup), as shown by the variance of the reconstructed conductivity near the origin. Most of the smaller CSF features in the origin can still be found, although these appear much larger , also having a much lower amplitude. This smoothing at the tissue boundaries is caused by the smoothness of the continuous fields, in addition to the low pass filtering. The noise also caused for the introduction of a few phantoms (small features in the reconstructions where the conductivity is estimated too large). These phantoms could be interpreted wrongly, and thus one should be careful drawing conclusions from them.

The reconstruction of the relative permittivity appears similar to that of the conductivity, in the sense that the large regions of the white and gray matter can easily be recognized (while over estimated in general). This is caused by the segmentation on the contrast function where the segmentation is performed jointly on the conductivity and permittivity. In the permittivity reconstruction however, the performance of the reconstruction of the CSF is extremely poor. Both at the center of the image, where the reconstruction is expected to perform poor, as at the CSF surrounding the brain the values are underestimated. The CSF itself is unrecognizable from this image, while the tissue between the CSF and the gray matter can be recognized in the image.

Conclusion

The simulations in this section showed the performance of the quantized shielded CSI-EPT reconstruction algorithm when applied to a noisy E-polarized dataset, using a realistic noise level of 35dB for the amplitude and phase of the measured signal. This section showed that the quantization method significantly increases the reconstruction accuracy, when comparing it to the reconstruction on the same data without quantization. It also confirmed the conclusion drawn from the noiseless simulation, which stated that the conductivity can be reconstructed more accurate than the permittivity, due to its dominance in the contrast source and function.

5.5. Reconstruction 3D dataset

While the geometry of the measurement setup allows for the assumption of full E-polarization of the electromagnetic waves, this is not necessarily true. This section will discuss the reconstruction performance when the shielded CSI-EPT is tested on realistic three-dimensional fields supplied by the ADEPT dataset.

The electric and magnetic fields generated in the ADEPT dataset are generated using the Sim4Life electromagnetic full-wave solver [40]. This full-wave solver calculates the fields, taking into account the finiteness of the birdcage coil and its shielding, and calculates the fields for all slices simultaneously. This results in fields which are no longer truly E-polarized, meaning that that the electric field is no longer completely in the longitudinal (z) direction, and the magnetic field is no longer only in the transversal (x, y) plane. The incident fields are still calculated using Eq. 3.10 and its magnetic counterpart using an excitation factor $\alpha = \frac{1}{40}$. This term is now chosen heuristically, but could also be added as an extra optimization parameter for the iterative process at the cost of a higher computational complexity and loss of accuracy.

As stated prior, due to a low-frequency artifact in the image caused by the model mismatch between the two-dimensional E-polarized model and fully three-dimensional data simulated data, the quantization method proposed in Chapter 4 is no longer viable. This means that the simulations in this section will be based on just the shielded CSI-EPT method, without this quantization step.

Cost function

Figure 5.12 shows the progression of the cost function as a function of iteration number for 2000 iterations; Fig. 5.12a shows the progression for subject M1, while Fig. 5.12b shows the distribution for all subjects.

Even when the E-polarization is assumed, the cost function still converges to a minimal value. However, this value is significantly higher for this three-dimensional simulation than for the aforementioned truly E-polarized noisy and noiseless measurement setups; the final value of this cost function is approximately $8 \cdot 10^{-3}$, compared to the $7 \cdot 10^{-4}$ and $9 \cdot 10^{-6}$ of the noisy and noiseless E-polarized cost functions, respectively. By definition of the cost function, this already means that either or both the simulated fields could not be accurately matched, and/or that (the two-dimensional) Maxwell's equations were no longer adhered. For the assumption that the fields are E-polarized an invariance along the longitudinal z direction is assumed. For a an arm or leg, this assumption can become rather valid, but for a vastly changing object such as a head, this assumption becomes less valid. This dependency on z would lead to the Maxwell's equations no longer being separable in just the E and H polarized planes (for which we only consider the E-polarized wave).

The progressions of the cost functions of all subjects appear to be overlapping, leading to a distribution of lines for which the variance is hardly noticeable (there is a small variance present between the lines). This lack of variance sparked a further investigation into the ADEPT dataset, where it became apparent that while there are 120 different subjects, these are created from the same 7 brains, altered by a slight translation, rotation, are change in tissue parameters. This would result in a lower variation as the simulation setups become very similar in this instances. This would inherently also result in an extremely low variance for the noiseless and noisy simulations, where a higher variance is observed.

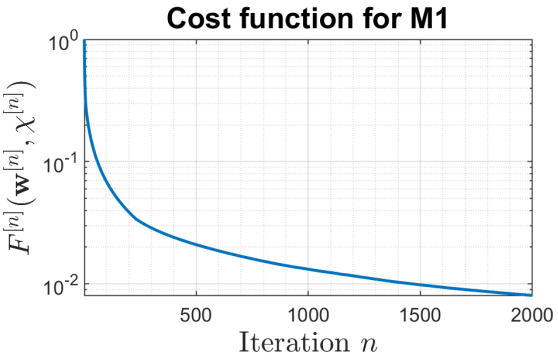

(a) Progression of the cost function for subject M1

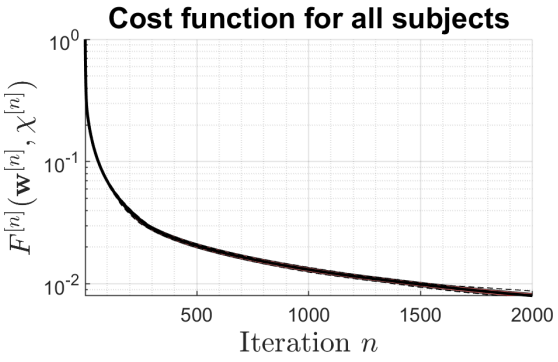

(b) Distribution of the cost function for all subjects. The black line shows the mean of all cost functions, the red regions show the area span by once or twice the standard deviation, while the dashed lines represent the maximum and the minimum of all cost functions

Figure 5.12: Progression of the cost function as a function of the iteration number for the realistic 3D simulation setup

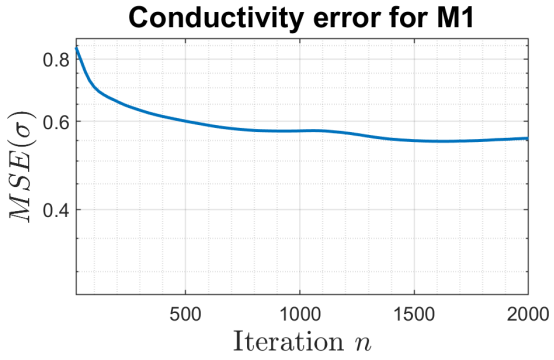

(a) Progression of the reconstruction error for the conductivity of subject M1

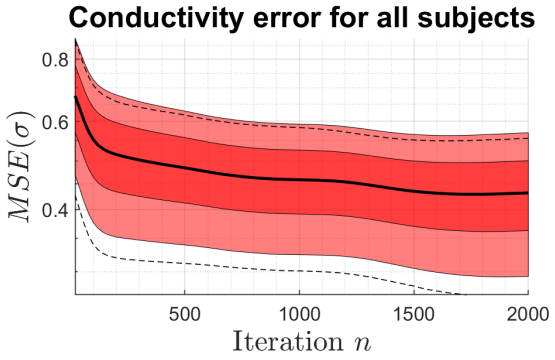

(b) Distribution of the reconstruction error for the conductivity for all subjects. The black line shows the mean, the red regions show the area span by once or twice the standard deviation, while the dashed lines represent the maximum and the minimum

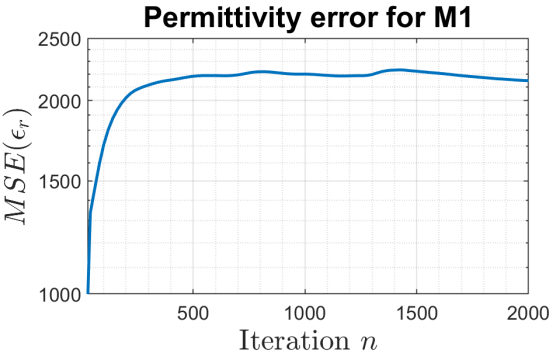

(c) Progression of the reconstruction error for the relative permittivity of subject M1

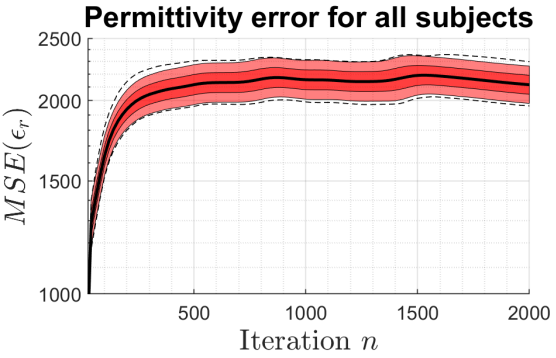

(d) Distribution of the reconstruction error for the relative permittivity for all subjects. The black line shows the mean, the red regions show the area span by once or twice the standard deviation, while the dashed lines represent the maximum and the minimum

Figure 5.13: Reconstruction errors for the electrical properties for the realistic 3D simulation setup

Reconstruction error

Figure 5.13 shows the reconstruction errors of the conductivity and relative permittivity; Figs. 5.13a and 5.13c shows these for subject M1, and Figs. 5.13b and 5.13d show the distributions for all subjects.

For both the noiseless and noisy truly E-polarized simulation setups, the progressions of the reconstruction error of the conductivity followed the trend of the cost functions. This is caused since both represent an MSE. The quantity of which the MSE is taken in the cost function (disregarding the normalization factors), is the scattered B_1^+-field, which is calculated by applying a linear operator on the product of the contrast function and the electric field. For these previous simulation all operators accurately described these, thus these functions becomes very similar. For this simulation, where the operators do not accurately describe the fields, this similarity is lost. For the reconstruction error of the conductivity this is shown by the increasing error around 1000 iterations, and the function ending ascendingly (for all previous simulations these were always descending functions). The lowest value of the MSE of the conductivity value, which now does not correspond with the lowest value of the cost function, is 0.55, which is significantly higher than the 0.12 and 0.04 of the noisy and noiseless simulations. This MSE would result in an average deviation from the ground truth of 0.75 S/m, which is larger than the absolute value of the gray or white matter. The large variance in the distribution of the reconstruction errors shows an inconsistent performance across the different subjects.

As shown before, the permittivity was already much harder to reconstruct, and for the three-dimensional simulation this is not different. The reconstruction algorithm, while converging to a solution, converges to a completely wrong solution. The initial estimate generated by the back-propagation method performs quantitatively better, than any reconstruction in later iterations.

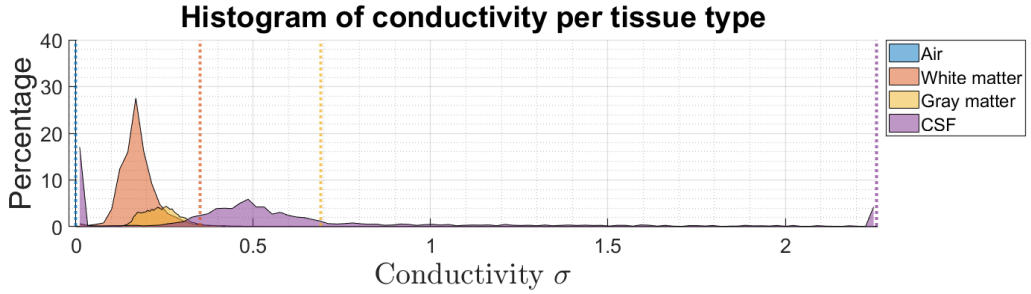

(a) Histograms for the reconstructed conductivity of subject M1

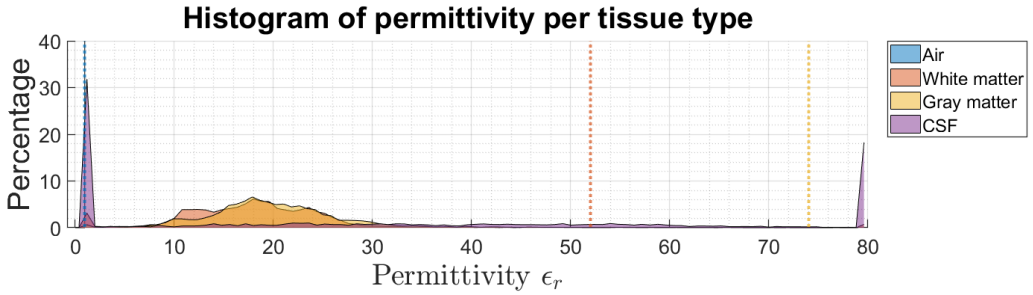

(b) Histograms for the reconstructed relative permittivity of subject M1

Figure 5.14: Histograms of the reconstructed electrical properties per tissue after 2000 iterations for the realistic 3D simulation setup

Histogram

Figure 5.14 shows the distributions of the reconstructed tissue parameters for the different tissues; Fig. 5.14a shows the distributions for the conductivity, and Fig. 5.14b display the permittivity distributions.

The histograms of the conductivity, as displayed in Fig. 5.14a, show a general underestimation of the conductivity for all three tissue types. The means different modes of the tissues are ordered correctly, but their absolute value is incorrect. The variance of these modes is also significantly higher, than for either the noiseless of noisy simulations. The translation of these modes, and the higher variances caused for the modes to be overlapping, meaning that the modes cannot be divided clearly based on only the tissue parameters. This is also the reason why the quantization step of Chapter 4 is not viable.

The distributions of the permittivity values for the different tissues show a complete overlap of the modes of the white and gray matter, and the CSF is mapped to the edges of the domain. Where the permittivity was already are much harder to estimate parameter in the noiseless and noisy simulations, it has now become nearly impossible to estimate them. The three-dimensional displacement current is not accurately represented by the two-dimensional field description of Chapters 2 and 3. Given that the displacement current was already the smaller part of the equivalent current-source, small deviation (e.g. caused by noise) can lead to extremer effects on its reconstruction.

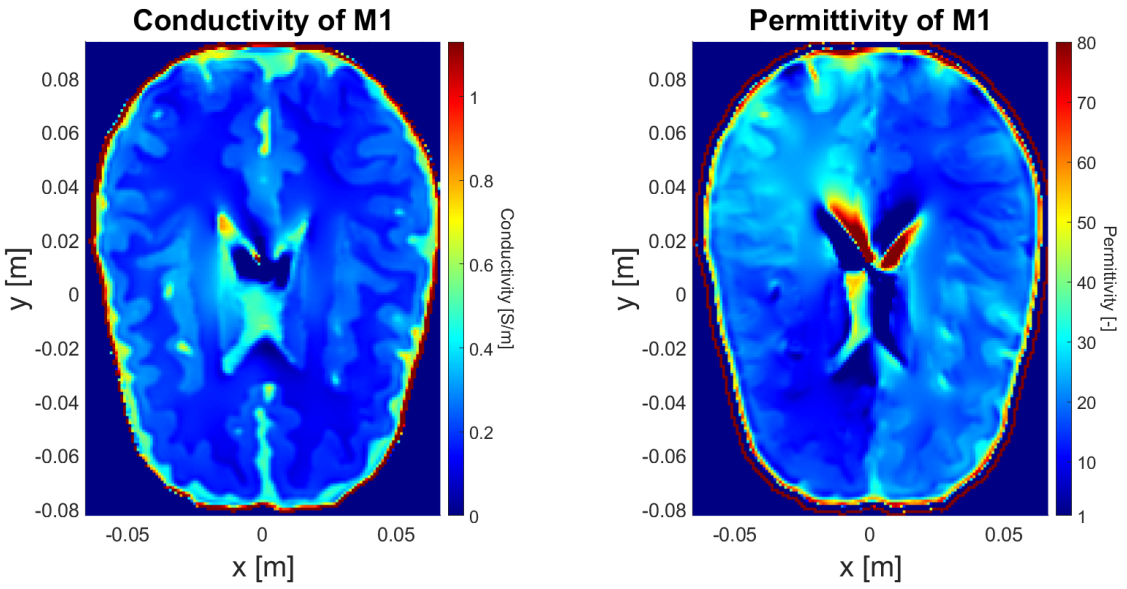

(a) Reconstructed conductivity of subject M1

(b) Reconstructed relative permittivity of subject M1

Figure 5.15: Reconstructed electrical properties after 2000 iterations for the realistic 3D simulation setup

Reconstruction image

Figure 5.15 shows the reconstructed tissue paramters of subject M1 after 2000 iterations using realistic three-dimensional simulated measurements; Fig. 5.15a shows the conductivity, and Fig. 5.15b shows the relative permittivity. Note that the color range in Fig. 5.15a (0 to 1.1 S/m) spans half the range of the colors shown in Figs. 5.5 and 5.11, which span from 0 to 2.2 S/m.

The reconstructed conductivity values are structurally much lower than the ground truth. There is a significant bright-spot near the center of the reconstruction. The vanishing electric field near the center of the birdcage coil causes an significant increase in the contrast function here. While this underestimation, and the presence of this low-frequency artifact leads to a quantitative poor performance, the conductivity is still very useful qualitatively. The different tissue can easily be recognized, and most small features of CSF can still be recognized by a sudden increase of the conductivity. The reconstructed conductivity images show more of these small features, which are not present in the ground truth. An example of such a phantom feature is the bright-spot around $(x, y) = (0.03, -0.015)$. These features could easily be misinterpreted, or the other could be interpreted as phantoms introduced by the reconstruction tools, as both are as likely.

As shown in the distributions of the permittivity values, the permittivity reconstruction no longer possesses any useful information. While the CSF surrounding the brain might be recognizable, no other tissue boundaries can be seen. A better estimate of this permittivity would be to classify the different tissues using the conductivity values, and using this classification towards the different tissues, map the most commonly found permittivity value for each of those tissue types.

Conclusion

This simulation showed the results for the simulation on the realistic three-dimensional dataset from ADEPT. The simulations showed a qualitative good performance for the reconstruction of the conductivity, where the shape of the different tissues can be recognized, but the true values of these tissues is not reconstructed well. Besides being generally underestimated, the modes of the different tissues are overlapping, leading to a quantitative inability if distinguishing between the tissues. The reconstruction of the permittivity showed a worse performance, both qualitatively and quantitatively. In the reconstructions hardly any difference between the tissues can be observed, and the histograms of the different tissues are completely overlapping.

Appendix F.2 shows an increased reconstruction performance when the greens operators are multiplied with $2j$. This 'correction' was achieved purely heuristically by committing inverse crime, thus the conclusion will not be drawn based on it. Yet, the results are significantly better across several subjects, thus this require more research.

6

Conclusion

This thesis presented a method for analytically accounting for RF-shielding in two-dimensional CSI-EPT using shielded birdcage coil. This was achieved formulating the boundary value problem, such that the effects of the shielding could be taken into account in the Greens functions analytically. The presence of this shielding lead to the loss of a spatial (or shift) invariance of the Greens function, disallowing for the fast implementation of the convolution by the FFTs. This work proposed a method of efficiently implementing the discretized Greens operators by exploiting the low-rank structure caused by the degenerate or separable kernel of the correction terms for the modified Greens function. This allowed running the shielded CSI-EPT algorithm on a standard laptop within a reasonable amount of time; otherwise specialized hardware and more time would have been required to use the shielded implementation.

Due to poor robustness when applying the shielded CSI-EPT algorithm on noisy data, a method of including the multi-modality of the tissue parameters has been proposed and tested for the E-polarized fields. This work proposed a method of quantizing the space of the tissue parameters, constraining the optimization process. The quantization achieved by applying the segmentation method of K-means clustering, achieved a significant increase reconstruction accuracy for higher noise-levels, at the cost of a slight decrease in this performance for noise levels, due to the low pass filtering required for the K-means to perform well.

The truly E-polarized simulations showed that the tissue parameters can be reconstructed well, even when considering noise measurements. The conductivity can be reconstructed much better than the relative permittivity, since at 3T the imaginary part of the contrast function (corresponding to the conduction current) is significantly larger than its real counterpart (corresponding to the displacement current). For higher field machines (7T, 14T) this difference might become less. When applying the quantization method, this difference already becomes smaller since the segmentation is performed jointly on the conductivity and permittivity (since it is applied on the contrast function).

The application of the two-dimensional shielded CSI-EPT on more realistic three-dimensional simulated data (ADEPT) showed useful qualitative results, while having a poor quantitative result. The support of the different tissues inside the brains could be recognized well, but the actual conductivity and permittivity values could not be reconstructed well. Due to the model mismatch between the two- and three-dimensional data, a low-frequency artifact is present in the reconstruction, disallowing for the quantization method. The two-dimensional CSI-EPT method, due to the E-polarization, assumes an invariance along z, thus imaging structures that are more invariant along this direction (e.g. an arm or leg) would improve the reconstruction.

In conclusion, the shielded CSI-EPT method described in this thesis is a more accurate description of the E-polarized waves in a shielded birdcage coil, allowing for a more robust and accurate reconstruction of the electrical properties. Its application on realistic three-dimensional data, while significantly better than previous methods, does not provide a quantitative good reconstruction, suggesting the assumption of full E-polarization is not fully correct. Qualitatively the shielded CSI-EPT is promising allowing for good identification of different tissues visually (which could also be achieved by complex post-processing techniques).

6.1. Future research

This thesis already showed promising results for the reconstruction of tissue parameters; yet further research is required.

The birdcage coil in the shielded CSI-EPT method is assumed to be a collection of infinitesimally thin line-currents. In reality, however, this current distribution is much more complex. Accurately modeling this current distribution will lead to a more accurate incident field. The object of interest is in the near-field of the rungs of the birdcage coil, which will load the antennas, altering the radiation of these antennas. This loading will therefore also change the incident field.

The current method of quantization segments the image into a fixed K (often set to 6) amount of clusters which corresponds to a certain amount of tissue types present in one image. K-means clustering and many other clustering methods require an accurate estimate of this number. Therefore, an analysis must be performed for accurately estimating this number of different tissues in an image, interim the optimization process. As stated prior, more complex clustering methods could be applied in post-processing to further increase the classification, and corresponding evaluation of the tissue parameters during or after reconstruction.

The reconstructions could be used in a pseudo-3D manner for an initialization for a more complex full 3D (CSI-)EPT method. A good initialization could reduce the total computation time for such a complex method. The segmentation methods (which are now defined for two-dimensional image images) could be extended to three dimensions. The methods for the segmentation could then be used once on the final reconstruction only for the three-dimensional approaches. Also an analysis on the reduction of the computational load for the three dimensional methods using this as initialization would allow for (if the reduction is significant) an easier application of these complex methods in the clinical domain.

Bibliography

[1] J. Liu, Y. Wang, U. Katscher, and B. He, "Electrical properties tomography based on B_1 maps in mri: Principles, applications, and challenges," en, *IEEE Transactions on Biomedical Engineering*, vol. 64, no. 11, pp. 2515–2530, Nov. 2017, ISSN: 0018-9294, 1558-2531. DOI: 10.1109/TBME.2017.2725140.

[2] L. Wang, "Microwave imaging and sensing techniques for breast cancer detection," en, *Micromachines*, vol. 14, no. 7, p. 1462, Jul. 2023, ISSN: 2072-666X. DOI: 10.3390/mi14071462.

[3] M. Schaefer, W. Gross, J. Ackemann, and M. Gebhard, "The complex dielectric spectrum of heart tissue during ischemia," en, *Bioelectrochemistry*, vol. 58, no. 2, pp. 171–180, Dec. 2002, ISSN: 15675394. DOI: 10.1016/S1567-5394(02)00152-4.

[4] U. Katscher, T. Voigt, C. Findeklee, P. Vernickel, K. Nehrke, and O. DÖssel, "Determination of electric conductivity and local sar via b1 mapping," en, *IEEE Transactions on Medical Imaging*, vol. 28, no. 9, pp. 1365–1374, Sep. 2009, ISSN: 0278-0062, 1558-254X. DOI: 10.1109/TMI.2009.2015757.

[5] M. Cheney, D. Isaacson, and J. C. Newell, "Electrical impedance tomography," en, *SIAM Review*, vol. 41, no. 1, pp. 85–101, Jan. 1999, ISSN: 0036-1445, 1095-7200. DOI: 10.1137/S0036144598333613.

[6] B. Brazey, Y. Haddab, and N. Zemiti, "Robust imaging using electrical impedance tomography: Review of current tools," *Proceedings of the Royal Society A: Mathematical, Physical and Engineering Sciences*, vol. 478, no. 2258, p. 20 210 713, Feb. 2022. DOI: 10.1098/rspa.2021.0713.

[7] P. N. T. Wells and H.-D. Liang, "Medical ultrasound: Imaging of soft tissue strain and elasticity," en, *Journal of The Royal Society Interface*, vol. 8, no. 64, pp. 1521–1549, Nov. 2011, ISSN: 1742-5689, 1742-5662. DOI: 10.1098/rsif.2011.0054.

[8] M. Hemaya, M. Hemaya, and A. Habeeb, "The risks associated with computed tomography scans: An assessment of the readability and reliability of online text available for patient information and guidance," en, *Cureus*, Oct. 2022, ISSN: 2168-8184. DOI: 10.7759/cureus.30758. [Online]. Available: https://www.cureus.com/articles/121619-the-risks-associated-with-computed-tomography-scans-an-assessment-of-the-readability-and-reliability-of-online-text-available-for-patient-information-and-guidance.

[9] E. Balidemaj, C. A. Van Den Berg, J. Trinks, *et al.*, "Csi-ept: A contrast source inversion approach for improved mri-based electric properties tomography," en, *IEEE Transactions on Medical Imaging*, vol. 34, no. 9, pp. 1788–1796, Sep. 2015, ISSN: 0278-0062, 1558-254X. DOI: 10.1109/TMI.2015.2404944.

[10] P. M. V. D. Berg and R. E. Kleinman, "A contrast source inversion method," en, *Inverse Problems*, vol. 13, no. 6, pp. 1607–1620, Dec. 1997, ISSN: 0266-5611, 1361-6420. DOI: 10.1088/0266-5611/13/6/013.

[11] P. M. V. D. Berg, A. L. V. Broekhoven, and A. Abubakar, "Extended contrast source inversion," en, *Inverse Problems*, vol. 15, no. 5, pp. 1325–1344, Oct. 1999, ISSN: 0266-5611, 1361-6420. DOI: 10.1088/0266-5611/15/5/315.

[12] P. R. S. Stijnman, S. Mandija, P. S. Fuchs, C. A. T. van den Berg, and R. F. Remis, "Transceive phase corrected 2d contrast source inversion-electrical properties tomography," en, *Magnetic Resonance in Medicine*, vol. 85, no. 5, pp. 2856–2868, 2021, ISSN: 1522-2594. DOI: 10.1002/mrm.28619.

[13] B. Van Den Bergen, C. C. Stolk, J. B. V. D. Berg, J. J. W. Lagendijk, and C. A. T. Van Den Berg, "Ultra fast electromagnetic field computations for rf multi-transmit techniques in high field mri," en, *Physics in Medicine and Biology*, vol. 54, no. 5, pp. 1253–1264, Mar. 2009, ISSN: 0031-9155, 1361-6560. DOI: 10.1088/0031-9155/54/5/010.

[14] R. L. Leijsen, W. M. Brink, C. A. T. Van Den Berg, A. G. Webb, and R. F. Remis, "3-d contrast source inversion-electrical properties tomography," en, *IEEE Transactions on Medical Imaging*, vol. 37, no. 9, pp. 2080–2089, Sep. 2018, ISSN: 0278-0062, 1558-254X. DOI: 10.1109/TMI.2018.2816125.

[15] R. Leijsen, P. Fuchs, W. Brink, A. Webb, and R. Remis, "Developments in electrical-property tomography based on the contrast-source inversion method," en, *Journal of Imaging*, vol. 5, no. 2, p. 25, Feb. 2019, ISSN: 2313-433X. DOI: 10.3390/jimaging5020025.

[16] Z. Yang, M. Lu, G. Drake, *et al.*, "Rf shielding designs for birdcage coils for preclinical mri at 9.4 t," en, *Magnetic Resonance Imaging*, vol. 94, pp. 1–6, Dec. 2022, ISSN: 0730725X. DOI: 10.1016/j.mri.2022.08.018.

[17] C. A. Balanis, *Advanced engineering electromagnetics*, eng, Second edition. Hoboken, NJ: Wiley, 2012, ISBN: 978-0-470-58948-9.

[18] R. Leijsen, W. Brink, C. Van Den Berg, A. Webb, and R. Remis, "Electrical properties tomography: A methodological review," en, *Diagnostics*, vol. 11, no. 2, p. 176, Jan. 2021, ISSN: 2075-4418. DOI: 10.3390/diagnostics11020176.

[19] E. Plenge, D. H. J. Poot, M. Bernsen, *et al.*, "Super-resolution methods in mri: Can they improve the trade-off between resolution, signal-to-noise ratio, and acquisition time?" en, *Magnetic Resonance in Medicine*, vol. 68, no. 6, pp. 1983–1993, Dec. 2012, ISSN: 0740-3194, 1522-2594. DOI: 10.1002/mrm.24187.

[20] A. Cichocki, N. Lee, I. V. Oseledets, A.-H. Phan, Q. Zhao, and D. Mandic, "Low-rank tensor networks for dimensionality reduction and large-scale optimization problems: Perspectives and challenges part 1," *arXiv preprint arXiv:1609.00893*, 2016.

[21] R. Remis and E. Charbon, "An electric field volume integral equation approach to simulate surface plasmon polaritons," en, *Advanced Electromagnetics*, vol. 2, no. 1, p. 15, Feb. 2013, ISSN: 2119-0275. DOI: 10.7716/aem.v2i1.23.

[22] R. Leijsen, W. Brink, X. An, A. Webb, and R. F. Remis, "Transverse-ept: A local first order electrical properties tomography approach not requiring estimation of the incident fields," en, *Progress In Electromagnetics Research M*, vol. 102, pp. 137–148, 2021, ISSN: 1937-8726. DOI: 10.2528/PIERM21021006.

[23] P. M. V. D. Berg and A. Abubakar, "Contrast source inversion method: State of art," en, *Progress In Electromagnetics Research*, vol. 34, pp. 189–218, 2001, ISSN: 1559-8985. DOI: 10.2528/PIER01061103.

[24] R. Leijsen, "Electrical property mapping using mri," en, Ph.D. dissertation, Leiden University, 2024.

[25] P. S. Fuchs, "Mri based electrical properties tomography," en, M.S. thesis, Delft University of Technology, 2016.

[26] C. Gilmore, "Towards an improved microwave tomography system," en, Jan. 2010. [Online]. Available: http://hdl.handle.net/1993/3850.

[27] C. Gilmore and J. LoVetri, "Enhancement of microwave tomography through the use of electrically conducting enclosures," en, *Inverse Problems*, vol. 24, no. 3, p. 035 008, Jun. 2008, ISSN: 0266-5611, 1361-6420. DOI: 10.1088/0266-5611/24/3/035008.

[28] M. Abramowitz and I. A. Stegun, *Handbook of mathematical functions with formulas, graphs, and mathematical tables* (Applied mathematics series), eng, 10th print. with corrections. Washington, DC: US Government Printing Office, 1972, ISBN: 978-0-318-11730-0.

[29] D. W. Trim, *Applied partial differential equations* (The Prindle, Weber & Schmidt series in mathematics), eng, 4. print. Boston, Mass: PWS-Kent Publ, 1994, ISBN: 978-0-534-92134-7.

[30] B. Fornberg, "Generation of finite difference formulas on arbitrarily spaced grids," en, *Mathematics of Computation*, vol. 51, no. 184, pp. 699–706, 1988, ISSN: 0025-5718, 1088-6842. DOI: 10.1090/S0025-5718-1988-0935077-0.

[31] N. van Dam, "Contrast source inversion electrical property tomography, is the two-dimensional csi algorithm feasible on realistic three-dimensional data?" M.S. thesis, Delft University of Technology, 2024.

[32] [Online]. Available: https://itis.swiss/virtual-population/tissue-properties/database/dielectric-properties.

[33] F. Ros and S. Guillaume, "A hierarchical clustering algorithm and an improvement of the single linkage criterion to deal with noise," en, *Expert Systems with Applications*, vol. 128, pp. 96–108, Aug. 2019, ISSN: 09574174. DOI: 10.1016/j.eswa.2019.03.031.

[34] H. Mittal, A. C. Pandey, M. Saraswat, S. Kumar, R. Pal, and G. Modwel, "A comprehensive survey of image segmentation: Clustering methods, performance parameters, and benchmark datasets," en, *Multimedia Tools and Applications*, vol. 81, no. 24, pp. 35 001–35 026, Oct. 2022, ISSN: 1380-7501, 1573-7721. DOI: 10.1007/s11042-021-10594-9.

[35] V. Faber, "Clustering and the continuous k-means algorithm," en, *Los Alamos Science*, no. 22, 1994.

[36] U. Von Luxburg, "A tutorial on spectral clustering," en, *Statistics and Computing*, vol. 17, no. 4, pp. 395–416, Dec. 2007, ISSN: 0960-3174, 1573-1375. DOI: 10.1007/s11222-007-9033-z.

[37] J. Liu and L. Guo, "An improved k-means algorithm for brain mri image segmentation," en, *3rd International Conference on Mechatronics, Robotics and Automation*, 2015.

[38] K. Ramesh, G. K. Kumar, K. Swapna, D. Datta, and S. S. Rajest, "A review of medical image segmentation algorithms," en, *EAI Endorsed Transactions on Pervasive Health and Technology*, vol. 7, no. 27, e6, Apr. 2021, ISSN: 2411-7145. DOI: 10.4108/eai.12-4-2021.169184.

[39] T. G. Meerbothe, E. F. Meliado, P. R. S. Stijnman, C. A. T. Van Den Berg, and S. Mandija, "A database for mr -based electrical properties tomography with in silico brain data— adept," en, *Magnetic Resonance in Medicine*, vol. 91, no. 3, pp. 1190–1199, Mar. 2024, ISSN: 0740-3194, 1522-2594. DOI: 10.1002/mrm.29904.

[40] ZMT Zurich MedTech AG, *Sim4life*, version 0.20.2, Feb. 19, 2010. [Online]. Available: https://sim4life.swiss/.

A

Scattering formalism

This chapter will describe the scattering formalism in the two-dimensional setting used throughout this thesis. This theory is used to describe the relation between the incident and scattered field operators in Chapters 2 and 3.

The relevant time-domain Maxwell's equations for contrast source inversion are Ampere-Maxwell's and Maxwell-Faraday's equation, as these describe the interaction between the electric and magnetic fields. These equations are:

$$\nabla \times \mathbf{H} + \sigma \mathbf{E} + \partial_t \mathbf{E} = -\mathbf{J}^{\text{ext}} \tag{A.1}$$

$$\nabla \times \mathbf{E} + \mu \partial_t \mathbf{H} = -\mathbf{K}^{\text{ext}} \tag{A.2}$$

Instead of using the vector notation given above, one can write these equations for all the Cartesian components separately. This results in:

$$\begin{aligned} -\partial_y H_z + \partial_z H_y + \sigma E_x + \partial_t E_x &= -J_x^{\text{ext}} \\ -\partial_z H_x + \partial_x H_z + \sigma E_y + \partial_t E_y &= -J_y^{\text{ext}} \\ -\partial_x H_y + \partial_y H_x + \sigma E_z + \partial_t E_z &= -J_z^{\text{ext}}, \end{aligned} \tag{A.3}$$

for Ampere-Maxwell's equation of Eq. A.1 and:

$$\begin{aligned} \partial_y E_z - \partial_z E_y + \mu \partial_t H_x &= -K_x^{\text{ext}} \\ \partial_z E_x - \partial_x E_z + \mu \partial_t H_y &= -K_y^{\text{ext}} \\ \partial_x E_y - \partial_y E_x + \mu \partial_t H_z &= -K_z^{\text{ext}}, \end{aligned} \tag{A.4}$$

for Maxwell-Faraday's of Eq. A.2.

Decoupling E and H polarization

Introducing $\hat{z}$ as the direction of invariance, directly suggests that all derivatives towards z become zero:

$$\partial_z \equiv 0. \tag{A.5}$$

Applying this knowledge on the systems of equations for the component-wise Maxwell equations results in two decoupled systems of equations; the first of which describes E-polarized waves, and the latter H-polarized waves. The system of equations describing these E-polarized waves is:

$$\begin{aligned} \partial_y E_z + \mu \partial_t H_x &= -K_x^{\text{ext}} \\ -\partial_x E_z + \mu \partial_t H_y &= -K_y^{\text{ext}} \\ -\partial_x H_y + \partial_y H_x + \sigma E_z + \partial_t E_z &= -J_z^{\text{ext}}, \end{aligned} \tag{A.6}$$

and the system of equations describing the H-polarized waves is given by:

$$\begin{aligned} -\partial_y H_z + \sigma E_x + \partial_t E_x &= -J_x^{\text{ext}} \\ \partial_x H_z + \sigma E_y + \partial_t E_y &= -J_y^{\text{ext}} \\ \partial_x E_y - \partial_y E_x + \mu \partial_t H_z &= -K_z^{\text{ext}}. \end{aligned} \tag{A.7}$$

The magnetic current sources here are assumed to be zero, as a non-zero magnetic current would suggest a current distribution of magnetic monopoles (which are physically non-existent).

When the object-of-interest, is being scanned using a birdcage coil, it can be assumed that only E-polarized waves are present when considering the center of the birdcage coil. This assumption becomes rather valid, since all currents near the center of the birdcage coil appear to be infinitely long $\hat{z}$-oriented line currents. This shows only the system of equations given by Eq. A.6 has to be considered for the remainder of this report.

However, note that this assumptions breaks down when one considers that, while the line currents appear to be invariant along $\hat{z}$, the object of interest might not. Thus, this assumption can be best made when considering an object which has little variation along the $\hat{z}$-direction, such as arms or legs.

Scattering formalism

Bringing the system of equations of Eq. A.6, which describe the E-polarized waves in time domain, to the frequency domain using the Laplace transform, results in:

$$\begin{aligned} -\partial_x \hat{H}_y + \partial_y \hat{H}_x + \hat{\eta} \hat{E}_z &= -\hat{J}_z^{\text{ext}} \\ \partial_y \hat{E}_z + s\mu \hat{H}_x &= 0 \\ -\partial_x \hat{E}_z + s\mu \hat{H}_y &= 0, \end{aligned} \tag{A.8}$$

where $\hat{\eta}$ describes the per-unit-length admittance of the medium, and is defined as $\hat{\eta}(\mathbf{r}) = \sigma(\mathbf{r}) + s\epsilon(\mathbf{r})$. When $s = j\omega$ this describes the steady-state Fourier transform of the time-domain total electric and magnetic fields (the $\mathbf{r}$ notation is omitted for sake of simplicity, but could be added after all quantities).

First, the situation for when the object is not there will be described, after which the 'contrast' will be added by the influence of this object. This incident field is described as:

$$\begin{aligned} -\partial_x \hat{H}_y^{\text{inc}} + \partial_y \hat{H}_x^{\text{inc}} + \hat{\eta}_0 \hat{E}_z^{\text{inc}} &= -\hat{J}_z^{\text{ext}} \\ \partial_y \hat{E}_z^{\text{inc}} + s\mu_0 \hat{H}_x^{\text{inc}} &= 0 \\ \partial_x \hat{E}_z^{\text{inc}} + s\mu_0 \hat{H}_y^{\text{inc}} &= 0, \end{aligned} \tag{A.9}$$

where all electrical properties (ϵ, μ, σ and consequently η), are that of free-space denoted by the nought-subscript.

Now the domain will be split in two, a subdomain which describes the space within the object, and a domain which describes the space outside of the object. Inside the object no external sources are present, thus Eq. A.8 becomes:

$$\begin{aligned} -\partial_x \hat{H}_y + \partial_y \hat{H}_x + \hat{\eta} \hat{E}_z &= 0 \\ \partial_y \hat{E}_z + s\mu_0 \hat{H}_x &= 0 \qquad \mathbf{r} \in \mathbb{D}^{\text{obj}} \\ -\partial_x \hat{E}_z + s\mu_0 \hat{H}_y &= 0, \end{aligned} \tag{A.10}$$

where $\hat{\eta}$ now contains the electric properties of this domain (μ is assumed not to introduce any contrast). Outside the object, the external sources are present, but the electrical properties are that of the background medium, which in this case is that of free-space. This results in:

$$\begin{aligned} -\partial_x \hat{H}_y + \partial_y \hat{H}_x + \hat{\eta}_0 \hat{E}_z &= -\hat{J}_z^{\text{ext}} \\ \partial_y \hat{E}_z + s\mu_0 \hat{H}_x &= 0 \qquad \mathbf{r} \notin \mathbb{D}^{\text{obj}} \\ -\partial_x \hat{E}_z + s\mu_0 \hat{H}_y &= 0. \end{aligned} \tag{A.11}$$

With this distinction of the waves inside and outside the object, the scattering formalism can be introduced. This formalism states that the total field is the superposition of the incident field, and the field due to

the scatterer (or the object). The scattered fields are then given by:

$$\{\hat{H}_x^{\text{sca}}, \hat{H}_y^{\text{sca}}, \hat{E}_z^{\text{sca}}\} = \{\hat{H}_x - \hat{H}_x^{\text{inc}}, \hat{H}_y - \hat{H}_y^{\text{inc}}, \hat{E}_z - \hat{E}_z^{\text{inc}}\} \tag{A.12}$$

Using this formalism, the scattered fields outside the object's domain will follow the following system of equations:

$$\begin{aligned} -\partial_x \hat{H}_y^{\text{sca}} + \partial_y \hat{H}_x^{\text{sca}} + \hat{\eta}_0 \hat{E}_z^{\text{sca}} &= 0 \\ \partial_y \hat{E}_z^{\text{sca}} + s\mu_0 \hat{H}_x^{\text{sca}} &= 0 \qquad \mathbf{r} \notin \mathbb{D}^{\text{obj}} \\ -\partial_x \hat{E}_z^{\text{sca}} + s\mu_0 \hat{H}_y^{\text{sca}} &= 0. \end{aligned} \tag{A.13}$$

Inside the object's domain, this same system of equations becomes:

$$\begin{aligned} -\partial_x \hat{H}_y^{\text{sca}} + \partial_y \hat{H}_x^{\text{sca}} + \hat{\eta}_0 \hat{E}_z^{\text{sca}} &= -(\hat{\eta} - \hat{\eta}_0)\hat{E}_z \\ \partial_y \hat{E}_z^{\text{sca}} + s\mu_0 \hat{H}_x^{\text{sca}} &= 0 \qquad \mathbf{r} \in \mathbb{D}^{\text{obj}} \\ -\partial_x \hat{E}_z^{\text{sca}} + s\mu_0 \hat{H}_y^{\text{sca}} &= 0, \end{aligned} \tag{A.14}$$

implying the presence of a scattering source for the inhomogeneous Helmholtz' equation. This scattering source is then defined as:

$$\hat{J}_z^{\text{sca}} = \begin{cases} (\hat{\eta} - \hat{\eta}_0)\hat{E}_z & \text{when } \mathbf{r} \in \mathbb{D}^{\text{obj}} \\ 0 & \text{when } \mathbf{r} \notin \mathbb{D}^{\text{obj}} \end{cases} \tag{A.15}$$

B

Derivation for Fourier expansion term Bn

In literature the B_n term of Gilmores analytic solution to the shielded Greens function has discrepancies. This appendix gives the full derivation of B_n to show the correct result. This Appendix will include all the 'π-terms', which come from the orthonormal eigenfunctions in [26][27]. All these terms cancel on each other and are therefore not present in Eq. 3.5 and 3.6. The derivation for the Fourier expansion coefficient is given by:

$$B_n\left(\mathbf{r}'\right) = \frac{-1}{\sqrt{\pi} J_n\left(ka\right)} \int_{-\pi}^{\pi} \hat{g}(a,\theta,\mathbf{r}') \sin\left(n\theta\right) \mathrm{d}\theta \tag{B.1}$$

$$\hat{g}\left(\mathbf{r},\mathbf{r}'\right) = \frac{1}{4j} H_0^{(2)}\left(k_0|\mathbf{r}-\mathbf{r}'|\right) \tag{B.2}$$

The Hankel function can be expanded in the following series according to [17]:

$$H_0^{(2)}\left(k|\mathbf{r}-\mathbf{r}'|\right) = \begin{cases} \sum_{m=-\infty}^{\infty} J_m\left(kr\right) H_m^{(2)}\left(kr'\right) e^{jm(\theta-\theta')} \text{ for } r \leq r' \\ \sum_{m=-\infty}^{\infty} J_m\left(kr'\right) H_m^{(2)}\left(kr\right) e^{jm(\theta-\theta')} \text{ for } r \geq r' \end{cases} \tag{B.3}$$

Since the Hankel function in the free-space Greens function g_{fs} is evaluated at $\mathbf{r} = \mathbf{a}$, where $\mathbf{a}$ is located at the shield's surface, $\mathbf{r} > \mathbf{r}'$ so only the second form of the Hankel series expansion is required.

Applying this series expansion of $H_0^{(2)}$ on Eq. B.1 gives:

$$B_n = \frac{-1}{4j\sqrt{\pi} J_n(ka)} \int_{-\pi}^{\pi} \sum_{m=-\infty}^{\infty} J_m(kr') H_m^{(2)}(ka) e^{jm(\theta-\theta')} \sin\left(n\theta\right) \mathrm{d}\theta \tag{B.4a}$$

$$= \frac{-1}{4j\sqrt{\pi} J_n(ka)} \sum_{m=-\infty}^{\infty} J_m(kr') H_m^{(2)}(ka) e^{-jm\theta'} \int_{-\pi}^{\pi} e^{jm\theta} \sin\left(n\theta\right) \mathrm{d}\theta \tag{B.4b}$$

The final integral in equation B.4b will now be evaluated separately. First by decomposing the sine term using Euler's identity:

$$\int_{-\pi}^{\pi} e^{jm\theta} \sin\left(n\theta\right) \mathrm{d}\theta = \int_{-\pi}^{\pi} e^{jm\theta} \frac{e^{jn\theta} - e^{-jn\theta}}{2j} \mathrm{d}\theta \tag{B.5a}$$

$$= \int_{-\pi}^{\pi} \frac{e^{j(m+n)\theta} - e^{j(m-n)\theta}}{2j} \mathrm{d}\theta \tag{B.5b}$$

This final integral consists of a term containing $(m+n)$ and another term containing $(m-n)$. The integral will be solved for those separately. First the term containing $(m+n)$ will be solved for $m+n \neq 0$:

$$\int_{-\pi}^{\pi} \frac{e^{j(m+n)\theta}}{2j} \mathrm{d}\theta = \left[\frac{e^{j(m+n)\theta}}{-2(m+n)} \right]_{\theta=-\pi}^{\pi} \tag{B.6a}$$

$$= \frac{e^{j(m+n)\pi} - e^{-j(m+n)\pi}}{-2(m+n)} = \frac{j\sin\left((m+n)\pi\right)}{-(m+n)} \tag{B.6b}$$

, which equal zero as the sine function has zeros at integer multiples of π. For $m+n=0$ this integral becomes much simpler, resulting in:

$$\int_{-\pi}^{\pi} \frac{1}{2j} \mathrm{d}\theta = -j\pi \tag{B.7}$$

The second term of Eq. B.5b containing the $(m-n)$ term can be solved. First the integrals for when $m-n \neq 0$ will be solved using:

$$\int_{-\pi}^{\pi} -\frac{e^{j(m-n)\theta}}{2j} \mathrm{d}\theta = -\left[\frac{e^{j(m-n)\theta}}{-2(m-n)}\right]_{\theta=-\pi}^{\pi} \tag{B.8a}$$

$$= -\frac{e^{j(m-n)\pi} - e^{-j(m-n)\pi}}{-2(m-n)} = -\frac{j\sin((m-n)\pi)}{-(m-n)}, \tag{B.8b}$$

which again equal zeros as the sine is only evaluated at integer multiples of π. The integral for when $m-n=0$ is again much simpler:

$$\int_{-\pi}^{\pi} -\frac{1}{2j} \mathrm{d}\theta = j\pi \tag{B.9}$$

This shows that the infinite sum in equation B.4b only has a value at $m=n$ or $m=-n$, which are scaled with $j\pi$ and $-j\pi$, respectively. This means Eq. B.1 can be written as:

$$B_n = \frac{-\pi}{4\sqrt{\pi} J_n(ka)} \left[J_n(kr') H_n^{(2)}(ka) e^{-jn\theta'} - J_{-n}(kr') H_{-n}^{(2)}(ka) e^{jn\theta'} \right] \tag{B.10}$$

Showing the correct form of B_n should include the minus-sign at the second Hankel term.

C

Correction for shielded Greens function proposed in literature

This appendix will prove that the modified Greens function proposed by Gilmore in [26][27], does not solve the differential equation it is trying to solve. After which a correction is proposed to make the corrected Greens function solve the boundary value problem.

The first section gives the necessary theory and conditions which the Greens function must obey, where the second section discusses the Greens function proposed in [26][27]. Finally a correction will be proposed to make the Greens function described in literature solve the derived boundary value problem.

Since $\mathbf{r} > \mathbf{r}'$, which is valid since $\mathbf{r}$ is laying on the outer edge of the domain of interest and $\mathbf{r}'$ is somewhere within this domain, Eq. 2.6 can be written as:

$$g_{fs}(\mathbf{r},\mathbf{r}') = \frac{1}{4j}\sum_{m=-\infty}^{\infty} J_n(k|r'|)H_m^{(2)}(kr)e^{jn(\theta-\theta')}, \tag{C.1}$$

where $\mathbf{r} = [r,\theta]^T$ and $\mathbf{r}' = [r',\theta']^T$ are the cylindrical representations of $\mathbf{r}$ and $\mathbf{r}'$. This final equation will be the goal for what p must reach when considering $\mathbf{r} \in \Omega$.

Greens function proposed in literature

In [26][27] the following eigenfunction is proposed as the solution for the correction term p:

$$p(\mathbf{r},\mathbf{r}') = \frac{A_0(\mathbf{r}')}{\sqrt{2\pi}}J_0(kr) + \sum_{n=1}^{\infty} A_n(\mathbf{r}')J_n(kr)\frac{\cos(n\theta)}{\sqrt{\pi}} + B_n(\mathbf{r}')J_n(kr)\frac{\sin(n\theta)}{\sqrt{\pi}}, \tag{C.2}$$

where A_n and B_n are given by:

$$A_n(\mathbf{r}') = \frac{-\pi}{4j\sqrt{\pi}J_n(ka)}\left[J_n(kr')e^{-jn\theta'}H_n^{(2)}(ka) + J_{-n}(kr')e^{jn\theta'}H_{-n}^{(2)}(ka)\right] \tag{C.3a}$$

$$B_n(\mathbf{r}') = \frac{-\pi}{4\sqrt{\pi}J_n(ka)}\left[J_n(kr')e^{-jn\theta'}H_n^{(2)}(ka) - J_{-n}(kr')e^{jn\theta'}H_{-n}^{(2)}(ka)\right], \tag{C.3b}$$

where a denotes the radius of the RF-shield. Note in this appendix that the correct expression for B_n is used, which is derived in Appendix B.

The remainder of this section will use the fact that $r = a$ when $\mathbf{r} \in \Omega$, and fills this and Eq. C.3a and C.3b in the expression of p given in Eq. C.2 to show that this is not equal to $-g^{EJ}$, which was condition that must hold. Substituting the expansion coefficients will be done in three parts: the order 0 term, the terms corresponding with the cosine eigenfunctions, and the terms corresponding with the sine eigenfunctions.

The first eigenfunction, with the order 0 expansion coefficient becomes:

$$\frac{A_0(\mathbf{r}')}{\sqrt{2\pi}}J_0(kr) = \frac{-\pi}{4j\sqrt{\pi}J_0(ka)}\left[J_0(kr')H_0^{(2)}(ka) + J_0(kr')H_0^{(2)}(ka)\right]\frac{1}{\sqrt{2\pi}}J_0(ka) \tag{C.4a}$$

$$= \frac{-1}{4j\sqrt{2}}\left[2J_0(kr')H_0^{(2)}(ka)\right] \tag{C.4b}$$

$$= \frac{-\sqrt{2}}{4j}J_0(kr')H_0^{(2)}(ka). \tag{C.4c}$$

The terms corresponding to the cosine eigenfunctions become:

$$\sum_{n=1}^{\infty} A_n(\mathbf{r}')J_n(kr)\frac{\cos(n\theta)}{\sqrt{\pi}} \tag{C.5a}$$

$$= \sum_{n=1}^{\infty}\frac{-\pi}{4j\sqrt{\pi}J_n(ka)}\left[J_n(kr')e^{-jn\theta'}H_n^{(2)}(ka) + J_{-n}(kr')e^{jn\theta'}H_{-n}^{(2)}(ka)\right]J_n(ka)\frac{\cos(n\theta)}{\sqrt{\pi}} \tag{C.5b}$$

$$= \sum_{n=1}^{\infty}\frac{-1}{4j}\left[J_n(kr')e^{-jn\theta'}H_n^{(2)}(ka) + J_{-n}(kr')e^{jn\theta'}H_{-n}^{(2)}(ka)\right]\cos(n\theta) \tag{C.5c}$$

$$= \sum_{n=1}^{\infty}\frac{-1}{4j}J_n(kr')e^{-jn\theta'}H_n^{(2)}(ka)\cos(n\theta) + \sum_{n=1}^{\infty}\frac{-1}{4j}J_{-n}(kr')e^{jn\theta'}H_{-n}^{(2)}(ka)\cos(n\theta) \tag{C.5d}$$

$$= \sum_{n=1}^{\infty}\frac{-1}{4j}J_n(kr')e^{-jn\theta'}H_n^{(2)}(ka)\cos(n\theta) + \sum_{n=-\infty}^{-1}\frac{-1}{4j}J_n(kr')e^{-jn\theta'}H_n^{(2)}(ka)\cos(-n\theta) \tag{C.5e}$$

$$= \sum_{n=[-\infty,\infty]\setminus\{0\}}\frac{-1}{4j}J_n(kr')e^{-jn\theta'}H_n^{(2)}(ka)\cos(n\theta), \tag{C.5f}$$

and the terms for the sine eigenfunctions become:

$$\sum_{n=1}^{\infty} B_n(\mathbf{r}')J_n(kr)\frac{\sin(n\theta)}{\sqrt{\pi}} \tag{C.6a}$$

$$= \sum_{n=1}^{\infty}\frac{-\pi}{4\sqrt{\pi}J_n(ka)}\left[J_n(kr')e^{-jn\theta'}H_n^{(2)}(ka) - J_{-n}(kr')e^{jn\theta'}H_{-n}^{(2)}(ka)\right]J_n(ka)\frac{\sin(n\theta)}{\sqrt{\pi}} \tag{C.6b}$$

$$= \sum_{n=1}^{\infty}\frac{-1}{4}\left[J_n(kr')e^{-jn\theta'}H_n^{(2)}(ka) - J_{-n}(kr')e^{jn\theta'}H_{-n}^{(2)}(ka)\right]\sin(n\theta) \tag{C.6c}$$

$$= \sum_{n=1}^{\infty}\frac{-1}{4}J_n(kr')e^{-jn\theta'}H_n^{(2)}(ka)\sin(n\theta) - \sum_{n=1}^{\infty}\frac{-1}{4}J_{-n}(kr')e^{jn\theta'}H_{-n}^{(2)}(ka)\sin(n\theta) \tag{C.6d}$$

$$= \sum_{n=1}^{\infty}\frac{-1}{4}J_n(kr')e^{-jn\theta'}H_n^{(2)}(ka)\sin(n\theta) - \sum_{n=-\infty}^{-1}\frac{-1}{4}J_n(kr')e^{-jn\theta'}H_n^{(2)}(ka)\sin(-n\theta) \tag{C.6e}$$

$$= \sum_{n=[-\infty,\infty]\setminus\{0\}}\frac{-1}{4}J_n(kr')e^{-jn\theta'}H_n^{(2)}(ka)\sin(n\theta). \tag{C.6f}$$

Adding the results of this first term, plus the results of both the eigenfunction expansions results in:

$$p(\mathbf{r},\mathbf{r}') = \frac{-\sqrt{2}}{4j}J_0(kr')H_0^{(2)}(ka) + \sum_{n=[-\infty,\infty]\setminus\{0\}}\frac{-1}{4j}J_n(kr')e^{-jn\theta'}H_n^{(2)}(ka)(\cos(n\theta) + j\sin(n\theta)) \tag{C.7a}$$

$$= \frac{-\sqrt{2}+1}{4j}J_0(kr')H_0^{(2)}(ka) + \frac{-1}{4j}J_0(kr')H_0^{(2)}(ka) + \sum_{n=[-\infty,\infty]\setminus\{0\}}\frac{-1}{4j}J_n(kr')e^{-jn\theta'}H_n^{(2)}(ka)e^{jn\theta} \tag{C.7b}$$

$$= \frac{-\sqrt{2}+1}{4j}J_0(kr')H_0^{(2)}(ka) + \sum_{n=-\infty}^{\infty}\frac{-1}{4j}J_n(kr')e^{-jn\theta'}H_n^{(2)}(ka)e^{jn\theta} \tag{C.7c}$$

$$= \frac{-\sqrt{2}+1}{4j}J_0(kr')H_0^{(2)}(ka) - g_{fs}(\mathbf{r},\mathbf{r}') \neq -g_{fs}(\mathbf{r},\mathbf{r}') \tag{C.7d}$$

This shows that $p \neq -g_{fs}$ when $\mathbf{r} \in \Omega$, suggesting that there will exist an electric field on the PEC surface, which cannot occur due to the property of the PEC which tells that the electric field had to vanish.

Correction

As stated above, the problem arises from the order 0 zero term in the eigenfunction expansion: $\frac{A_0(\mathbf{r}')}{\sqrt{2\pi}} J_0(kr)$. In the denominator of this fraction, the factor $\sqrt{2}$ does not cancel against the factor 2 coming from the A_0 term. If the first term was written as:

$$\frac{A_0(\mathbf{r}')}{2\sqrt{\pi}} J_0(kr), \tag{C.8}$$

these factors of two would cancel against each other, which would result in p being equal the negative of g_{fs} when $\mathbf{r} \in \Omega$. Applying this correction makes sure that the shielded Greens function satisfies the boundary value problem given in Eq. 3.1.

Note: in the appendix of [27], an exception was made to the definition of A_0, this means that this correction was already mentioned by the authors of the original paper.

D

Analysis of standing waves

From testing it appeared that the Modified Greens function as proposed by Gilmore in [26], [27] provides a constant phase response, and thus should that the Greens functions will result in a collection of standing waves. This appendix shows why this phase is constant, and what this phase should be. The modified Greens function, as shown many times before, is given by:

$$g_{sh}^{EJ}(\mathbf{r},\mathbf{r}') = g^{EJ}(\mathbf{r},\mathbf{r}') + p^{EJ}(\mathbf{r},\mathbf{r}'). \tag{D.1}$$

This appendix will first focus on the derivation of the phase of the correction term $p(\mathbf{r},\mathbf{r}')$, which is given by:

$$p^{EJ}(\mathbf{r},\mathbf{r}') = \frac{A_0}{2\sqrt{\pi}} J_0(kr) + \sum_{n=1}^{\infty} J_n(kr)\left(A_n(\mathbf{r}')\frac{\cos(n\theta)}{\sqrt{\pi}} + B_n(\mathbf{r}')\frac{\sin(n\theta)}{\sqrt{\pi}}\right). \tag{D.2}$$

Simplifying the correction term of the shielded electric field Greens function

Substituting the definition of A_n and B_n into Eq. D.2 results in:

$$\begin{aligned} p^{EJ}(\mathbf{r},\mathbf{r}') = &\frac{-\pi}{4j\sqrt{\pi}J_0(ka)}\left[2J_0(kr')H_0^{(2)}(ka)\right]\frac{1}{2\sqrt{\pi}}J_0(kr) + \\ &\sum_{n=1}^{\infty} J_n(kr)\left(\frac{-\pi}{4j\sqrt{\pi}J_n(ka)}\left[J_n(kr')e^{-jn\theta'}H_n^{(2)}(ka) + J_{-n}(kr')e^{jn\theta'}H_{-n}^{(2)}(ka)\right]\frac{\cos(n\theta)}{\sqrt{\pi}} + \right. \\ &\left.\frac{-\pi}{4\sqrt{\pi}J_n(ka)}\left[J_n(kr')e^{-jn\theta'}H_n^{(2)}(ka) - J_{-n}(kr')e^{jn\theta'}H_{-n}^{(2)}(ka)\right]\frac{\sin(n\theta)}{\sqrt{\pi}}\right) \end{aligned} \tag{D.3}$$

Collecting all terms which cancel against one other; these terms contain all π and $\sqrt{\pi}$ terms.

$$\begin{aligned} p^{EJ}(\mathbf{r},\mathbf{r}') = &\frac{-1}{4jJ_0(ka)}J_0(kr')H_0^{(2)}(ka)J_0(kr) + \\ &\sum_{n=1}^{\infty}\frac{-J_n(kr)}{4jJ_n(ka)}\left(\left[J_n(kr')e^{-jn\theta'}H_n^{(2)}(ka) + J_{-n}(kr')e^{jn\theta'}H_{-n}^{(2)}(ka)\right]\cos(n\theta) + \right. \\ &\left. j\left[J_n(kr')e^{-jn\theta'}H_n^{(2)}(ka) - J_{-n}(kr')e^{jn\theta'}H_{-n}^{(2)}(ka)\right]\sin(n\theta)\right) \end{aligned} \tag{D.4}$$

Collect all positive ordered Bessel and Hankel functions, and collect all negatively ordered Bessel and Hankel functions:

$$p^{EJ}(\mathbf{r},\mathbf{r}') = \frac{-1}{4jJ_0(ka)} J_0(kr') H_0^{(2)}(ka) J_0(kr) + \sum_{n=1}^{\infty} \frac{-J_n(kr)}{4jJ_n(ka)} \Big(J_n(kr') e^{-jn\theta'} H_n^{(2)}(ka) \left[\cos(n\theta) + j\sin(n\theta)\right] + J_{-n}(kr') e^{jn\theta'} H_{-n}^{(2)}(ka) \left[\cos(n\theta) - j\sin(n\theta)\right] \Big) \tag{D.5}$$

Using Euler's identity to convert the sine and cosine terms to there exponential representation, to consequently combine it with the other exponential. This step also includes the conversion of the negatively ordered Bessel functions using $J_{-n}(x) = (-1)^n J_n(x)$ [28], and $H_{-n}^{(2)}(x) = e^{-j\pi n} H_n^{(2)}(x)$[28], which becomes $H_{-n}^{(2)}(x) = (-1)^n H_n^{(2)}(x)$ for $n \in \mathbb{Z}$. This will result in:

$$p^{EJ}(\mathbf{r},\mathbf{r}') = \frac{-1}{4jJ_0(ka)} J_0(kr') H_0^{(2)}(ka) J_0(kr) + \sum_{n=1}^{\infty} \frac{-J_n(kr)}{4jJ_n(ka)} \Big(J_n(kr') e^{jn(\theta-\theta')} H_n^{(2)}(ka) + J_n(kr') e^{jn(\theta'-\theta)} H_n^{(2)}(ka) \Big) \tag{D.6}$$

The exponentials in this term can be combined to form the cosine, and finally due to the symmetry in the cosine the one-sided infinte sum can be converted a double-sided infinite sum.

$$p^{EJ}(\mathbf{r},\mathbf{r}') = \frac{-1}{4jJ_0(ka)} J_0(kr') H_0^{(2)}(ka) J_0(kr) + \sum_{n=1}^{\infty} \frac{-J_n(kr)}{2jJ_n(ka)} \Big(J_n(kr') H_n^{(2)}(ka) \cos(n(\theta-\theta')) \Big) \tag{D.7}$$

$$= \sum_{n=-\infty}^{\infty} \frac{-H_n^{(2)}(ka) J_n(kr) J_n(kr') \cos(n(\theta-\theta'))}{4jJ_n(ka)} \tag{D.8}$$

Phase of the shielded greens function is zero

This section will show that the imaginary part of g^{EJ} and p^{EJ} are equal, thus that the complete electric field Greens function is real, thus produces a standing wave. The Bessel functions of the first and second kind are real function (for real arguments). Applying the series expansion of the 0 order Hankel function of the second kind[17] (for $r' \geq r$), and taking the imaginary part of the free-space Greens function results in:

$$\Im\left[g^{EJ}(\mathbf{r},\mathbf{r}')\right] = \Im\left[\frac{1}{4j} H_0^{(2)}(k|\mathbf{r}-\mathbf{r}'|)\right] \tag{D.9a}$$

$$= \Im\left[\frac{1}{4j} \sum_{n=-\infty}^{\infty} J_n(kr') H_m^{(2)}(kr) e^{jn(\theta-\theta')}\right] \tag{D.9b}$$

$$= \Im\left[\frac{1}{4j} \sum_{n=-\infty}^{\infty} J_n(kr')(J_n(kr) - jY_n(kr))(\cos(n(\theta-\theta')) + j\sin(n(\theta-\theta')))\right] \tag{D.9c}$$

$$= \frac{1}{4} \sum_{n=-\infty}^{\infty} J_n(kr') J_n(kr) \cos(n(\theta-\theta')). \tag{D.9d}$$

The above mentioned separation of variable is only true when $r' \geq r$, but using the separation of variable for when $r' \leq r$ results in the same, using the same method. Taking the imaginary part of the correction term p results in:

$$\Im\left[p(\mathbf{r},\mathbf{r}')\right] = \Im\left[\sum_{n=-\infty}^{\infty} \frac{-H_n^{(2)}(ka) J_n(kr) J_n(kr') \cos(n(\theta-\theta'))}{4jJ_n(ka)}\right] \tag{D.10a}$$

$$= \Im\left[\sum_{n=-\infty}^{\infty} \frac{-(J_n(ka) - jY_n(ka)) J_n(kr) J_n(kr') \cos(n(\theta-\theta'))}{4jJ_n(ka)}\right] \tag{D.10b}$$

$$= -\frac{1}{4} \sum_{n=-\infty}^{\infty} J_n(kr) J_n(kr') \cos(n(\theta-\theta')), \tag{D.10c}$$

showing that the imaginary part of g^{EJ} equals the negative of the imaginary part of p^{EJ}. Therefore adding both the real and imaginary part g to the real and imaginary part of p results in just adding their real parts:

$$g_{sh}^{EJ}(\mathbf{r},\mathbf{r}') = \mathrm{Re}\left\{g^{EJ}(\mathbf{r},\mathbf{r}')\right\} + \mathrm{Re}\left\{p^{EJ}(\mathbf{r},\mathbf{r}')\right\} \tag{D.11}$$

$$= \frac{-1}{4} Y_0(k|\mathbf{r}-\mathbf{r}'|) + \sum_{n=-\infty}^{\infty} \frac{Y_n(ka)}{4J_n(ka)} J_n(kr) J_n(kr') \cos(n(\theta-\theta')). \tag{D.12}$$

E

Derivation for shielded magnetic field Greens function

The derivation of the Greens operator which describes the Magnetic fiels as a result of an electric current/contrast source, requires the curl of the (electric field) Greens function. Due to the distributive properties of the cross-product, the calculation of the shielded Greens function can be written as:

$$\nabla \times G(\mathbf{r},\mathbf{r}') = \nabla \times g_{fs}(\mathbf{r},\mathbf{r}') + \nabla \times p(\mathbf{r},\mathbf{r}'), \tag{E.1}$$

where the curl of the free-space Greens function is known, as it is also used in the $g_{fs}^{HJ}(\mathbf{r},\mathbf{r}')$. The curl of this free-space Greens function is then given by:

$$\begin{aligned}\nabla \times g_{fs}(\mathbf{r},\mathbf{r}') = &-\frac{y-y'}{||\mathbf{r}-\mathbf{r}'||}\frac{k}{4j}H_1^{(2)}\left(k\left|\left|\mathbf{r}-\mathbf{r}'\right|\right|\right)\hat{x}+\\ &\frac{x-x'}{||\mathbf{r}-\mathbf{r}'||}\frac{k}{4j}H_1^{(2)}\left(k\left|\left|\mathbf{r}-\mathbf{r}'\right|\right|\right)\hat{y}.\end{aligned} \tag{E.2}$$

Solving the curl of the correction term $p(\mathbf{r},\mathbf{r}')$ is a little more involved. Since the correction term $p(\mathbf{r},\mathbf{r}')$ is mostly defined in cylindrical coordinates, taking the curl in cylindrical coordinates is more straightforward. Taking this curl in cylindrical coordinates is done by:

$$\nabla \times p(\mathbf{r},\mathbf{r}') = \left(\frac{1}{r}\frac{\partial p_z}{\partial \theta} - \frac{\partial p_\theta}{\partial z}\right)\hat{r} + \left(\frac{\partial p_r}{\partial z} - \frac{\partial p_z}{\partial r}\right)\hat{\theta} + \frac{1}{r}\left(\frac{\partial (r p_\theta)}{\partial r} - \frac{\partial p_r}{\partial \theta}\right)\hat{z} \tag{E.3}$$

Under the assumption that only a $\hat{z}$ component is present in this $p(\mathbf{r},\mathbf{r}')$, this curl can be solved for the $\hat{r}$ and $\hat{\theta}$ components separately. The $\hat{r}$ component results in:

$$\left(\frac{1}{r}\frac{\partial p_z}{\partial \theta} - \frac{\partial p_\theta}{\partial z}\right) = \frac{1}{r}\frac{\partial p_z}{\partial \theta} \tag{E.4}$$

$$= \frac{1}{r}\frac{\partial}{\partial \theta}\sum_{n=-\infty}^{\infty}\frac{-H_n^{(2)}(ka)}{4jJ_n(ka)}J_n(kr)J_n(kr')\cos(n(\theta-\theta')) \tag{E.5}$$

$$= \frac{1}{r}\sum_{n=-\infty}^{\infty}\frac{H_n^{(2)}(ka)}{4jJ_n(ka)}J_n(kr)J_n(kr')n\sin(n(\theta-\theta')), \tag{E.6}$$

while the $\hat{\theta}$ component results in:

$$\left(\frac{\partial p_r}{\partial z} - \frac{\partial p_z}{\partial r}\right) = -\frac{\partial p_z}{\partial r} \tag{E.7}$$

$$= \frac{\partial}{\partial r}\sum_{n=-\infty}^{\infty}\frac{H_n^{(2)}(ka)}{4jJ_n(ka)}J_n(kr)J_n(kr')\cos(n(\theta-\theta')) \tag{E.8}$$

$$= \sum_{n=-\infty}^{\infty}\frac{H_n^{(2)}(ka)}{8jJ_n(ka)}J_n(kr')\cos(n(\theta-\theta'))k\left(J_{n-1}(kr)-J_{n+1}(kr)\right) \tag{E.9}$$

These can be easily converted to the Cartesian coordinate system by taking $\hat{r} = \cos(\theta)\hat{x} + \sin(\theta)\hat{y}$, and $\hat{\theta} = -\sin(\theta)\hat{x} + \cos(\theta)\hat{y}$.

F

Extra results

This appendix provides extra results of simulations which are not directly present in the main body of the thesis. The results presented here are divided in three sections: the first is the results of the simulation without quantization on the synthetic E-polarized measurements using a realistic noise level having an SNR of 35dB; the second shows the results when a fixed scalar is applied to the greens operators to improve the reconstruction results; and the final section shows the reconstruction of the tissue parameters for the different noise levels described in Sec. 5.3.

F.1. Reconstruction noisy 2D without quantization

This section will describe the simulation results for a simulation where the noise is of the same level as described in Sec. 5.4, using synthetic E-polarized measurements having a SNR of 35dB. This section will primarily be used to show the poor performance of the shielded CSI-EPT reconstruction algorithm when the quantization is not applied. All results use the same metris as described in Sec. 5.1.

Cost function

Figure F.1 shows the progression of the cost functions of the shielded CSI-EPT for 2000 iterations. The distribution and the progression of M1 are approximately equal, this will be dicussed as one.

The progression shows a very fast decay towards the minimal value of $4 \cdot 10^{-4}$. Even considering this noisy measurement, the shielded CSI-EPT algorithm converges to a minimal value for the cost function. The effect of explosion caused by the ill-posed nature of the problem is also not observed here. The smoothness of the fields inherently means that rapid changes introduced by high frequency noise cannot be modeled accurately, leading to a mismatch between the modeled and measured fields, increasing the data residual.

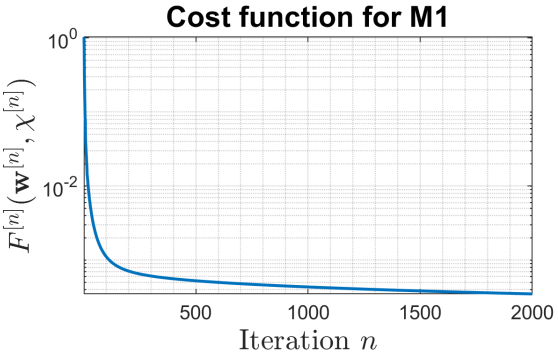

(a) Progression of the cost function for subject M1

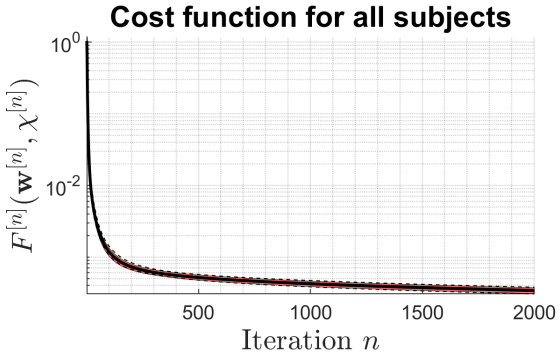

(b) Distribution of the cost function for all subjects. The black line shows the mean of all cost functions, the red regions show the area span by once or twice the standard deviation, while the dashed lines represent the maximum and the minimum of all cost functions

Figure F.1: Progression of the cost function as a function of the iteration number for the noisy (SNR=35dB) 2D, truly E-polarized simulation setup. These results are obtained using the shielded CSI-EPT algorithm without the quantization methods

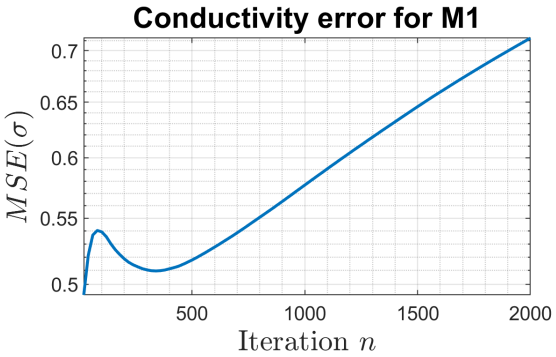

(a) Progression of the reconstruction error for the conductivity of subject M1

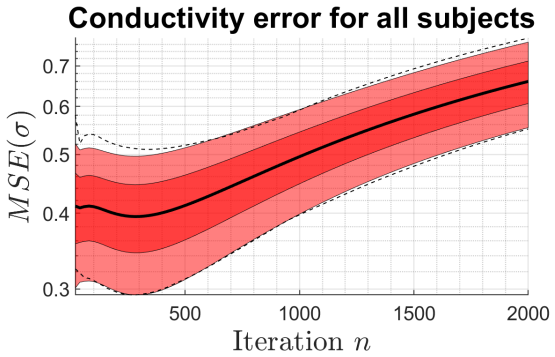

(b) Distribution of the reconstruction error for the conductivity for all subjects. The black line shows the mean, the red regions show the area span by once or twice the standard deviation, while the dashed lines represent the maximum and the minimum.

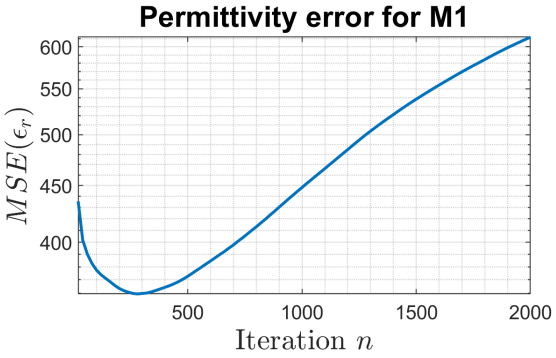

(c) Progression of the reconstruction error for the relative permittivity of subject M1

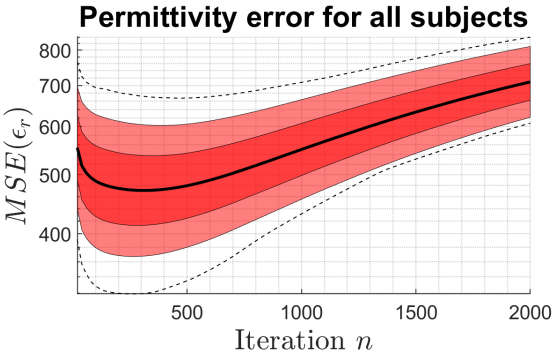

(d) Distribution of the reconstruction error for the relative permittivity for all subjects. The black line shows the mean, the red regions show the area span by once or twice the standard deviation, while the dashed lines represent the maximum and the minimum.

Figure F.2: Reconstruction errors for the electrical properties for the noisy(SNR=35dB) 2D, truly E-polarized simulation setup. These results are obtained using the shielded CSI-EPT algorithm without the quantization methods

Reconstruction errors

Figures F.2 display the progression of the reconstruction errors for the tissue parameters; Figs. F.2a and F.2b show the MSE for the conductivity for subject M1 and the distribution for all subjects, respectively; while Figs. F.2a and F.2b show these for the relative permittivity.

Whereas the cost function converged to a minimum, both the reconstruction error of the conductivity and relative permittivity increase after reaching a minimum after a few iterations.

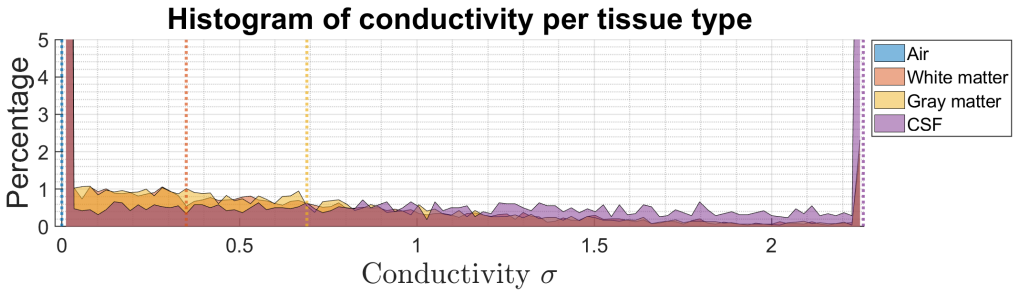

(a) Histograms for the reconstructed conductivity of subject M1

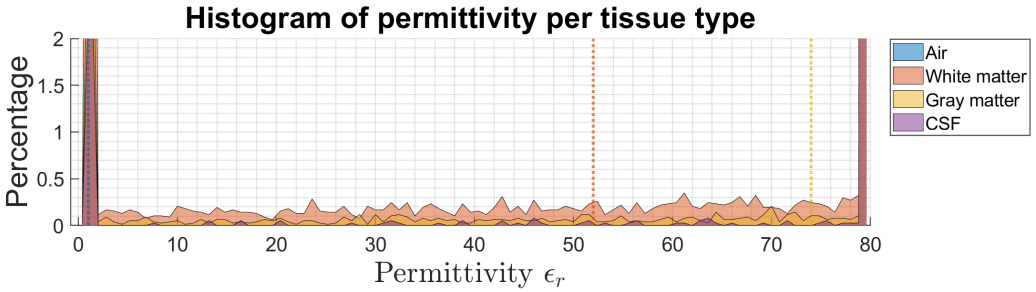

(b) Histograms for the reconstructed relative permittivity of subject M1

Figure F.3: Histograms of the reconstructed electrical properties per tissue after 2000 iterations for the noisy(SNR=35dB) 2D, truly Epolarized simulation setup. These results are obtained using the shielded CSI-EPT algorithm without the quantization methods

Histogram

Figure 5.10 shows the distributions of the tissue parameters for the different tissues after 2000 iteration of quantized shielded CSI-EPT. As shown by the diverging MSE for both the conductivity and the relative permittivity, the performance of reconstruction is poor. For both tissue parameters, the modes are overlapping, not showing any resemblance to the expected multi-modality of these distributions. This poor reconstruction performace is also shown in the actual reconstructions of the conductivity and relative permittivity, as shown in Figs. F.4a and F.4b, respectively.

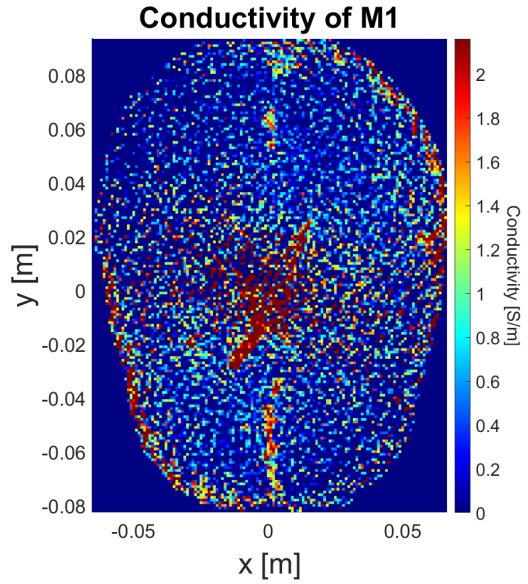

(a) Reconstructed conductivity of subject M1

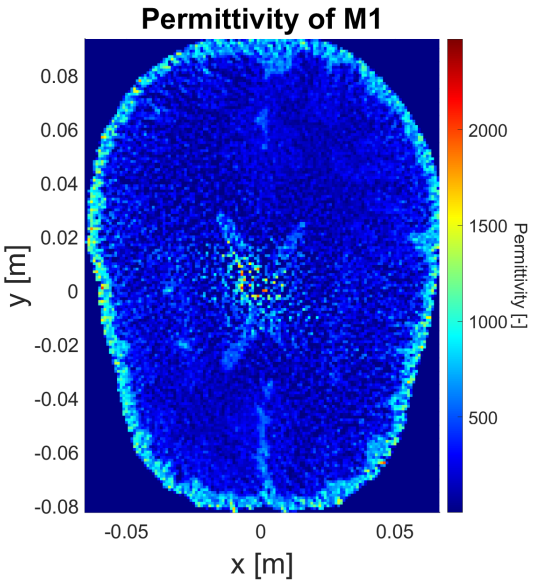

(b) Reconstructed relative permittivity of subject M1

Figure F.4: Reconstructed electrical properties after 2000 iterations for the noisy(SNR=35dB) 2D, truly E-polarized simulation setup. These results are obtained using the shielded CSI-EPT algorithm without the quantization methods

F.2. Reconstruction 3D dataset

During testing, it was observed that the magnitude of the contrast was under estimated by approximately a factor 2. Also the contrast source appeared to be estimated with a 90 degrees phase shift, resulting in a phase shift in the reconstructed fields. This section will describe the results using measurements from the ADEPT dataset, where in this specific simulations the Greens operators are multiplied with $2j$. The incident fields are then also generated using these modified Greens operators.

Cost function

Figure F.5 shows the progression of the cost function as a function of iteration number for 2000 iterations; Fig. F.5a shows the progression for subject M1, while Fig. 5.12b shows the distribution for all subjects.

Comparing this cost function to the progression of the original 3D reconstructions, as shown in Fig. 5.12 shows two things. The first is that the progression as shown in Fig. F.5a is not a smooth function. Where the step size for each iteration seemed to be getting smaller for the original 3D simulation, in the modified simulation this is not necessarily true. The second, maybe more important, notion is that the final value of the cost function is significantly lower when using the modified greens operator, reaching a value of approximately $2 \cdot 10^{-3}$ in comparison to the final value of $8 \cdot 10^{-3}$ for the original three dimensional simulation. This shows that modified version is better at modeling the scattered magnetic field than the original.

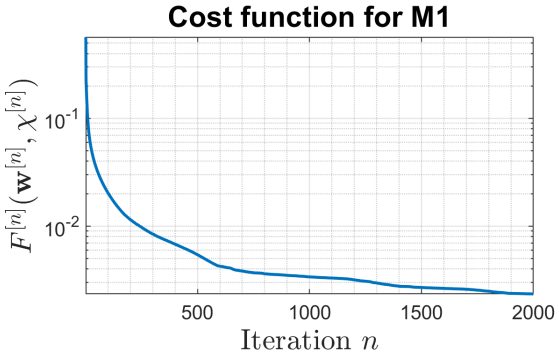

(a) Progression of the cost function for subject M1

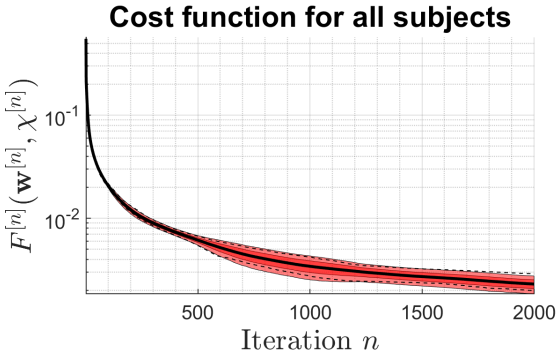

(b) Distribution of the cost function for all subjects. The black line shows the mean of all cost functions, the red regions show the area span by once or twice the standard deviation, while the dashed lines represent the maximum and the minimum of all cost functions

Figure F.5: Progression of the cost function as a function of the iteration number for the realistic 3D simulation setup. In this simulation the greens operators are multiplied with $2j$

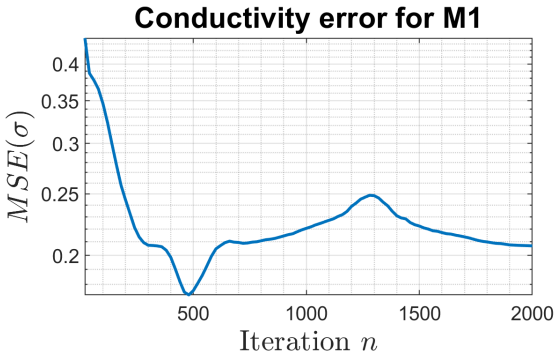

(a) Progression of the reconstruction error for the conductivity of subject M1

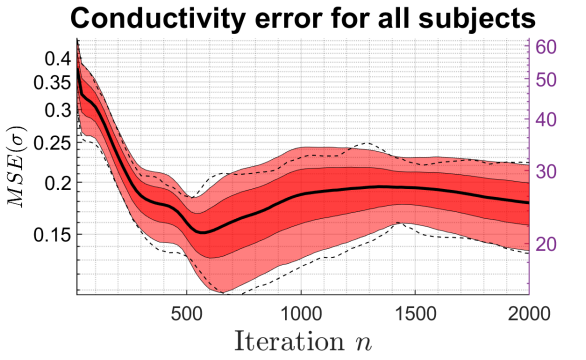

(b) Distribution of the reconstruction error for the conductivity for all subjects. The black line shows the mean, the red regions show the area span by once or twice the standard deviation, while the dashed lines represent the maximum and the minimum

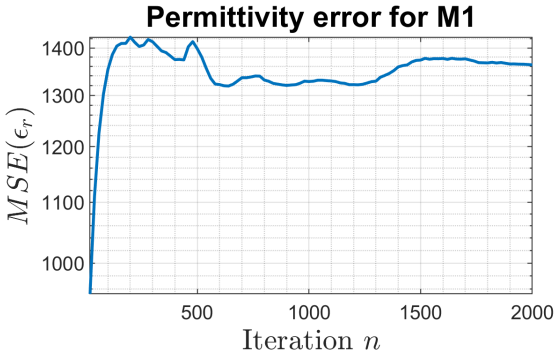

(c) Progression of the reconstruction error for the relative permittivity of subject M1

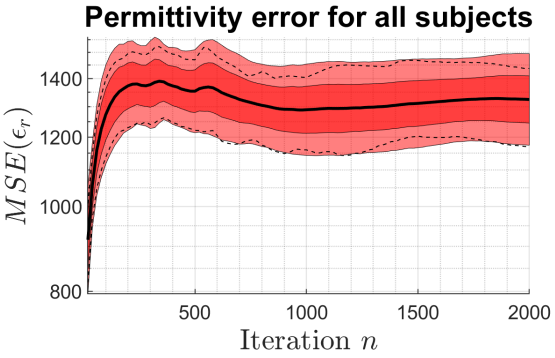

(d) Distribution of the reconstruction error for the relative permittivity for all subjects. The black line shows the mean, the red regions show the area span by once or twice the standard deviation, while the dashed lines represent the maximum and the minimum

Figure F.6: Reconstruction errors for the electrical properties for the realistic 3D simulation setup. In this simulation the Greens operators are multiplied with $2j$

Reconstruction errors

Figure F.6 shows the reconstruction errors of the conductivity and relative permittivity; Figs. F.6a and F.6c shows these for subject M1, and Figs. F.6b and F.6d show the distributions for all subjects.

For the permittivity the performance has not significantly increased, but the reconstruction performance of the conductivity has improved. For the original simulations the MSE of the conductivity after 2000 iterations only reached 0.56, whereas this 'modified' implementation reaches an MSE of 0.21. The progression of the MSE for the original case was converging towards this 0.56 value, while the progression of this modified implementation is shows local minima. This could be expected due to the model mismatch between the two- and three-dimensional model.

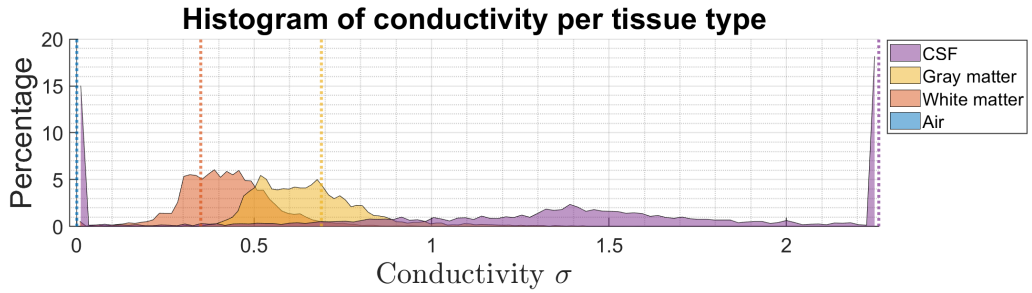

(a) Histograms for the reconstructed conductivity of subject M1

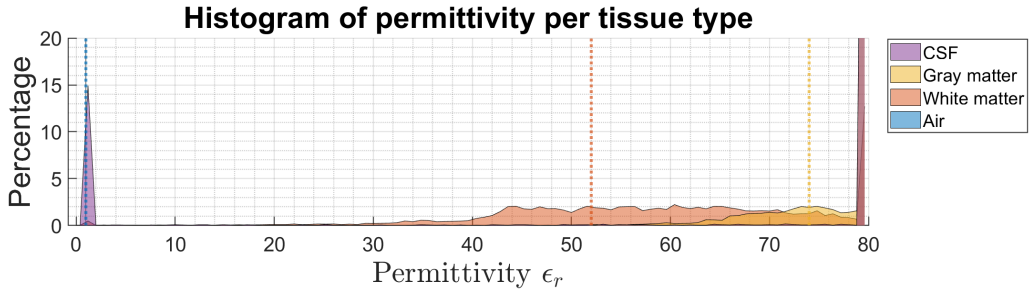

(b) Histograms for the reconstructed permittivity of subject M1

Figure F.7: Histograms of the reconstructed electrical properties per tissue after 2000 iterations for the three-dimensional dataset from ADEPT. These results are obtained using the shielded CSI-EPT algorithm with the modified Greens operator (which are multiplied by $2j$)

Histograms

Figure F.7 shows the histograms for the different tissues after 2000 iterations of the shielded CSI-EPT algorithm with the modified Greens operators. For the conductivity, as shown in Fig. F.7a, the modes are reconstructed closer to their ground truth values, while still having a large variance. This large variance causes the gray and white matter modes to overlap. While overlapping, one can make a good distinction between the two. The conductivity of the CSF is still severely underestimated. Such a reconstruction could now allow for the quantization method to be applicable, which was previously not applicable due to the complete overlap of several modes.

For the relative permittivity values, however, the variance of the modes is much too large. This means the tissues cannot be characterized on their permittivity values alone, as the wide modes are overlapping significantly.

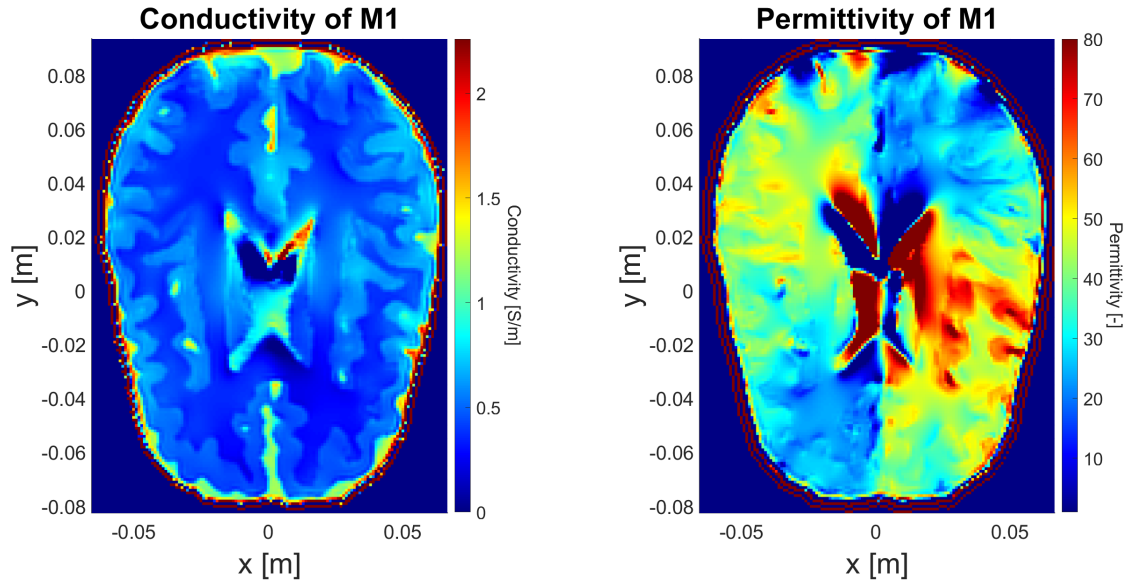

(a) Reconstructed conductivity for subject M1

(b) Reconstructed conductivity for subject M1

Figure F.8: Reconstructed electrical properties after 2000 iterations of the shielded CSI-EPT algorithm performed on the three-dimensional dataset. The Greens operators in this simulation are multiplied with $2j$

Reconstruction image

Finally, Fig. F.8 shows the reconstructed tissue parameters of subject M1 after 2000 iterations of the shielded CSI-EPT algorithm with the implementation of the 'modified' Greens operators. This primarily shows that the conductivity values are reconstructed well qualitatively, while the permittivity values are not reconstructed well (both qualitatively as quantitatively). In the reconstruction of the conductivity, the different tissues can be easily differentiated from oneother. The low-frequency artifact near the center is still present, but significantly reduced in comparison to the original reconstruction of Fig. 5.15a. This shows that the assumption of E-polarization is pretty accurate, allowing for good reconstructions (qualitatively) on three-dimensional data.

F.3. Reconstructions for different noise levels

Section 5.3 displayed the analysis of the shielded CSI-EPT methods without and with the quantization methods for different noise levels. That section showed the significance for the quantization step to higher noise levels (thus lower SNRs), and the due to the coupling of the tissue parameters in the clustering on the magnitude and phase of the contrast function, instead of the clustering on the conductivity and relative permittivity values, the performance of the permittivity reconstructed increased significantly for all noise levels (even very low noise levels with high SNRs). The following figures show the reconstructions of these tissue parameters for these different noise levels, with and without the inclusion of the quantization step. Figures F.9 and F.10 show the conductivity and relative permittivity reconstruction for different noise levels without quantization respectively. Figures F.9 and F.10 shows these results when the quantization is applied.

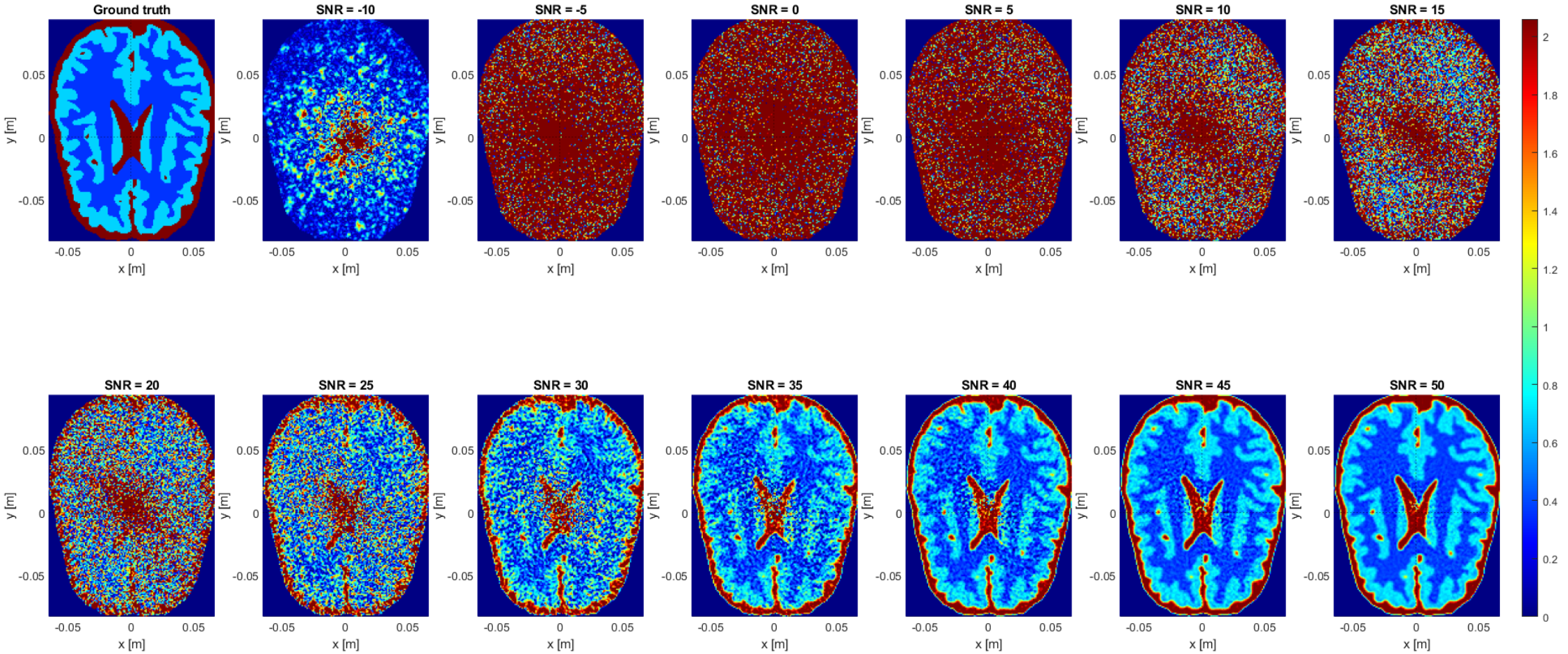

Figure F.9: Conductivity reconstruction for different noise levels after 2000 iteration of shielded CSI-EPT without quantization

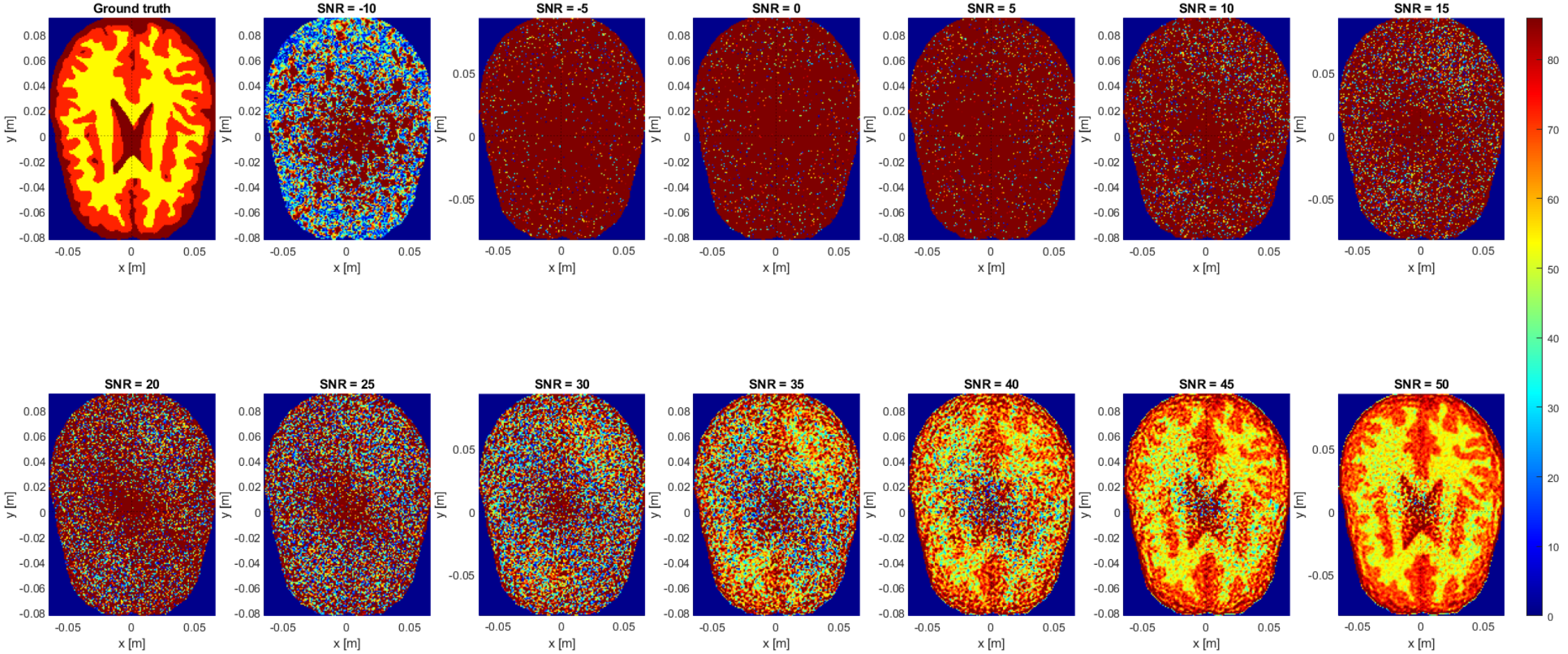

Figure F.10: Permittivity reconstruction for different noise levels after 2000 iteration of shielded CSI-EPT without quantization

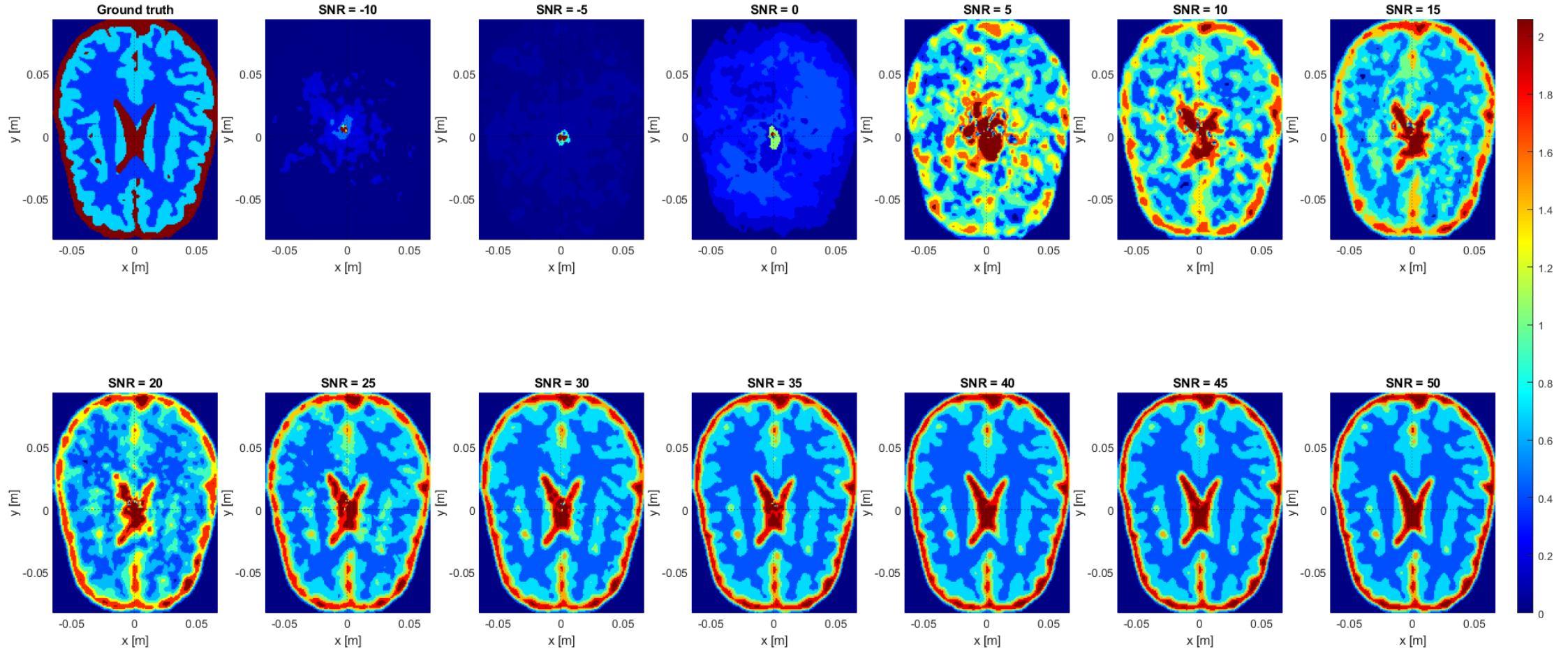

Figure F.11: Conductivity reconstruction for different noise levels after 2000 iteration of shielded CSI-EPT with quantization

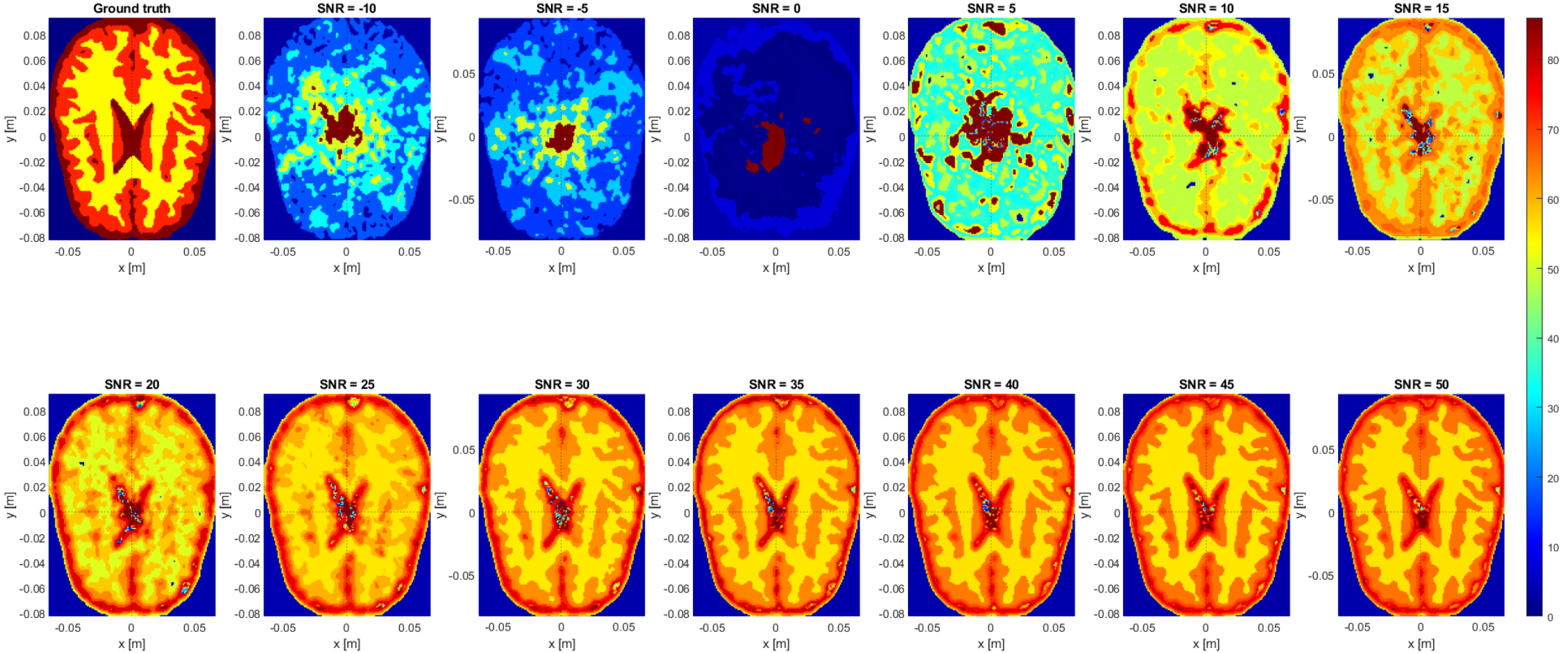

Figure F.12: Relative permittivity reconstruction for different noise levels after 2000 iteration of shielded CSI-EPT with quantization

G

Comparison CSI-EPT methods

This chapter will show the comparison between the CSI-EPT method without shielding as described in Chapter 2 and the method with shielding as described in 3. Literature describes that the reconstruction accuracy is strongly dependent on the estimation of the incident field. Thus, the reconstruction accuracy of for different incident fields will also be shown.

All methods assume the presence of only E-polarized waves in a shielded birdcage coil, where the rungs of the birdcage coil all represented as line currents. The analytical description of Chapter 3 is the correct description of this, as this describes this particular situation analytically. For this comparison the measured fields will be synthesized by solving the forward problem using the operators given by this analytical description, after which the reconstruction will be performed on these. The reconstruction will be performed using two sets of Greens operators, and three incident fields, resulting in six different methods. For the Greens operators the free-space operators and the shielded operators will be used. For the incident fields three situation will be created, the first is the rungs of the antennas radiating in free-space, the second is creating the incident fields using the mirror-source approximation as described in Chapter 2, and the final is using the analytical description of the shielding.

This comparison of the different implementation will be performed without noise. All results will be shown as a the average of the first 60 models of the ADEPT dataset, for which 1000 iterations of the (shielded) CSI-EPT will be performed.

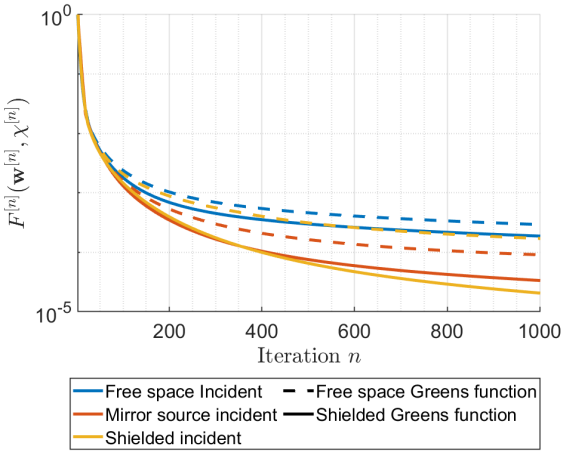

Figure G.1: Progression of the cost function for different noiseless simulation setups, such that the performance can be compared for the free-space and shielded Greens operators, and the free-space, mirror-shield, and shielded incident fields.

Cost function

Figure G.1 shows the progression of the different simulation setups described in the introduction of the Appendix. Most notable in this figure is that all of the cost function are converging to their own respective minimum, where the simulations with the shielded Greens operators reach a lower value of the cost function than the simulations with the free-space operators for the same incident fields. For the shielded Greens operators, we can observe that the properly shielded incident field performs better than the mirror-sourced incident field, which on its own performs better than the free-space incident field. For the free-space Greens operators, however, the mirror-source incident field performs better than the properly shielded incident field.

The free-space incident field has in general a much higher amplitude than the (approximately shielded) mirror-source incident field, and the properly shielded incident fields. The shielding will in first instance cause for a destructive interference, due to the small distances the waves have to travel with respect to the wavelengths.

The effect of explosion caused by the ill-posed nature, as has been observed in [31], is still not present in these simulations. The major difference between the simulations in which this explosion is observed, and these simulations is the sampling size in x and y, which in this simulation is 1 mm, while this is 2.5 mm, for the simulation in this literature. This smaller sampling in space allows for a more accurate Riemann sum representation of the required integrals.

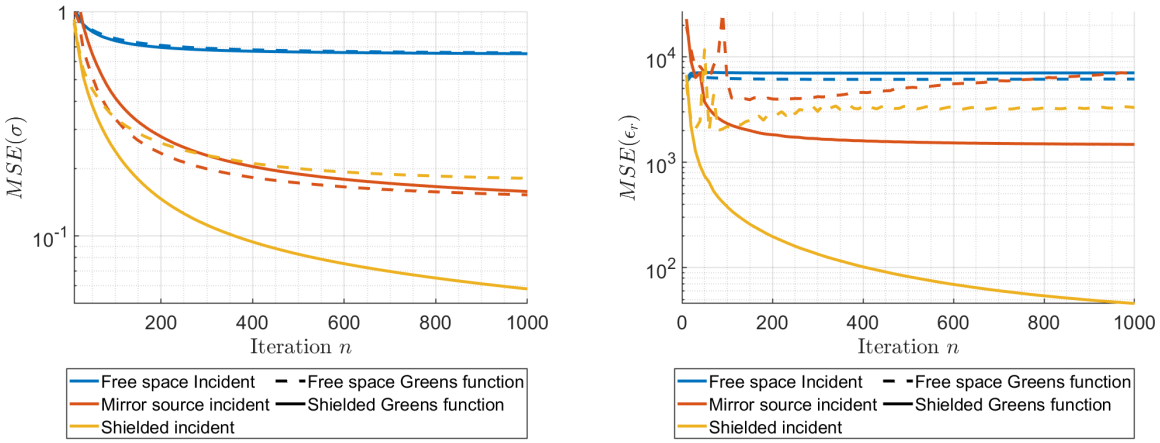

(a) MSE of the conductivity plotted for each iteration of the (shielded) CSI-EPT

(b) MSE of the relative permittivity plotted for each iteration of the (shielded) CSI-EPT

Figure G.2: Reconstruction errors for the different methods

Reconstruction error

Figure G.2a shows the reconstruction errors as measured by the MSE of the conductivity for the different methods, and Fig. G.2b shows this for the relative permittivity.

The MSE of the conductivity converges to a minimum for all methods. As expected, the fully shielded (where both the shielded incident field as the shielded Greens operator are used) performs significantly better than all other methods, since the same operators are used for the measurements as for the inversion algorithm. Due to the wrong scaling of the free-space incident fields, both methods using these incident fields perform really poorly, since this too large (in magnitude field) causes for an underestimation of the magnitude of the contrast function from the contrast source, leading to an underestimation of booth conductivity and permittivity.

What is most interesting from this analysis is that for the methods using the mirror-source incident fields the method using the free-space operator performs slightly better than the method using the Greens operators, and that both these methods perform better than the method using the free-space Greens operators with the fully shielded incident field.

The main disadvantage of the inaccurate greens operators, and inaccurate incident field is shown by the progression of the MSE of the reative permittivity of Fig. G.2b. This shows that only two of the six methods converge to a minimum, while the other methods have their minimum not at the final iteration. This shows the importance of an accurate estimation of the incident field.

Reconstruction images

Figure G.3 shows the tissue parameters for the different method, along with the ground truths in the most left images. The colorbars for the conductivities of images is located on the top of the image, whereas the colorbar for the permittivities is found below the images.

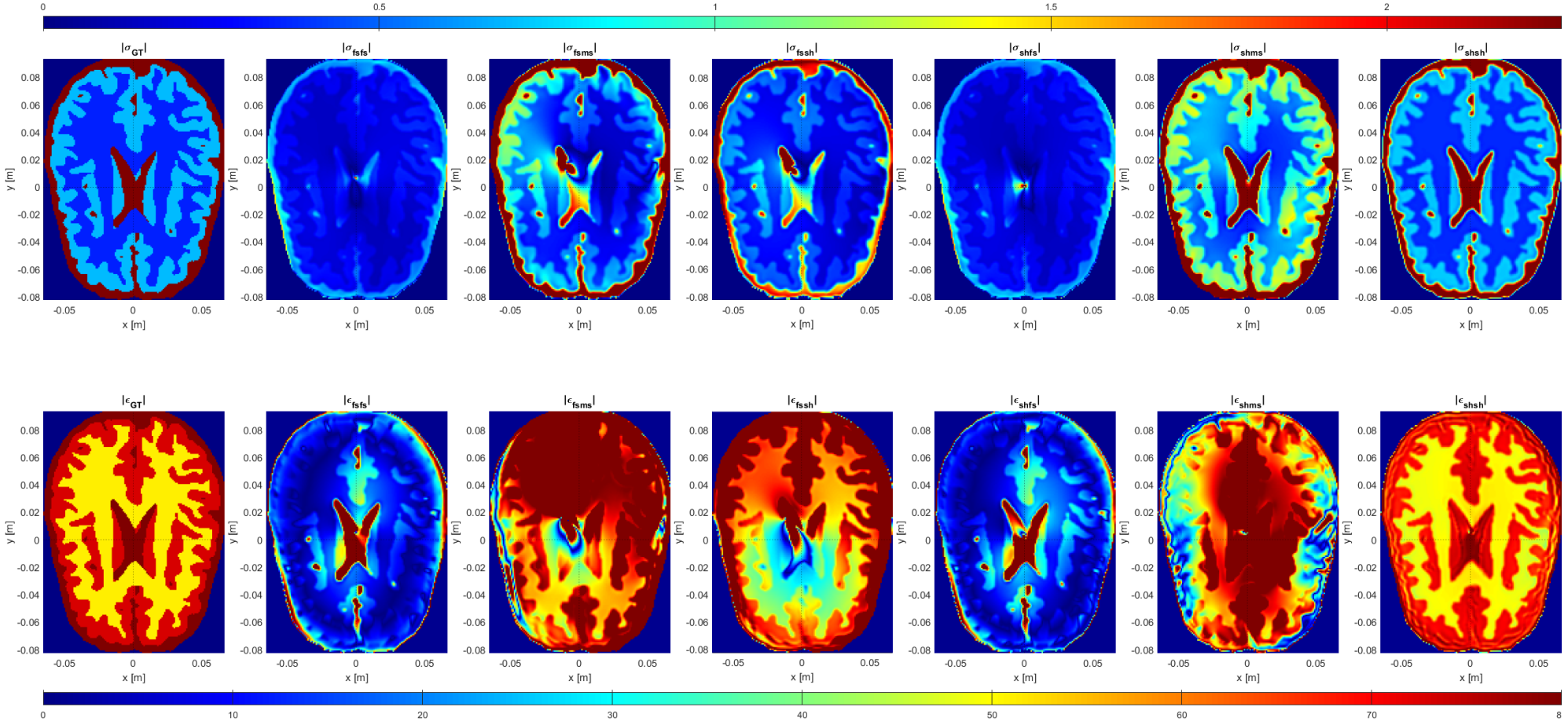

Figure G.3: Reconstructed tissue parameters for different methods. n the subscript of the titles the methods are described: the first two letters describe the greens operators used (fs: free-space, sh: shielded), while the second two describe the used incident field (fs: free-space, ms: mirror-source, sh: shielded). The subscript GT for the most left parameters denotes the ground truth of the parameters